FINAL REPORT

**TR-626: Optimization of Snow Drifting Mitigation and
Control Methods for Iowa Conditions**

**Final Report
February 2015**

Submitted by

George Constantinescu, Marian Muste and K. Basnet
Department of Civil & Environmental Engineering
and
IIHR-Hydroscience and Engineering Hydraulics Laboratory
The University of Iowa
Iowa City, IA

Authors:
Univ. Iowa: G. Constantinescu, M. Muste, K. Basnet

Disclaimer Notice

The contents of this report reflect the views of the authors, who are responsible for the facts and the accuracy of the information presented herein. The opinions, findings, and conclusions expressed in this publication are those of the authors and not necessarily of the sponsors. The sponsors assume no liability for the contents or use of the information contained in this document. This report does not constitute a standard, specification, or regulation.

Statement of Non-Discrimination

Acknowledgements

1. Report No. TR-626	2. Government Accession No. Optional	3. Recipient Catalog No. Optional
4. Title and Subtitle Optimization of snow drifting mitigation and control methods for Iowa conditions		5. Report Date February 9, 2015
		6. Performing Organization Code N/A
7. Author(s) Constantinescu G., Muste M. and Basnet K.		8. Performing Organization Report No.
9. Performing Organization Name and Address Dept. Civil and Environmental Engineering, The University of Iowa, Iowa City, IA, 52242 and Dept. Civil, Construction and Environmental Engineering and The Bridge Engineering Center at the Institute for Transportation, Iowa State University, Ames, Iowa.		10. Work Unit No. (TRAIS) Not Required
		11. Contract or Grant No. TR-626 1 80224 00
12. Sponsoring Organization Name and Address Iowa Department of Transportation 800 Lincoln Way Ames, Iowa 50010		13. Type of Report and Period Covered Final Report
		14. Sponsoring Agency Code TR-626
15. Supplementary Notes None		

16. Abstract

Blowing and drifting of snow is a major concern for transportation efficiency and road safety in regions where their development is common. One common way to mitigate snow drift on roadways is to install plastic snow fences. Correct design of snow fences is critical for road safety and maintaining the roads open during winter in the US Midwest and other states affected by large snow events during the winter season and to maintain costs related to accumulation of snow on the roads and repair of roads to minimum levels. Of critical importance for road safety is the protection against snow drifting in regions with narrow rights of way, where standard fences cannot be deployed at the recommended distance from the road. Designing snow fences requires sound engineering judgment and a thorough evaluation of the potential for snow blowing and drifting at the construction site. The evaluation includes site-specific design parameters typically obtained with semi-empirical relations characterizing the local transport conditions. Among the critical parameters involved in fence design and assessment of their post-construction efficiency is the quantification of the snow accumulation at fence sites.

The present study proposes a joint experimental and numerical approach to monitor snow deposits around snow fences, quantitatively estimate snow deposits in the field, asses the efficiency and improve the design of snow fences. Snow deposit profiles were mapped using GPS based real-time kinematic surveys (RTK) conducted at the monitored field site during and after snow storms. The monitored site allowed testing different snow fence designs under close to identical conditions over four winter seasons. The study also discusses the detailed monitoring system and analysis of weather forecast and meteorological conditions at the monitored sites. A main goal of the present study was to assess the performance of lightweight plastic snow fences with a lower porosity than the typical 50% porosity used in standard designs of such fences. The field data collected during the first winter was used to identify the best design for snow fences with a porosity of 50%. Flow fields obtained from numerical simulations showed that the fence design that worked the best during the first winter induced the formation of an elongated area of small velocity magnitude close to the ground. This information was used to identify other candidates for optimum design of fences with a lower porosity. Two of the designs with a fence porosity of 30% that were found to perform well based on results of numerical simulations were tested in the field during the second winter along with the best performing design for fences with a porosity of 50%. Field data showed that the length of the snow deposit away from the fence was reduced by about 30% for the two proposed lower-porosity (30%) fence designs compared to the best design identified for fences with a porosity of 50%. Moreover, one of the lower-porosity designs tested in the field showed no significant snow deposition within the bottom gap region beneath the fence. Thus, a major outcome of this study is to recommend using plastic snow fences with a porosity of 30%. It is expected that this lower-porosity design will continue to work well for even more severe snow events or for successive snow events occurring during the same winter. The approach advocated in the present study allowed making general recommendations for optimizing the design of lower-porosity plastic snow fences. This approach can be extended to improve the design of other types of snow fences. Some preliminary work for living snow fences is also discussed.

Another major contribution of this study is to propose, develop protocols and test a novel technique based on close range photogrammetry (CRP) to quantify the snow deposits trapped snow fences. As image data can be acquired continuously, the time evolution of the volume of snow retained by a snow fence during a storm or during a whole winter season can, in principle, be obtained. Moreover, CRP is a non-intrusive method that eliminates the need to perform man-made measurements during the storms, which are difficult and sometimes dangerous to perform. Presently, there is lots of empiricism in the design of snow fences due to lack of data on fence storage capacity on how snow deposits change with the fence design and snow storm characteristics and in the estimation of the main parameters used by the state DOTs to design snow fences at a given site. The availability of such information from CRP measurements should provide critical data for the evaluation of the performance of a certain snow fence design that is tested by the IDOT. As part of the present study, the novel CRP method is tested at several sites.

The present study also discusses some attempts and preliminary work to determine the snow relocation coefficient which is one of the main variables that has to be estimated by IDOT engineers when using the standard snow fence design software (Snow Drift Profiler, Tabler, 2006). Our analysis showed that standard empirical formulas did not produce reasonable values when applied at the Iowa test sites monitored as part of the present study and that simple methods to estimate this variable are not reliable. The present study makes recommendations for the development of a new methodology based on Large Scale Particle Image Velocimetry that can directly measure the snow drift fluxes and the amount of snow relocated by the fence.

17. **Key Words**		18. **Distribution Statement**	
Snow fence, design optimization, Snow deposits, monitoring performance of snow fences, computational fluid dynamics, 3D photogrammetry		No restrictions. This document is available to the public through the National Technical Information Service, Springfield, Virginia 22161	
19. **Security Classification (of this report)** Unclassified	20. **Security Classification (of this page)** Unclassified	21. **No. of pages** 122	22. **Price** N/A

Form DOT F 1700.7 (8-72)

This page left intentionally blank

TABLE OF CONTENTS

EXECUTIVE SUMMARY

Blowing and drifting of snow is a major concern for transportation efficiency and road safety in regions where their development is common. One common way to mitigate snow drift on roadways is to install plastic snow fences. Correct design of snow fences is critical for road safety and maintaining the roads open during winter in the US Midwest and other states affected by large snow events during the winter season and to maintain costs related to accumulation of snow on the roads and repair of roads to minimum levels. Of critical importance for road safety is the protection against snow drifting in regions with narrow rights of way, where standard fences cannot be deployed at the recommended distance from the road. Designing snow fences requires sound engineering judgment and a thorough evaluation of the potential for snow blowing and drifting at the construction site. The evaluation includes site-specific design parameters typically obtained with semi-empirical relations characterizing the local transport conditions. Among the critical parameters involved in fence design and assessment of their post-construction efficiency is the quantification of the snow accumulation at fence sites.

The present study proposes a joint experimental and numerical approach to monitor snow deposits around snow fences, quantitatively estimate snow deposits in the field, asses the efficiency and improve the design of snow fences. Snow deposit profiles were mapped using GPS based real-time kinematic surveys (RTK) conducted at the monitored field site during and after snow storms. The monitored site allowed testing different snow fence designs under close to identical conditions over four winter seasons. The study also discusses the detailed monitoring system and analysis of weather forecast and meteorological conditions at the monitored sites. A main goal of the present study was to assess the performance of lightweight plastic snow fences with a lower porosity than the typical 50% porosity used in standard designs of such fences. The field data collected during the first winter was used to identify the best design for snow fences with a porosity of 50%. Flow fields obtained from numerical simulations showed that the fence design that worked the best during the first winter induced the formation of an elongated area of small velocity magnitude close to the ground. This information was used to identify other candidates for optimum design of fences with a lower porosity. Two of the designs with a fence porosity of 30% that were found to perform well based on results of numerical simulations were tested in the field during the second winter along with the best performing design for fences with a porosity of 50%. Field data showed that the length of the snow deposit away from the fence was reduced by about 30% for the two proposed lower-porosity (30%) fence designs compared to the best design identified for fences with a porosity of 50%. Moreover, one of the lower-porosity designs tested in the field showed no significant snow deposition within the bottom gap region beneath the fence. Thus, a major outcome of this study is to recommend using plastic snow fences with a porosity of 30%. It is expected that this lower-porosity design will continue to work well for even more severe snow events or for successive snow events occurring during the same winter. The approach advocated in the present study allowed making general recommendations for optimizing the design of lower-porosity plastic snow fences. This approach can be extended to improve the design of other types of snow fences. Some preliminary work for living snow fences is also discussed.

Another major contribution of this study is to propose, develop protocols and test a novel technique based on close range photogrammetry (CRP) to quantify the snow deposits trapped snow fences. As image data can be acquired continuously, the time evolution of the volume of snow retained by

a snow fence during a storm or during a whole winter season can, in principle, be obtained. Moreover, CRP is a non-intrusive method that eliminates the need to perform man-made measurements during the storms, which are difficult and sometimes dangerous to perform. Presently, there is lots of empiricism in the design of snow fences due to lack of data on fence storage capacity on how snow deposits change with the fence design and snow storm characteristics and in the estimation of the main parameters used by the state DOTs to design snow fences at a given site. The availability of such information from CRP measurements should provide critical data for the evaluation of the performance of a certain snow fence design that is tested by the IDOT. As part of the present study, the novel CRP method is tested at several sites.

The present study also discusses some attempts and preliminary work to determine the snow relocation coefficient which is one of the main variables that has to be estimated by IDOT engineers when using the standard snow fence design software (Snow Drift Profiler, Tabler, 2006). Our analysis showed that standard empirical formulas did not produce reasonable values when applied at the Iowa test sites monitored as part of the present study and that simple methods to estimate this variable are not reliable. The present study makes recommendations for the development of a new methodology based on Large Scale Particle Image Velocimetry that can directly measure the snow drift fluxes and the amount of snow relocated by the fence.

1. INTRODUCTION

Blowing snow that reaches the road and the accumulation of snow on the roadway (snow drifting) are two of the main causes for reduction in driver visibility and safety and, ultimately, for increased accidents during the winter season. Large drifts of snow can reduce the effective road width. Blowing snow crossing the road can significantly impair drivers' visibility. Most blowing snow travels within 2 m from the ground surface. Blowing snow is the main cause of ice cover formation on roads in wind-exposed regions. Roads situated in regions prone to severe snow blowing and drifting are characterized by high snow removal and road maintenance costs. Removing mechanically snow from the roadways is very costly due to equipment expenses and salaries of the snow removal crews. Additionally, mechanically removing the snow results in lower usage of the roads between the time the snow deposits and the time the snow is removed (e.g., see Tabler, 1991, and 2003; Iowa DOT: Iowa's Cooperative Snow Fence Program, 2005; Sanudo-Fontaned et al., 2011).

Ideally, roads are designed to facilitate accumulation of snow in the ditches, while the snow moving over the road should be prevented from starting to accumulate on the road. Designing roads such that snow drifts never accumulate on the roadways is not always possible. The use of snow fences, if properly designed (e.g., in terms of position, height, orientation, porosity, bottom gap), can result in a dramatic decrease of problems related to snow blowing and drifting by slowing down the speed of the snow particles and promoting deposition of snow particles behind (downwind of) the fence (Figure 1). In this regard, snow fences are just a particular type of surface-mounted porous barriers subject to an incoming flow containing particulates. One of the main design parameters of such barriers is the porosity, which is the ratio of open area of the barrier/fence to its total frontal area. Similar barriers are widely used as windbreaks (Dong et al., 2010) to reduce the flow velocity within a given region so that one can mitigate the damage caused by wind (e.g., region downwind of a porous barrier can act as a shelter offering protection from hurricanes; see also Raine and Stevenson, 1977) and wind-blown sediments/particulates (e.g., the porous barrier can control where sand shifts or snow drifting occurs), or as an effective way to control aeolian sand transport (Alhajraf, 2004; Saif et al., 2010). This is why such wind barriers are widely used not only in cold areas but also in coastal and arid regions (Anno, 1986; Lee and Kim, 1999; Dong et. al, 2007).

1.1. General comments on snow fence design

Snow fences are generally installed perpendicular to the prevailing wind direction and along the roadway. Snow particles are prone to deposit on the downwind side of the snow fence, where the velocity magnitude is small. The amount of snow that a fence can retain on its downwind side is mainly a function of the fence porosity and the size of the bottom gap. The bottom gap is the open space between the ground and bottom of the porous fence (Figure 2). The role of the bottom gap is to reduce snow accumulation in the immediate vicinity of the fence. The ratio between the height of the bottom gap, G, and the total fence height, H, is an important design parameter controlling the total snow trapping capacity of the fence (Tabler, 2003). Fences can be constructed from several materials (Sañudo-Fontaned et al., 2011). Besides the traditional wood fences, typical materials for fences include metal rails, plastic nets, polymer rails and woven fabric. Fence materials are attached to supporting structures (e.g., posts) made of steel or wood or by using an

especially designed (truss-type) framework set in the ground. Another alternative is the use of living snow fences which consist of trees and/or local grasses planted along the roads (see Nixon et al., 2003). Both structural and living snow fences have advantages and disadvantages, as described in Tabler (1991).
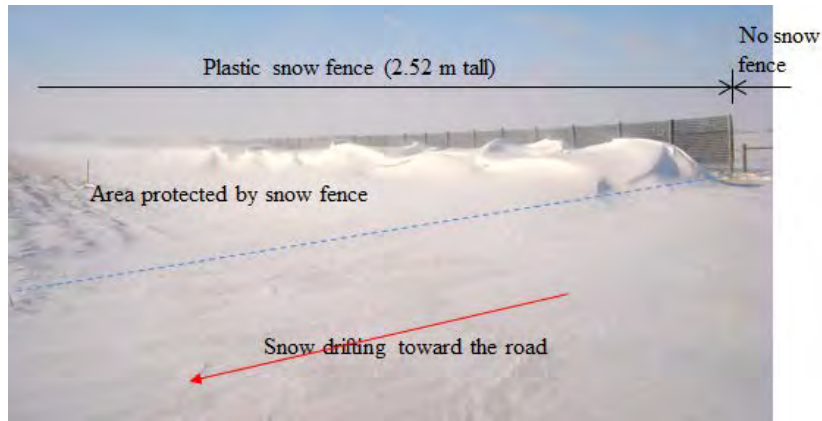

Figure 1. Picture illustrating the effect of placing a snow fence close to a road on snow drifting. The unfenced area on the right is subject to significant snow blowing and drifting toward and over the road, leading to the development of a significant snow deposit on the roadway. On the left side, which is protected by a plastic snow fence, snow accumulates on the downwind side of the fence but the snow deposit close to the roadway is negligible. The picture was taken at the site situated on Highway 20, Williams, Iowa, U.S.

Several studies (e.g., Seginer, 1972; Heisler and Dewalle, 1988; Dong et al., 2007 and 2010) have shown that the fence porosity is the main parameter determining the degree of velocity reduction and turbulence amplification induced in the wake of long fences defined as fences whose length is much larger than their height). In the particular case of snow fences, the characteristics of the turbulent velocity field behind the fence controls how much snow will deposit and over what distance significant snow deposition will occur. Dong et al. (2010) found that while decreasing fence porosity results in a decrease of the mean streamwise velocity behind the fence, the mean velocity fluctuations in the vertical direction can increase significantly for low porosities. Their study proposed an optimal porosity of about 20% based on the fact that for lower porosities the turbulent intensity, Reynolds stresses and vertical velocity behind the fence start increasing rapidly with further decrease in fence porosity. Lee and Kim (1999) found that snow fences with a porosity of about 40% generate wakes with relatively small turbulent fluctuations and a relatively large reduction of the velocity magnitude with respect to that of the incoming wind. Experimental studies have shown that above a critical value of the porosity, there is no recirculation region behind the fence as observed in the case of a solid (zero porosity) fence. The threshold porosity value was found to be between 30% and 35% in the studies of Castro (1971), Perera (1981), and Lee and Kim (1999). This also means that there is no well-defined recirculation region (bubble) in the wake of the porous fence if the fence porosity is larger than 30%. In the case of fences that are not directly attached to the bottom surface, the bottom gap is the other design parameter. Based on a series of laboratory measurements of the wake flow past porous fences with varying bottom gap, Kim and Lee (2002) recommended the use of a bottom gap of height equal to 10% of the fence height for fences with porosity close to 40%. There is wide agreement on the fact that using a

single array of snow fences is less expensive than deploying parallel arrays of smaller-height fences.

Figure 1 clearly illustrates the difference between a road area not protected by snow fences, where snow particles drift toward the road and snow accumulates in the vicinity and over the road, and a neighboring road area protected by a (plastic) snow fence, where snow drifting is much less and snow accumulation in the immediate vicinity of the road and over the road is negligible. These differences substantiate the two main roles of the snow fence which are to retain the blowing snow upwind of the roadway area and to store that snow drift on the landscape. Moreover, snow fences make the roads safer by improving the visibility for drivers. Several states in U.S. (e.g., Minnesota, Wyoming, Utah) have established a clear link between the deployment of snow fences in critical areas of highways and a significant reduction (by about 50%) of the number of serious vehicle accidents associated with snow drifting and blowing. This was accompanied by a major cut in winter maintenance costs, as snow fences lower the cost of snow removal and decreases freezing effects on the roadway (Tabler, 1991).

The main parameters that characterize a snow fence are the fence porosity, P, the fence height, H, and the bottom gap, G (Figure 2). Snow Fence Guides (e.g., Tabler, 1991 and 2003; Iowa DOT: Iowa's Cooperative Snow Fence Program, 2005) provide design recommendation regarding the setback distance from roads, the porosity, and the bottom gap. For structural snow fences, the snow drift extends downwind generally up to 25 to 35 times the fence height, while the height of the drift is comparable to that of the fence (Tabler, 2003). Most conventional snow fence designs recommend the use of structural snow fences with porosity close to 50%. To maximize the snow storage capacity of such fences, it is generally recommended the bottom gap under the fence is equal to 10% of the total fence height, H=h+G. A main design challenge occurs when the right of way of the road to be protected is too narrow to allow placing the snow fence at the distance from the edge of the roadway recommended by the guidelines. There are two main ways to address this problem.

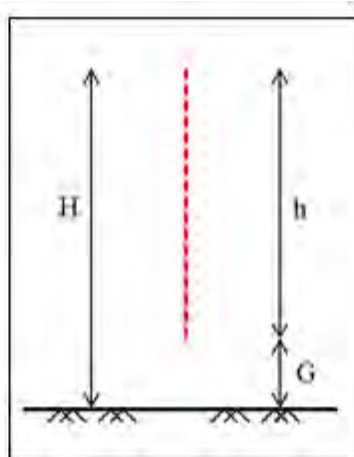Figure 2. Sketch showing main variables characterizing a porous fence: total fence height (H), net fence height (h) and bottom gap (G).

The first option is to install fences of complex design. For example, one solution is to use the so-called 'blower' snow fences that have lateral fins attached obliquely to the vertical support (Haniu

et al., 2009). The fins play the role of wind straightening vanes. Another design approach involves the use of metallic snow fences with airfoil snow plates placed close to the roadway (García Nieto et al., 2010). Such designs were successfully tested in field conditions, especially in Asian countries. The main reasons are that manufacturing them is fairly expensive compared to conventional designs (e.g., plastic snow fences in most U.S. states). In some countries the deployment of heavy and rigid structures very close to the road is considered unsafe.

The second option is to modify the porosity, bottom gap and height of conventional snow fences (e.g., inexpensive wood lath fences or lightweight plastic snow fences mounted on a welded fence) such that they lead to more efficient snow trapping in road areas with narrow right of way. Fences with a lower porosity induce a larger downwind wake region where the smaller velocity magnitude favors snow deposition compared to higher-porosity fences. The capacity of the fence to retain snow also scales with the fence height. Meanwhile, it is highly likely that, to work efficiently, these lower-porosity fences should be designed with a larger bottom gap than that of standard higher-porosity fences. This is needed because once the bottom gap becomes filled with snow during a large snow event the snow retention capacity of the fence diminishes drastically.

In the present study we will focus on the second option which, if proven successful, is a more economical and general solution to protect regions with narrow rights of ways against adverse effects associated with snow drifting. Given that lightweight plastic snow fences are among the most inexpensive and common types of snow fences, in our study we will focus on this type of snow fences. The optimization strategy is to reduce fence porosity while, at the same time, increasing the bottom gap such that to augment the snow retention capacity of the fence and diminish the distance away from the fence over which snow deposition is significant. This will allow using lower-porosity fences in regions with narrower straight of ways. In the present study we focus on commercially available lightweight plastic snow fences mounted on a welded wire mesh. This solution is adopted in many regions of U.S. because such fences can be easily and rapidly deployed or removed from the field.

1.2. Field monitoring of the performance of snow fences

In terms of assessing the performance of a snow fence, field monitoring of the snow deposits especially after major snow storms is essential. The most important information that needs to be obtained from the field monitoring is the snow deposition pattern that can be obtained from surveys, the maximum distance from the fence where snow accumulates on the downwind side and the volume of snow retained by the fence. Using such information collected over multiple major snow events IDOT engineers can determine whether the snow fence that they designed performs satisfactorily at the location where it was deployed. Moreover, testing several different designs at the same site allows identifying the best design among the ones tested. This provides the most reliable method to optimize the design of a certain type of snow fence.

Common operations during various phases of the construction of civil works (such as buildings, roadways, railways and mining) are cutting and filling materials in various areas of the construction sites. Estimation of the volume prior to execution of these works is essential for planning and management of the construction phases. These estimations are also needed for evaluation of the volumes dislocated by natural hazards such as land-slides and snow avalanches

15

or that retained upwind and downwind of obstructions such as snow fences. In general, the evaluator needs to tradeoff between efficient volume calculation and the targeted accuracy of the volume estimation as the latter is commensurate with the number and the spatial distribution of observations (control points) acquired over the surface of the volume (Soole and Poropat, 2000). It is obvious that the use of more points provide better representation of the terrain, therefore searching for fast, safe, and cost-efficient methods for the surveys are continuous (Yakar and Yilmaz, 2008).

The conventional measurement technology for estimation of volumes of materials dislocated in natural environments was the theodolites combining optical and mechanical components assembled with high precision (Gannett, 1906). Currently, this approach is increasingly replaced with non-intrusive survey methods based on electromagnetic, optical, and acoustic-based principles. Contemporary measurement technologies for representation of the terrain topography include modern versions of the theodolite (a.k.a. total station), real time kinematic (RTK) and terrestrial light detection and ranging (LIDAR). Contemporary total stations are instruments measure angles and distance to targeted points using electro-optical scanning mechanisms and microwave or infrared carrier signals that are reflected by the targets. RTK is one of the recent surveying techniques using satellite-based positioning system. Neither of these instruments can measure simultaneously multiple points over the volume surface. Moreover, there is need for a physical presence at the measurement point location. For total station an operator and auxiliary person carrying a graduate rod or a reflector are engaged. For RTK measurements, the instrument is sequentially placed at each surveying points therefore the survey can be conducted by a single person. Terrestrial (ground-based) LIDAR is a laser-based remote sensing technology that is capable of producing cloud of points over the surveyed volume without the need of an operator or sensor positioning at the measurement points. Limitations of this technique are related to its high cost and limitations in making measurements over rough or highly reflecting surfaces and being dependent on the weather conditions.

The brief review of the above technologies indicates that while each of them have uniquely strong capabilities (theodolite – high accuracy; RTK – improved operational aspects; LIDAR - multiple measurement points remotely acquired) they are expensive in terms of equipment or personnel involved in operations, especially in areas where the access is risky or difficult. Consequently, the quest for new accurate, cost- and operational effective means for conducting terrestrial survey is on-going. One of the new candidate currently under scrutiny is terrestrial photogrammetry, a pre-digital era instrument created in mid-nineteenth century (http://en.wikipedia.org). Since the 1930s, most of the topographic and thematic maps produced in the United States have been made according to aerial photography and photogrammetric methods (Matthews, 2008). The main methods used in the present study to determine snow deposits are based on RTK and close-range photogrammetry (CRP). As use of CRP for determining snow deposits is new, we provide below some background on the main features of this method and on its advantages and limitations.

Photogrammetry is the art and science of obtaining reliable three-dimensional data from two or more photographs (Kunapo, 2005). The technique has emerged from radiolocation, multilateration and radiometry while its 3-D positioning estimative component (based on modeling) employs methods related to triangulation, trilateration and multidimensional scaling (Yakar and Yilmaz, 2008). Scaling the 3D location of each point in the images requires few reference points to be

surveyed at the measurement site (a small fraction from those needed by the above-reviewed methods). However, photogrammetry can produce stand-alone measurements in situations where the terrain topology or objects that cannot be physically measured (Yakar, 2009). Photogrammetry is 22% faster, 13% more accurate, and 33% cheaper in average compared to the classical method (Yakar and Yilmaz, 2008). Photogrammetric acquisition and processing can be done by one person.

Depending on the recording camera location, photogrammetry can be divided into two basic categories traditional (or aerial) and nontraditional (or close-range). In aerial photogrammetry the camera is typically mounted on an aircraft and pointed vertically towards the land (Matthews, 2008). Multiple overlapping images of the land are taken as the aircraft flies along a flight path. These images are processed in a stereo-plotter (an instrument that lets an operator see two images at once in a stereo view). Advances in digital imagery and photogrammetric software during the last two decades have enabled the use of photogrammetric methods over a wider range of applications. At the same time, reducing the equipment cost and decreasing the computing time have caused the entire photogrammetry process more cost-effective. These advances have revolutionized both aerial, but especially, terrestrial measurements by removing many of the rigors of traditional aerial photogrammetry, thus moving stereoscopic image collection from the hands of the photogrammetric expert to those of field personnel. When images are taken from close proximity, the technique is labeled as Close Range Photogrammetry (CRP). In CRP the camera is close to the object (less than 300 m) and is typically hand-held or set on a tripod or a pole (Matthews, 2008). Usually this type of photogrammetry is non-topographic - that is, the output is in from of drawings, 3D models, measurements and point clouds not a topographic product such as terrain models or topographic maps. CRP is typically reconstructing the actual terrain topography using a pair of photos of the same area (or object) taken from slightly different locations. If multiple overlapping images are taken from different angles, an even better resolved 3D reconstruction of the objects can be obtained (Kraus, 1992; Wolf and Dewitt, 2000; Cooper and Robson, 1996).

CRP images are increasingly applied to digitally measure and subsequently model volumes of buildings, engineering structures, forensic and accident scenes, mines, earth-works, stock-piles, archaeological artifacts, and natural disasters (see www.photogrammetry.com). Given that images can be acquired with conventional cameras, the advent of low-cost, high-resolution cameras commercialized in recent years has produced an increased in popularity of CRP for a variety of practical applications. Using CRP in conjunction with high resolution, time-lapse photography sheds new insights into the understanding of complex process such as surface erosion and other geomorphic processes at spatial and temporal scales that are difficult to measure using classical methods. Consequently, this technology has broad applicability for tracking in space and time ecosystem and physical processes research occurring in nature. For example, capturing the rock characteristics (e.g., Sturzenegger and Stead, 2009), finding the potential erosion gully (e.g., Marzolff and Poesen, 2009), and observing the kinematics of a landslide (e.g., Baldi et al., 2008).

Besides using some of the more classical methods mentioned before, this study presents a new application of CRP that was not previously tested: mapping of volumes of snow accumulations. In particular, this study reports on the capability of CRP to map snow accumulations produced by snow fences installed for mitigation of drifting snow. Mapping of snow deposits using CRP entail

several complexities that are not typically involved in conventional CRP applications. Most of the complexities stem from the lack of texture and of control points over the snow surface. Part of this study we investigate the complexities of this unique CRP case study and propose solutions for practical implementation of this methodology by the IDOT.

2. INVESTIGATING APPROACH TO OPTIMIZE LIGHTWEIGHT PLASTIC SNOW FENCE DESIGN AND TO QUANTIFY VOLUME OF TRAPPED SNOW

A joint approach based on multi-year monitoring of snow deposition and performance of several snow fence designs at the field site and numerical simulations was adopted to assess the efficiency and improve snow fence design. This study focuses on improving the design of lightweight porous fences. The standard design of these snow fences assumes the porosity is close to 50%. Previous studies have shown that the major change in wake structure (recirculation region similar to wake past solid fences vs. no recirculation region) occurs for fences with a porosity close to 30%. These studies have also shown that for constant fence height, h, fences with a lower porosity may retain more snow and the region of significant snow deposition may be extending less away from the fence compared to fences with a higher porosity. Based on these observations, the present study focuses on identifying optimum designs for plastic snow fences with a porosity, P, of 30% and 50%. A two-year monitoring campaign was undertaken.

During the first year of monitoring, the goal was to identify the snow fence with the best performance among several snow fence designs with P=50%. Three different designs (A1, A2 and A3) of fences with P=50% and varying relative bottom gap G/H were tested in the field. The design that showed minimal snow deposition within the bottom gap, minimum length of the snow drift deposit and maximum volume of snow drift during the large snow events occurring during the first winter was identified as best design.

In parallel, 2-D Reynolds-Averaged Numerical Simulations (RANS) were conducted using the geometry of the three snow fences monitored in-situ. A commercial CFD software was used to perform steady state simulations of the air-flow around the snow fence for a given topography and fence design. It was found that the best design was the one for which the streamwise extent and width of the region of small velocity magnitude situated close to the bare ground were the largest. This region corresponded approximately to the one where significant snow deposit occurred during the large snow events. Based on this criterion, several other designs for fences with P=50% were tested based only on numerical simulations. None of the new designs appeared to perform significantly better than the one identified as best design among the three designs tested in the field. In fact, many of the new designs performed visibly worse. Then, more than 10 designs of fences with P=30% were tested. In particular, in two series of simulations, the height of the bottom gap, G, was varied while maintaining the fence height h and, respectively, the total fence height, H=h+G, constant. Based on analysis of the velocity magnitude fields, two candidates for best design of fences with P=30% were identified. These designs are denoted B1 and B2 in the study.

During the second year, the performances of the best fence design with P=50% and the two candidates for best design for fences with P=30% were monitored in the field using the same criteria as those described for the monitoring campaign undertaken during the first year. As the

discussion of the results will show, the overall performance of both proposed designs with P=30% was better than that of the best design identified for fences with P=50%.

In terms of site monitoring and direct measurements of the snow deposits, the experimental protocol was perfected through successive field campaigns to include the steps illustrated in Table 1. The site was visited before the winter season at the time of the installation of the experimental equipment for continuous monitoring. During the initial site visit, a RTK bare-ground survey was conducted to determine the coordinates of marker poles at its base (GCPs). The coordinates of each camera position (horizontal and vertical) were calculated using RTK survey and measuring tapes along with direct readings of the camera inclination angles using Angle Meter iPhone app. These angles are needed to calculate parameters for CRP external calibration. The height of each marker poles from its base was physically measured using measuring tapes. After equipment installation, provisions were taken to secure the equipment and ancillary supports against wind-induced vibrations or other incidental effects. The initial visit concluded with the acquisition of a set of images with the web-cameras to make sure that the system is ready for continuous operation.

Table 1. Experimental protocols.

I. Pre-winter survey (bare-ground)	II. Synoptic measurements (P1)	III. Continuous monitoring (P2)	IV. CRP analysis
1. RTK survey a. marker poles b. additional GCPs 2. Tape measurements of marker pole height	1. RTK survey 2. Total station 3. Tape measurements of snow depth at marker poles 4. Video and still photos of various site components	1. Image acquisition with a pair of web-camera (sampling at 1 hour apart) 2. Local weather monitoring using third party sources	1. Continuous using marker poles as GCPs 2. Synoptic using additional GCPs survey in situ
Baseline for snow deposit volume estimation	Calibration/validation of experimental volume mapping tools	Continuous CRP and securing information at the site at all times	Snow volume estimation and validation

2.1. NUMERICAL MODEL

2.1.1. Governing equations and boundary conditions

The RANS numerical simulations of the airflow past the porous snow fence were performed using the Computational Fluid Dynamics (CFD) package STAR-CCM+, developed by CD-Adapco. This CFD software contains an advanced mesh generator with automatic mesh refinement capabilities that offers lots of flexibility in terms of resolving the boundary layers close to solid surfaces in very complex domains. The governing Navier Stokes equations are:

$$\frac{\partial}{\partial x_i}(\rho u_i) = 0$$

$$\frac{\partial}{\partial t}(\rho u_i) + \frac{\partial}{\partial x_i}(\rho u_i u_k) = -\frac{\partial p}{\partial x_i} + \frac{\partial}{\partial x_j}\left[(\mu + \mu_t)\left(\frac{\partial u_i}{\partial x_j} + \frac{\partial u_j}{\partial x_i}\right)\right] \qquad (1)$$

where u_i is the Cartesian velocity component along the i direction, v is the molecular viscosity, p is the pressure, ρ is the density and μ and μ_t are the dynamic and turbulent viscosity, respectively. The two-layer k-ε turbulence model (k is the turbulence kinetic energy and ε is the turbulent dissipation rate) was used to estimate the eddy viscosity:

$$\mu_T = \rho C_\mu \frac{k^2}{\varepsilon} \qquad (2)$$

The transport equations used to calculate k and ε are:

$$\frac{\partial}{\partial t}(k) + \frac{\partial}{\partial x_i}(u_i k) = \frac{\partial}{\partial x_j}\left[\frac{1}{\rho}(\mu + \frac{\mu_t}{\sigma_k})\left(\frac{\partial k}{\partial x_j}\right)\right] + G - \varepsilon$$

$$\frac{\partial}{\partial t}(\varepsilon) + \frac{\partial}{\partial x_i}(u_i \varepsilon) = \frac{\partial}{\partial x_j}\left[\frac{1}{\rho}(\mu + \frac{\mu_t}{\sigma_\varepsilon})\left(\frac{\partial \varepsilon}{\partial x_j}\right)\right] + C_{\varepsilon 1}\frac{\varepsilon}{k} - C_{\varepsilon 2}\frac{\varepsilon^2}{k} \qquad (3)$$

where G is the turbulence production term and the model coefficients have the following values:

$$\sigma_k = 1.0 \qquad \sigma_\varepsilon = 1.3 \qquad C_{\varepsilon 1} = 1.44 \qquad C_{\varepsilon 2} = 1.92 \qquad C_\mu = 0.09 \qquad (4)$$

The two-layer k-ε model was used in the present RANS simulations, in which the mesh was sufficiently fine to resolve the flow within the viscous sublayer. The flow domain is divided into two regions: an inner layer where a one-equation turbulence model is used and an outer layer where the above (high-Reynolds-number) version of the k-ε model is used. The inner-layer model solves only the k-equation while the ε-equation is replaced by

$$\varepsilon = \frac{k^{3/2}}{l_\varepsilon} \qquad (5)$$

The eddy viscosity is obtained from

$$\mu_T = \rho C_\mu \sqrt{k l_\mu} \qquad (6)$$

instead of equation (2). Here l_ε and l_μ are length scales which are a function of the turbulence Reynolds number, $R_T = \frac{\sqrt{k}n}{v}$. Their expressions are:

$$l_\mu = C_1 n \left[1 - \exp\left(-\frac{R_T}{A_\mu} \right) \right]$$

$$l_\varepsilon = C_1 n \left[1 - \exp\left(-\frac{R_T}{A_\varepsilon} \right) \right] \qquad (7)$$

where n is the normal distance from the (nearest) wall, $C_1 = \kappa C_\mu^{-3/4}$, so as to obtain a smooth eddy-viscosity distribution between the inner and the outer layers, $\kappa = 0.418$ is the von Karman constant, $A_\varepsilon = 2C_1$ and $A_\mu = 70$. Besides its robustness, an advantage of the two-layer model is that it does not require a boundary condition for ε at the wall.

In the constant-density RANS simulations performed in the present study, the diffusion terms were discretized using a second-order-accurate central scheme and the convective terms were discretized using the second-order upwind scheme. The first-order upwind scheme was used to discretize the convective terms in the transport equations for the turbulence variables. The source terms in the transport equations were treated implicitly. As only steady state RANS simulations were performed, the unsteady term in the momentum equations and in the transport equations for the turbulent variables was equal to zero. The segregated flow solver uses a cell-centered finite-volume method in which the gradients of the variables are computed by means of Green-Gauss' theorem. The SIMPLE algorithm was used to solve the discretized Navier-Stokes equations.

A slip (symmetry) boundary condition was used at the top boundary for the velocity. The bottom boundary and the fence surfaces were treated as no-slip (zero velocity) boundaries. The turbulent kinetic energy was set equal to zero at these boundaries. A standard mass outflow boundary condition was used at the downstream boundary. The turbulence variables were extrapolated at the exit and on the top boundary. The distributions of the mean velocity and turbulent quantities in the inflow section were obtained from a preliminary simulation of the flow in a straight channel of identical height with periodic conditions in the streamwise direction. This is standard treatment for this type of problems (e.g., see Kirkil and Constantinescu, 2009; Constantinescu et al., 2011). The simulations were started with a zero velocity field in the interior of the domain and with small values for k and ε. As steady-state simulations were conducted, the initial conditions did not affect the final steady solution.

2.1.2. Validation of RANS model for relevant configurations

Before discussing results of RANS simulations performed for the porous fences that were tested in the field as part of the present study, it is important to assess the capabilities of such simulations to predict the mean flow field around porous fences installed in the vicinity of a ground surface. One of the test cases studied experimentally by Huang et al. (2012) is chosen for testing the performance of 2D RANS simulations performed using STAR-CCM+. Besides wind tunnel experiments, Huang et al. (2012) also reported results of a 2D Large Eddy Simulation (LES) performed using a dynamic Smagorinsky model on a relatively coarse mesh containing close to 18,000 grid points. Because the mesh was coarse, wall functions were used in LES. In the present 2D RANS simulations, the viscous sublayer is resolved (no wall functions are used) and the mesh is much finer (400,000 grid points).

The computational domain and the porous fence are shown in Figure 3. The design of the nonuniform porous fence was identical to that used in experiment and the 2D LES of Huang et al. (2012). The incoming flow velocity was U_0=10.6 m/s and the total fence height was H=h=0.06 m. As shown in Figure 3, a nonuniform porous fence was tested. The upper half of the fence was solid, while the lower half of the fence had a porosity P=30%. The height of the fence elements was 0.116H and the opening between two elements was 0.05H. The bottom gap was equal to zero (G=0) and the fence width was 0.02H. The Reynolds number defined with the mean incoming wind velocity, U_0, and the fence height, H, was 41,000. The inflow conditions corresponded to fully developed turbulent channel flow at Re=41,000. The height of the domain was 10H. The nondimensional velocity magnitude flow field, V/U_0, is shown in Figure 3. As expected, a region of low velocity magnitude is generated some distance behind the porous fence, close to the bottom boundary. The flow is deflected upwards and downwards by the upper solid part of the fence.
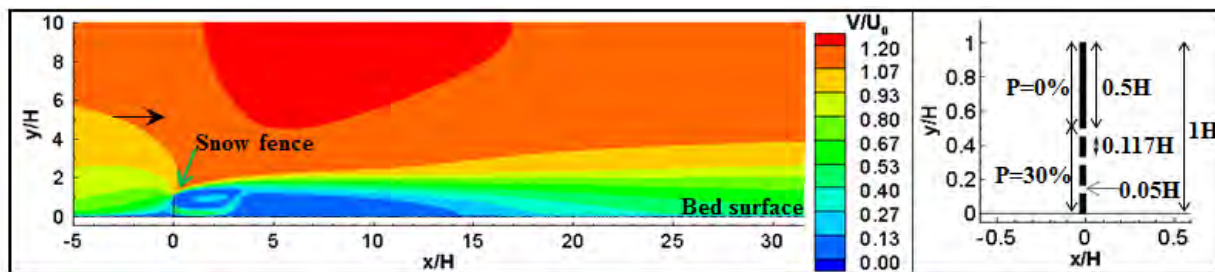
Figure 3. Distribution of velocity magnitude around and downstream of the nonuniform porous fence predicted by a 2D RANS simulation. The simulation corresponds to the experimental set up of Huang et al. (2012). Also shown is a close up view of the porous fence.

The vertical variation of the nondimensional streamwise velocity, u/U_0, is compared in Figure 4 with experimental hot-wire anemometer measurements and results of 2D LES. The comparison is shown at four streamwise locations situated between 1H and 12H downstream of the fence. As expected, the velocity behind the fence is larger in the region with y<0.5H than in the region defined by 0.5H<y<1.5H. This happens because the upper half of the fence is solid while a bleeding flow is present for y<0.5H. Overall, 2D RANS captures fairly well the main features of the measured profiles of the streamiwse velocity at all four locations shown in Figure 4. Moreover, the predictive capabilities of 2D RANS are superior to the ones shown by the 2D LES. There is little doubt that 3D LES performed on sufficiently fine meshes will give mean flow predictions similar or better than 2D RANS. However, for the purpose of the present study that uses the velocity magnitude flow field around the fence to guide selection of candidates for best design for a certain type of snow fence, the level of accuracy of 2D RANS performed using the two-layer k-model is sufficient.
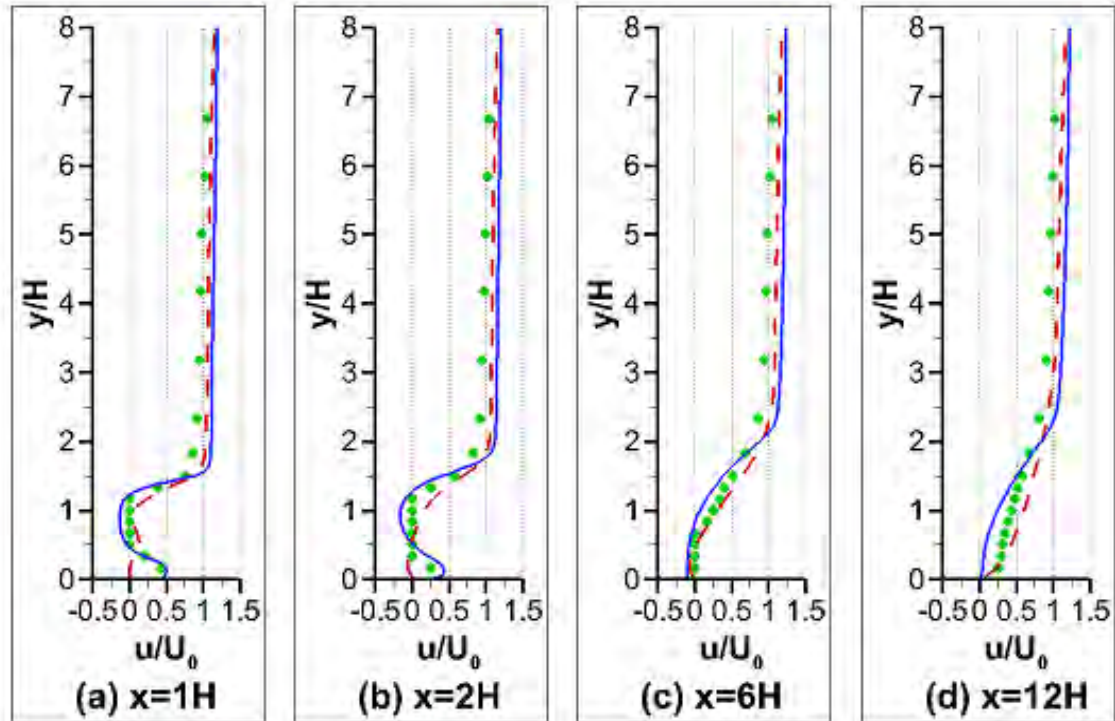
Figure 4. Comparison between mean streamwise velocity profiles predicted by numerical simulations with measured data. a) x=1H; b) x=2H; c) x=6H; d) x=12H. The green symbols correspond to the experimental results of Huang et al. (2012). The solid blue line corresponds to the present 2D RANS results. Also shown with a dashed red line are the results of a 2D LES performed by Huang et al. (2012).

2.1.3. Simulations of flow past porous fences

A first series of 2D RANS simulations were conducted to determine the main differences in the flow patterns among the fences with a porosity of 50% that were tested in the field during the first winter. Results for fences with P=50% discussed in the next section will show that the performance of the snow fence increased as the size of the region of small velocity magnitude forming near the ground downstream of the fence became bigger. This makes sense, as the presence of a region of small velocity magnitude in the vicinity of the ground should favor deposition of suspended particles (snow flakes in the present case) beneath that region. A second series of 2D RANS simulations were conducted with different fence heights and fence gaps for fences with P=30% to identify the best candidates for optimum design for fences with P=30%. Two of the fence designs with P=30% which showed the formation of a relatively large region of small velocity magnitude in the vicinity of the ground, similar to the flow patterns observed for the best design for fences with P=50%, were tested in the field during the second winter. So, the primary role of the RANS simulations is to reduce the number of good candidates for best design to be tested in the field. This is important, as a limited number of different snow fence designs can generally be tested under close to identical conditions at a given field site.

The bare ground profile was obtained from the RTK survey. In all the 2D RANS simulations, the height of the computational domain was 10 m, which is much larger than the height of the largest

snow fence simulated (H<2.5m). In the computational domain, the axis of the fence is situated at x=0 (Figure 5a). The inlet and outlet boundaries are located at 50 m upstream and 157 m downstream of the fence, respectively. The inlet is situated far enough from the region where the presence of the snow fence disturbs the incoming flow field that was assumed to be fully turbulent.

The simulations were performed at a sufficiently high Reynolds number (Re=1.53x10^6, where Re is defined with the mean incoming wind velocity in the direction perpendicular to the road, U=12m/s, and a length scale D=2m corresponding to the average fence height) for the solution to be only weakly dependent on the Reynolds number. A parametric study in which the Reynolds number was varied between Re=1x10^6 and Re=3x10^7 confirmed the distributions of the nondimensional mean velocity components and turbulent kinetic energy were close to independent of the value of Re. This is fully expected for these high values of the physical Reynolds number (Re>10^5, see also Constantinescu et al., 2008, Sinha et al., 2012).

An important feature of the present numerical simulations is that the solid elements defining the fence porosity are resolved by the mesh (Figure 5c). This is a much more correct treatment compared to the common procedure in which a layer of uniform porosity is defined at the location of the fence. Of course, generating a high quality mesh is much more difficult given the presence of very thin solid elements. However, the details of the airflow through the fence and the influence of porosity on the wake flow downstream of the fence are more correctly simulated. In this regard, the use of the local mesh refinement procedure (quadtree-mesh based; e.g. see Kramer and Jozka, 2008) available in the grid generator integrated with STAR CCM+ was critical to successfully generate a high quality mesh. The thickness of the solid elements was identical to that of the plastic snow fence (2 mm). The distance between two solid elements was close to the mean height of the openings in the plastic snow fence tested in the field. Close to 20 grid points were used to resolve the flow through each of the fence openings. The minimum size of the smallest grid cells was about 1 mm. This small size was needed to resolve the flow around the upstream and downstream faces of the thin fence elements. The minimum grid spacing in the wall normal direction was around 1-2 mm, which corresponds to less than five wall units. This fine mesh is required by the two-layer k-ε model that resolves the viscous sublayer. In the regions situated away from the fence and the bare ground, the mean size of the grid cells was increased to about 40 cm. The increase was gradual to maintain a high mesh quality and low stretching ratios (e.g., see Figure 5b).
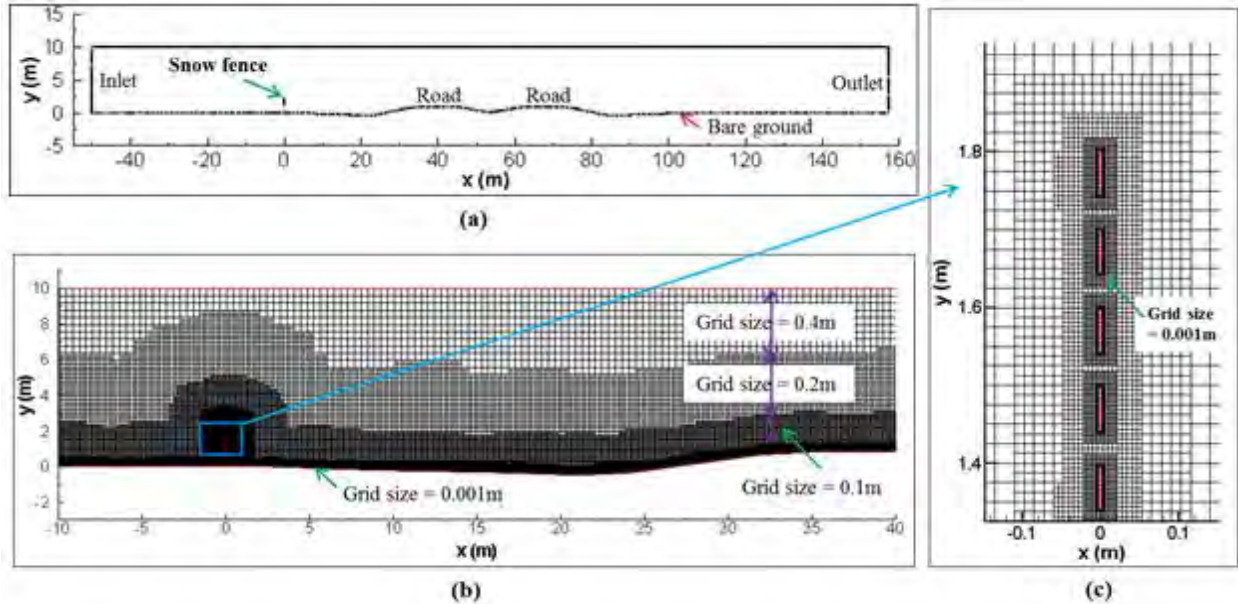
Figure 5. Computational domain and mesh. a) Sketch of the computational domain; b) view of the mesh in the region situated in between the fence and the extremity of the road; and c) detail view showing the local mesh refinement around the fence elements for a fence with a porosity of 30%.

2.2. EXPERIMENTAL METHODS

2.2.1. Field testing site and snow fence deployment

To assess the performance of a snow fence design one needs field observations at a testing site where the flow and topography can be considered to be close to two-dimensional. Moreover, the site should be long enough such that several designs can be tested at once under close to identical conditions in terms of incoming wind direction and magnitude, temperature and snow precipitation during a snow event. For the present study, a field testing site fulfilling the aforementioned requirements and known for severe snow drift problems was identified on Highway 20 near Williams, Iowa, U.S. (Figure 6). Additional similar measurements were performed at the Anamosa site, but the Williams site that allowed testing three different designs under close to identical conditions was the site used to optimize the design of plastic snowfence.

Field monitoring at the site was performed over a three winter seasons. Results from the first two winter seasons were sufficient to propose the new design and check its performance. Results obtained over the last winter season confirmed the performance of the new design. Height, porosity and bottom gap of the plastic snow fence were varied among the different designs tested at the site. During each winter season, three different snow fence designs were tested at the site next to each other. Figure 7 shows the general layout of field testing site and Figure 8 illustrates the corresponding location where three different fences (A1, A2 and A3) were tested during the first winter. The figure also contains views of those three fences. Same layout was used during the second winter, only the fence designs were changed. Figures 9, 10 and 11 show the layout of fence A1, A2 and A3 respectively.

Figure 12 shows a picture of one of the lightweight plastic snow fences installed at the site. The plastic snow fence is attached to a 2 mm diameter welded wire frame. The dimensions of the wire frame structure that supports the plastic fence are presented in Figure 13 and the dimensions of holes in the plastic fence are displayed in Figure 14.

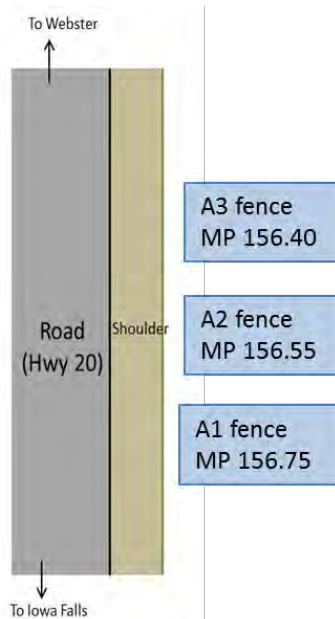Figure 6. Field testing site located on Highway 20, Williams, Iowa, U.S.

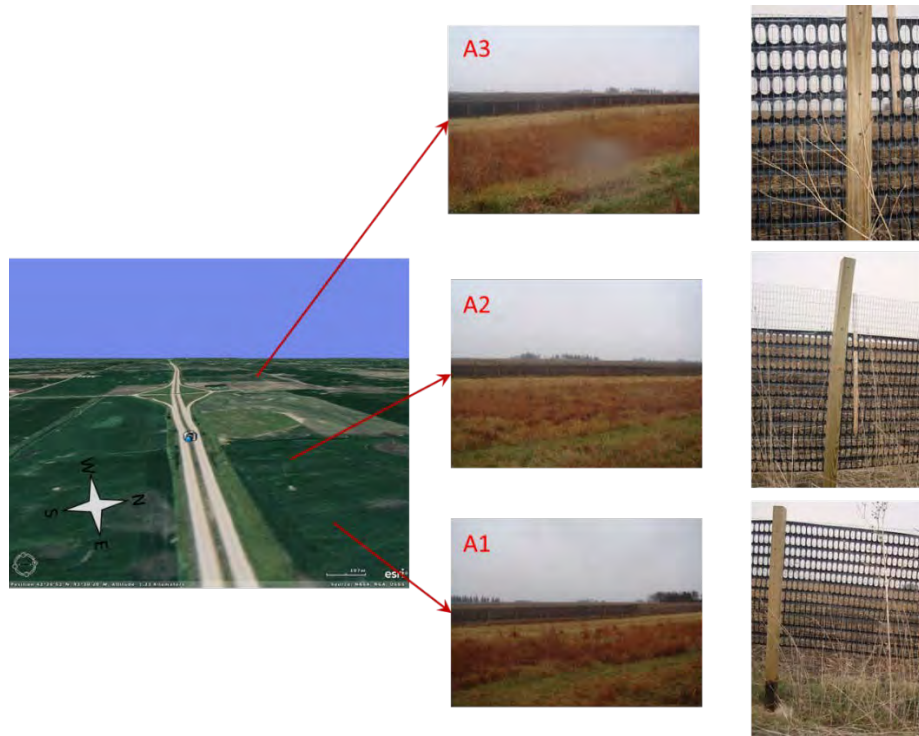

Figure 7. Location of A1, A2 and A3 fences adjacent to each other.

Figure 8. Pre-survey at the Williams site (November 14, 2010).
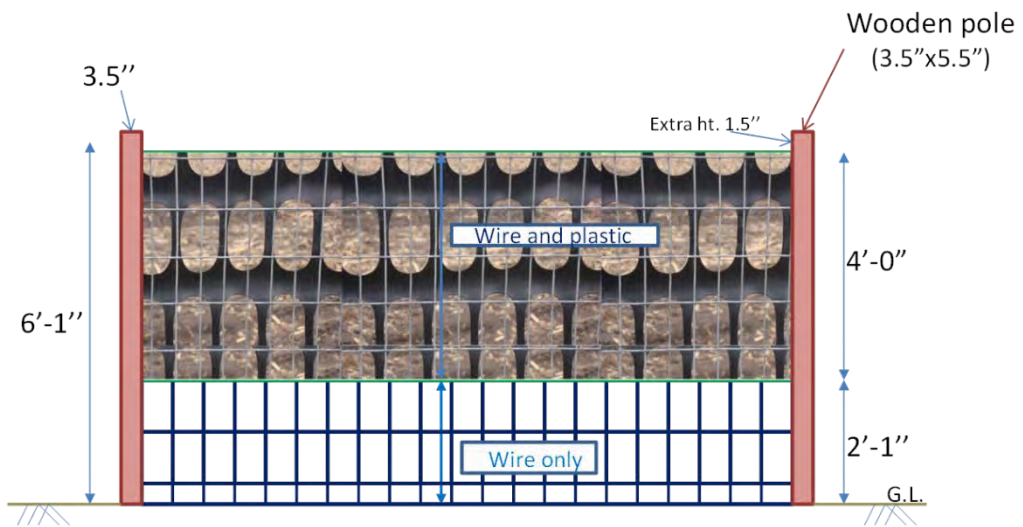
Figure 9. Layout of A1 fence.
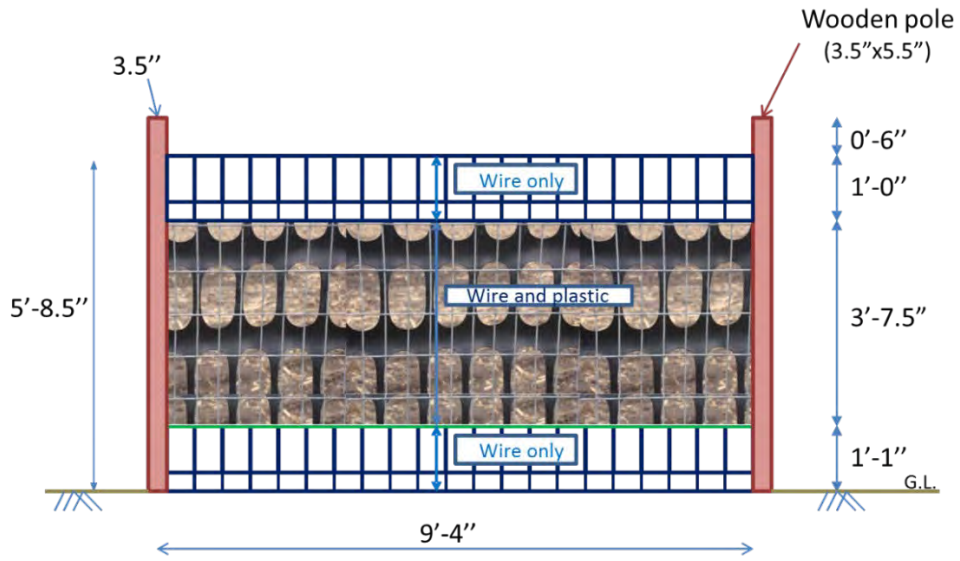
Figure 10. Layout of A2 fence.
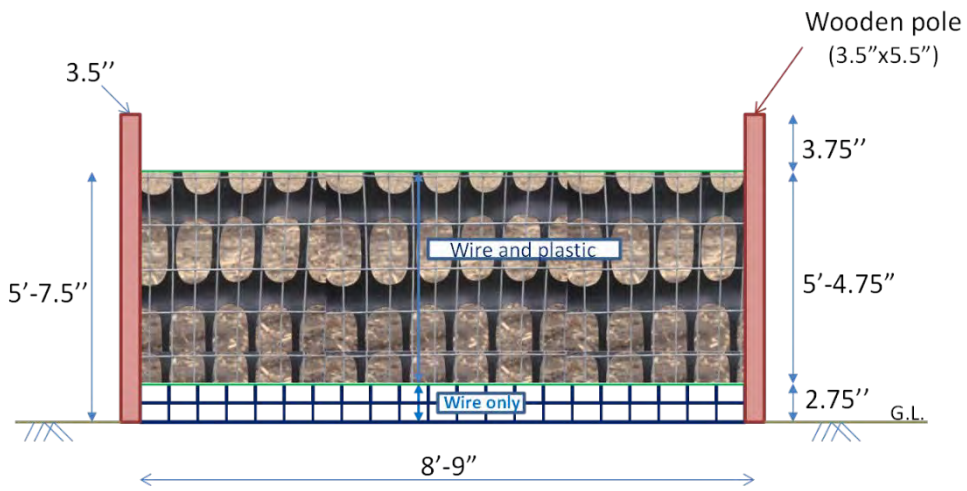
Figure 11. Layout of A3 fence.

Figure 12. (a) View of one of the lightweight plastic snow fences tested at the field site (A1 fence: P=50%, G/H=0.34, H ≅ 1.9); (b) Close view showing the 2 mm diameter welded wire frame used to support the plastic fence.

Figure 13. Detail view showing layout for wire frame supports.

Figure 14. Detail view showing layout of plastic fence.

2.2.2. Meteorological conditions at the site

2.2.2.1. Meteorological conditions throughout a winter season

Meteorological data throughout a winter season were obtained from only one meteorological station located at Iowa Falls situated close to the Williams field site. Time series of wind velocity (both speed and direction) together with snow fall and temperature are presented in Figure 15 and 16 for two different winter seasons.
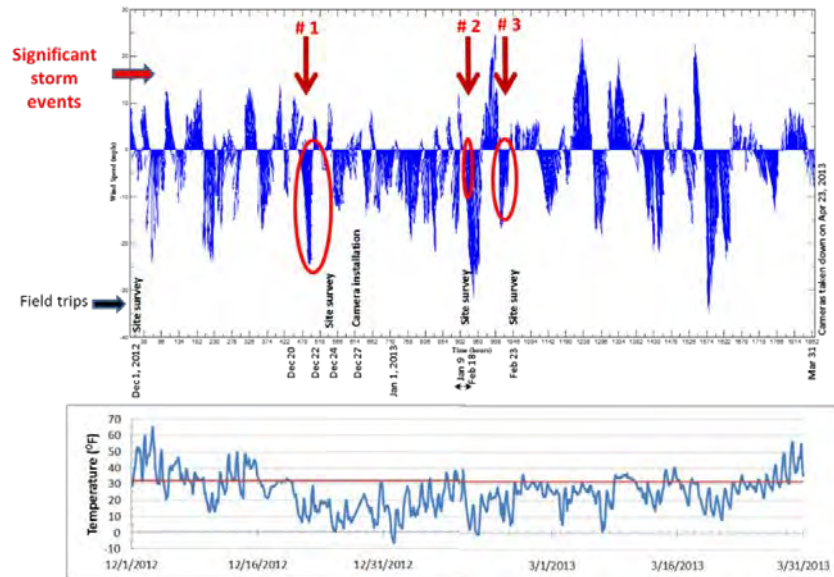
Figure 15. Meteorological data at Iowa Falls near Williams site (December 1, 2012 – March 31, 2013).
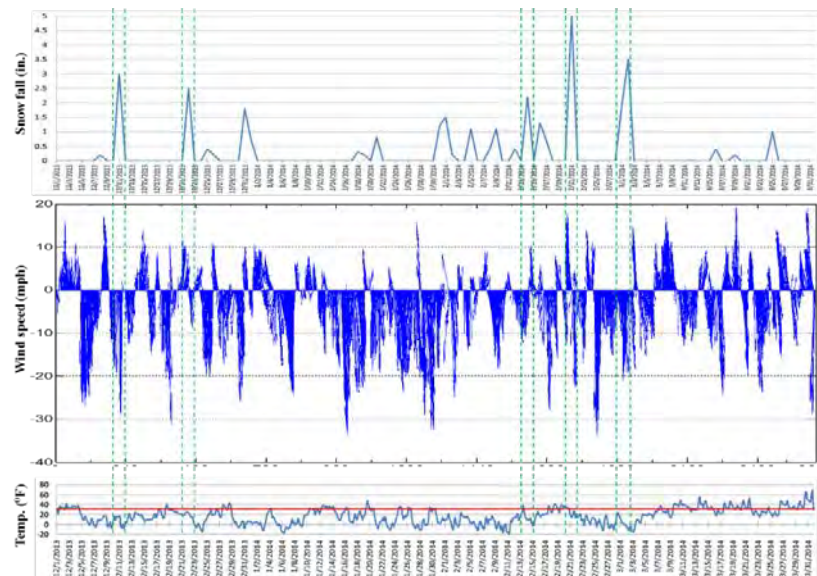
Figure 16. Meteorological data at Iowa Falls near Williams site (December 1, 2013 – March 31, 2014).

2.2.2. Meteorological conditions during a particular event

Wind velocity at 6 different meteorological stations surrounding our monitored area was monitored for different times and different days during a major snow event lasting December 20 to December 24, 2012 as shown in Figure 17 through 24. The instantaneous dominant wind velocity for each particular time was determined by analyzing wind data measured at the 6 surrounding stations. Then, the average dominant wind velocity for the event was calculated based on the instantaneous wind velocities considering 6 surrounding stations, as shown in Figure 25. The dominant wind velocity for the event was found to be 12 m/s. This value was then compared with local meteorological station data located nearby the site at Iowa Falls. The wind speed and direction calculated based on spatial and temporal analysis was found to be close to the temporal wind measurement data at the local station situated in Iowa Falls.

The wind data at the Iowa Falls local station was compared with direct observations made during a visit at the site, as illustrated in Figure 26. The pattern of wind direction noticed in the snow surface during the site visit was found to be close to the dominant wind direction calculated from the meteorological data. Therefore only information from the local station was used to analyze the meteorological data.
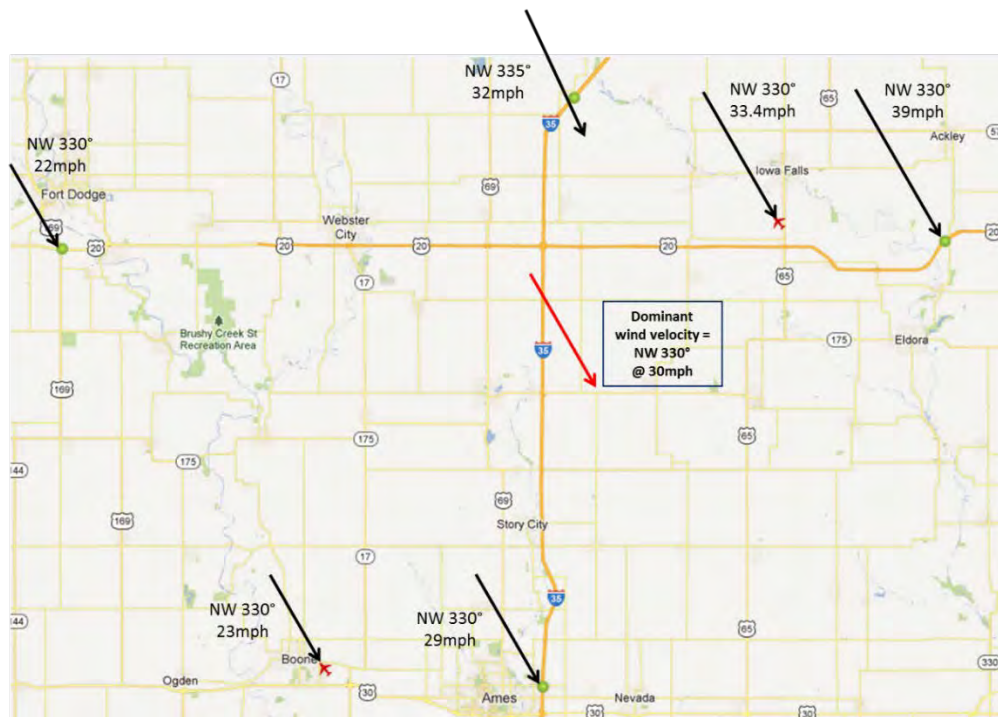

Figure 17. Spatial wind distribution around the monitored area at 9.45am on December 20, 2012.

Figure 18. Spatial wind distribution around the monitored area at 9.45am on December 21, 2012.

Figure 19. Spatial wind distribution around the monitored area at 2.45pm on December 21, 2012.
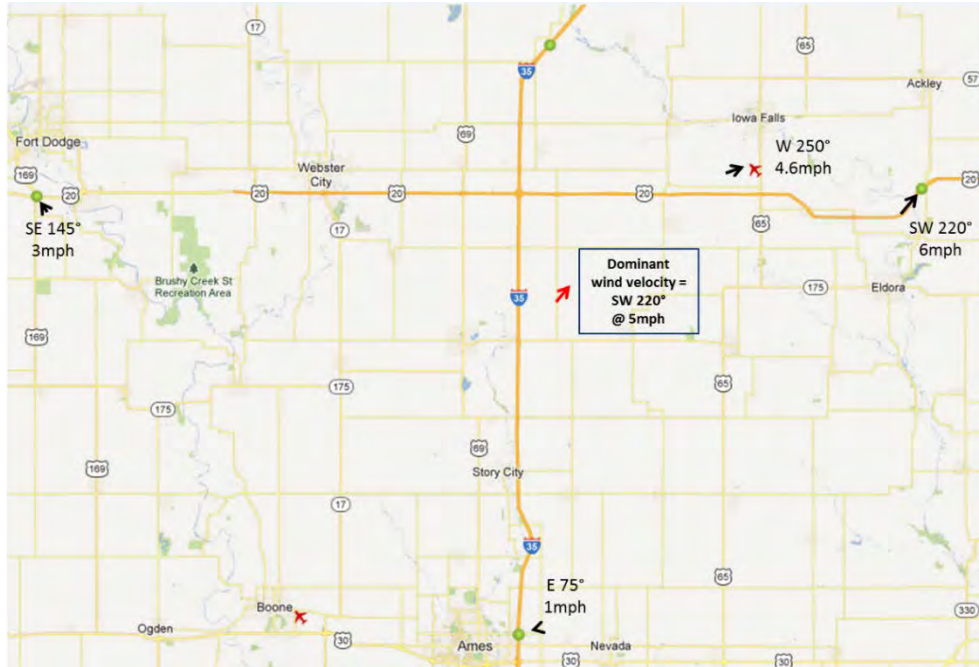
Figure 20. Spatial wind distribution around the monitored area at 9pm on December 21, 2012.

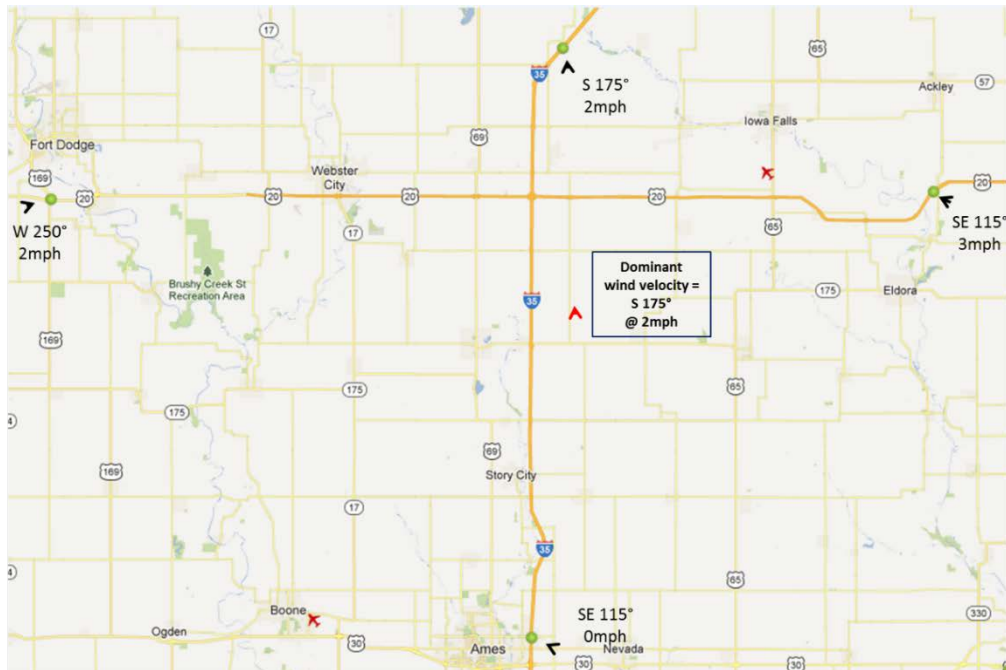Figure 21. Spatial wind distribution around the monitored area at 9.45am on December 22, 2012.

Figure 22. Spatial wind distribution around the monitored area at 4.10pm on December 22, 2012.
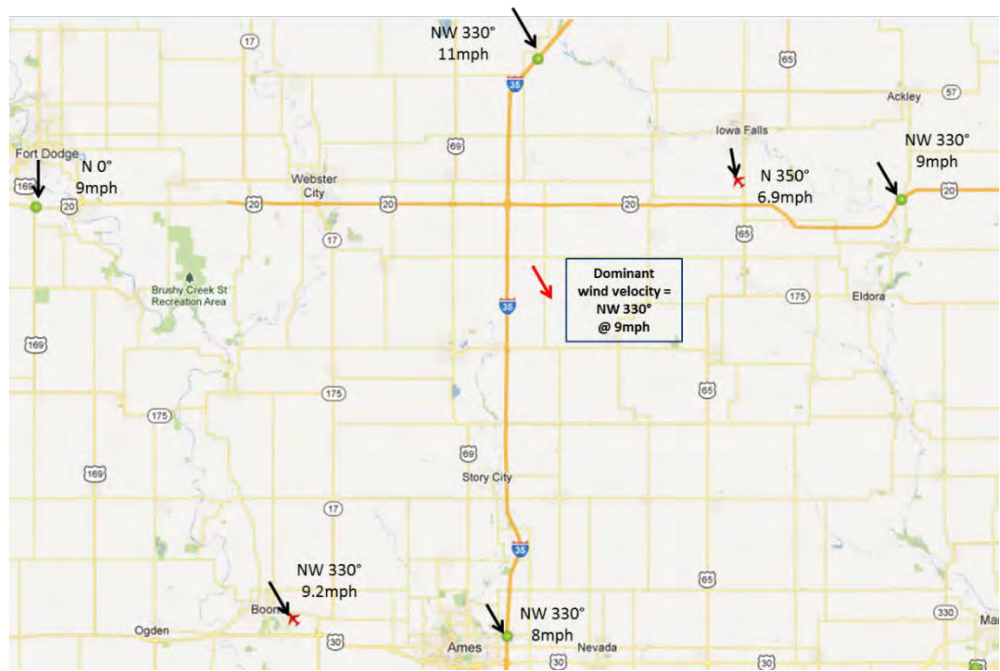

Figure 23. Spatial wind distribution around the monitored area at 10.15pm on December 22, 2012.

Figure 24. Spatial wind distribution around the monitored area at 7.50am on December 23, 2012.
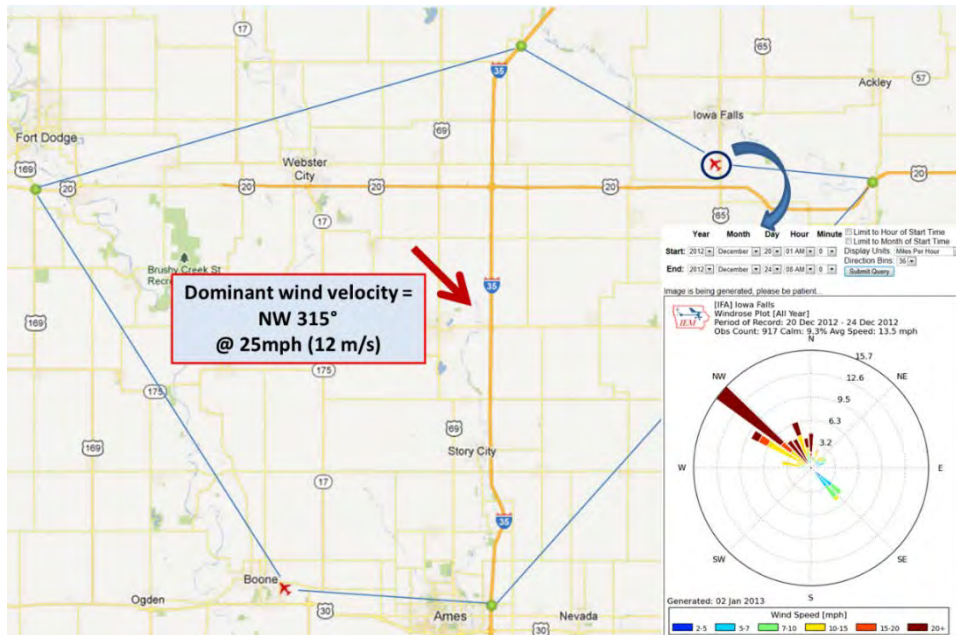

Figure 25. Comparison of areal wind velocity with local data at Iowa Falls Meteorological station for the period of December 20-24, 2012.
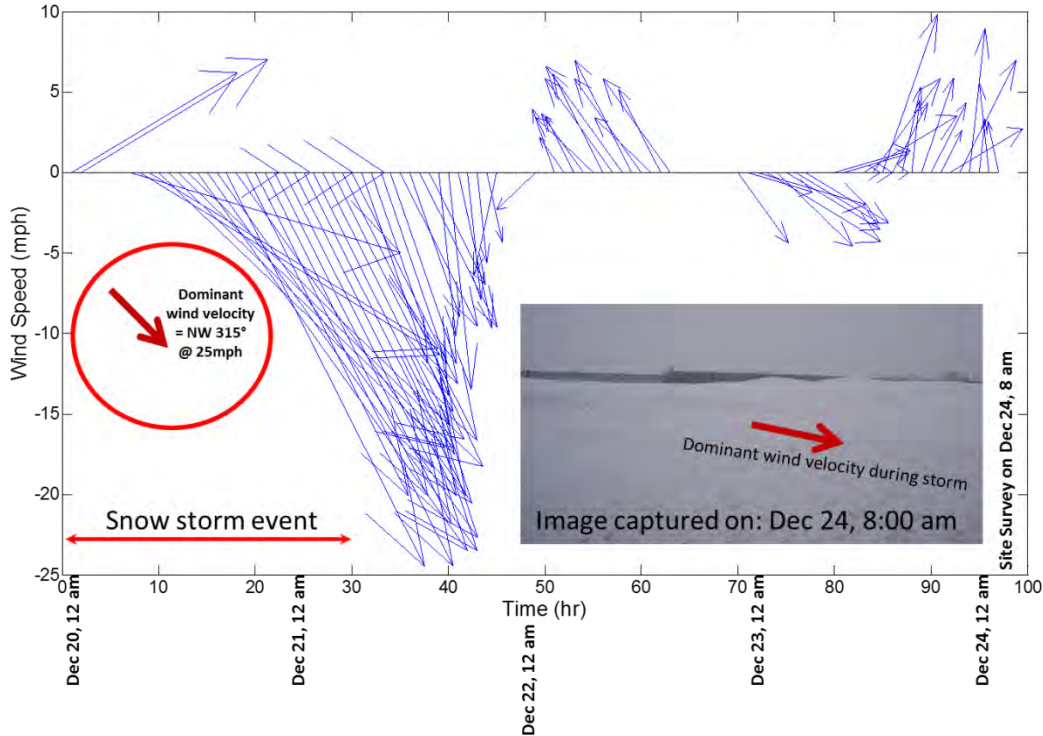
Figure 26. Wind variation during a snow event (December 20, 2012 – December 24, 2012).

2.2.3. Real time monitoring system and field measurements

The field monitoring entailed two sets of observations. The first consisted of a real time observing system aimed to determine if snow deposition accumulated during storms was significant enough to visit the site and conduct detailed measurements of the snow profiles in situ. For this purpose a Moultrie i65 GAME Spy camera and the Moultrie Game Management System were used for continuous imaging of the field test site during the winter seasons (see Figures 27 and 28). The Moultrie camera is equipped with a GPS connect system that sends the images taken in the field over a wireless cellular network to the Moultrie Game Management System website. Pictures can be downloaded online at any time to monitor conditions at the site (see Figure 28). Additionally, the system allows controlling remotely the camera settings via the internet. The system allows both photo mode and video mode and choosing the time interval at which pictures are stored on the website.

Marker poles arranged as shown in Figure 28 were installed at each observation site. The marker poles were needed to assist the topographic surveys. The marker poles were set perpendicular to the road in between the snow fence and the road shoulder. The marker poles were surveyed before the winter season at the ground level. After each storm, the snow deposits were mapped over the imaged area to capture the 3-D topology of the snow deposit produced by the snow fence.

36

Figure 27. Field set-up and information provided by the real-time monitoring system.
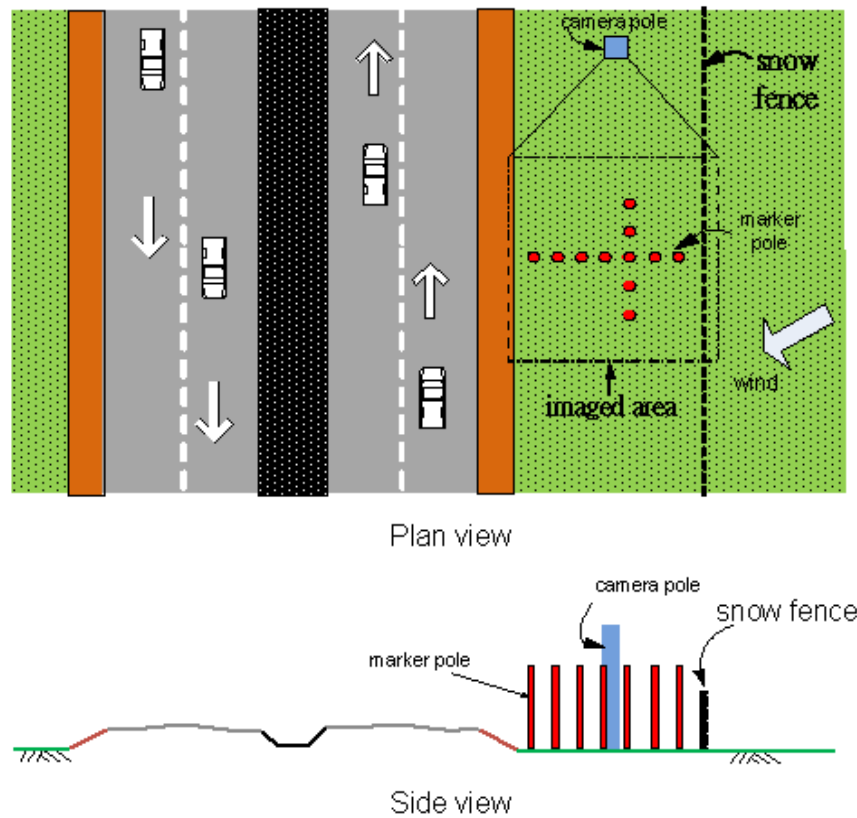

Plan view

Side view

Figure 28. Sketch of the field testing site showing the position of the road, the snow fence, the marker poles and the camera pole used to support the video camera employed for monitoring snow deposits at the site. Drawing is not at scale.

Three Moultrie i65 GAME Spy cameras were used to record images every hour around the region where the marker poles were installed for each of the fence designs tested concomitantly at the site. They provided additional information on the temporal evolution of the snow deposits. However, this information is accessible only after pictures are downloaded during site visits by the monitoring team.

2.2.4. Conventional survey methods (Total station with Tape measurements)

(a)

(b)

Figure 29. Field survey using Total station and measuring tape: a) Total station; b) Direct tape measurement.

Total station surveys with direct tape measurement (Figure 29a) were carried out before the first snow event to determine the bareground profile along the marker poles. For this, the [X,Y,Z] coordinates at top of each marker pole were determined using the Total station and then the height

of each marker pole above the bareground was measured using measuring tape to determine the [X,Y,Z] coordinates of the intersection points. The topcon GTS 235 Total Station was used in this study.

After each snow event, the height of marker poles above the snow surface was measured using a tape (Figure 29b) to determine the [X,Y,Z] coordinates of the intersection points between the snow surface and the marker poles. This was done by using the already known [X,Y,Z] coordinates at the top of marker poles. The underlying assumption was that the marker poles were in a fixed position. Snow profiles in the direction defined by the marker poles installed at each of the three fences tested at the Williams site were calculated using those [X,Y,Z] coordinates of the intersection points between the snow surface and the marker poles. The symbol IDOT in the legend of Figures 34 through 37 identifies the profiles obtained from the Total station survey which are then compared with direct measurement measurements along the IDOT marker poles. However, the total station survey method is tedious and time consuming. This is the reason why we searched for better solutions of performing the survey at the field site (e.g., GPS survey discussed next).

2.2.5. Real-time kinematic survey

Figure 30. RTK survey conducted along the marker poles line.

A global positioning system (GPS) based real-time kinematic (RTK) survey was conducted at the start of the first winter season to obtain the bare ground profile in the direction defined by the marker poles installed at each of the three fence designs tested in the field. This first RTK survey provided the coordinates [x,y,z] of the contact points between the marker poles and the bare ground (Figure 28). The bare ground profiles at the three locations where marker poles were present were quite close. Thus, when comparing the data (snow deposition), the represented bare ground profile corresponds to the mean of the bare ground profiles determined at the three locations. During both winters, RTK surveys were conducted after the end of each significant snow event at the three locations to obtain the coordinates [x,y,z] of the intersection points between the marker poles and the top of the snow deposit (Figure 30). This protocol ensured that the cameras did not move under the actions of strong winds during storms. Equally important, the position and height of each marker pole were known such that the height of the snow blanket at the pole location could be

obtained from analysis of the images. This provided an easy way to verify the results of the RTK surveys.

2.2.6. LSPIV- Digimap

DigiMap is an in-house developed software by our group. The data obtained using DigiMap was also used to determine the snow profiles behind the snow fences. This is a technique which consists of measuring continuously the snow profiles rather than using coordinates at only a certain number of points like in the methods previously discussed (e.g., Tape measurements, Total station). In this method, the aim is to survey the marker poles set at the monitoring site for mapping the snow deposition and to acquire the information needed to conduct the ortho-rectification using the Digital Mapping Software (DigiMap). The main data collected is a mapping of the deformed surface obtained by deploying the Mobile Large-Scale PIV truck (MLSPIV) and then processing the images using the Digital Mapping software developed at IIHR. Photo views of the MLSPIV truck, the LSPIV components and the deployment of the LSPIV camera above the truck at the field site are shown in Figure 31.
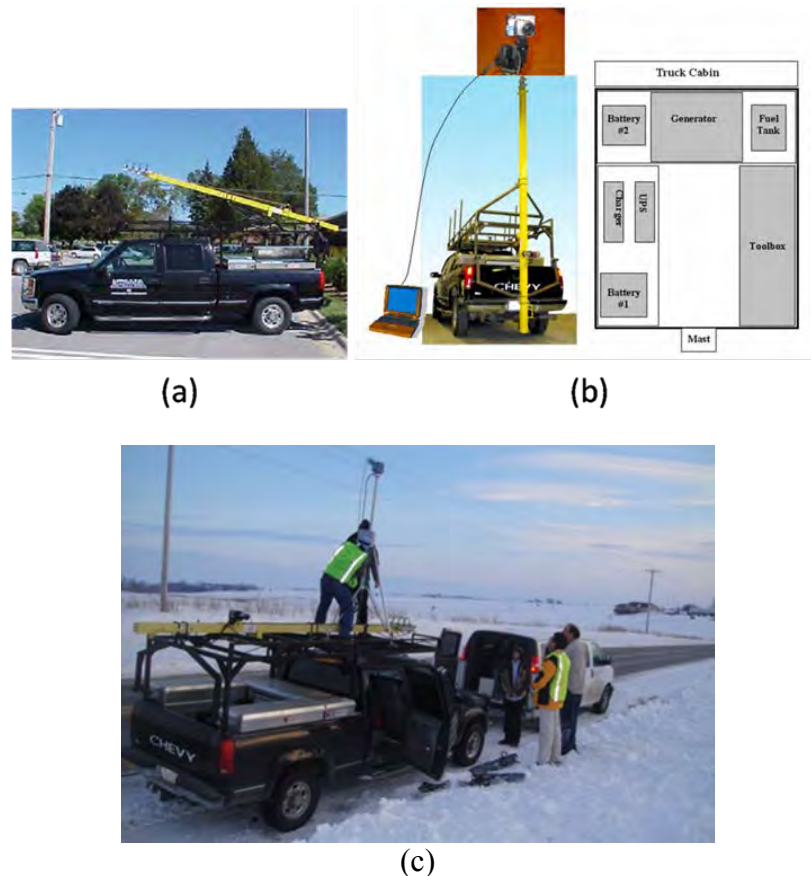

(a) (b)

(c)

Figure 31. Mobile LSPIV unit: a) LSPIV truck; b) LSPIV components; c) Photo performed at the field site displaying camera installment above the LSPIV truck.

Images were taken after major snow events at the site. At the study site, a series of images were taken using multiple framings from the MLSPIV truck, as shown in Figure 32a. Each framing should follow some rules of thumb such as: to include 3 to 5 poles, each image should cover at

least 300 pixels, as required by the DigiMap procedure. The acquired images were then stitched into a panoramic view using DigiMap. The survey tool (total station or GPS) was used to get the coordinates [X,Y,Z] of the poles and saved as text files for use with the Digital Mapping software. The images in Figure 32 were ortho-rectified (Figure 32.b) using as raw information the photographs in Figure 32a. Preliminary test results for an event occurring during the first winter are shown in Figures 33, 34 and 35 for fences A1, A2 and A3, respectively. Similar information is shown for another snow event during the first winter in Figures 37, 38 and 39 for fence A1, A2 and A3, respectively. Figures 36 and 40 compare the Digimap results with the Total station and direct tape measurements only at the IDOT marker poles present at site during the first and second events, respectively. The results by the three methods are comparable with each other though the near fence area could not mapped using DigiMap. The snow profiles can be quantitatively delineated with DigiMap but this was found to be tedious and time consuming for the purpose of volume calculation. Similar to the other methods discussed, this is a method that requires to visit the site and to spend a considerable amount of time in the field for performing measurements at the end of a snow event.

(a)

(b)

Figure 32. An example of LSPIV processing: a) Assembled raw images; b) ortho-rectified (geometrical transformation) images.
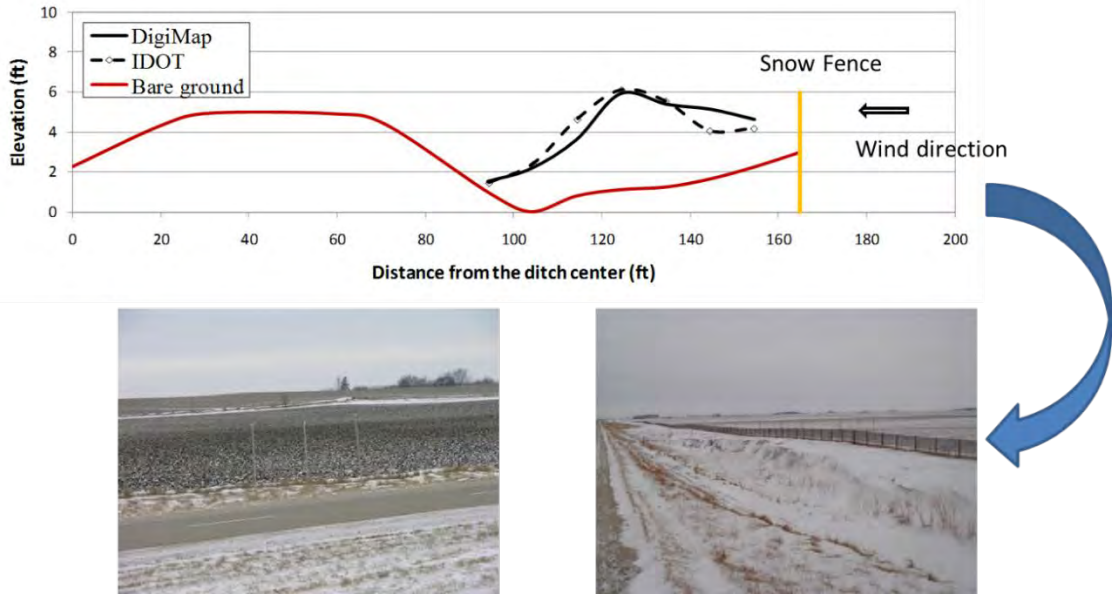
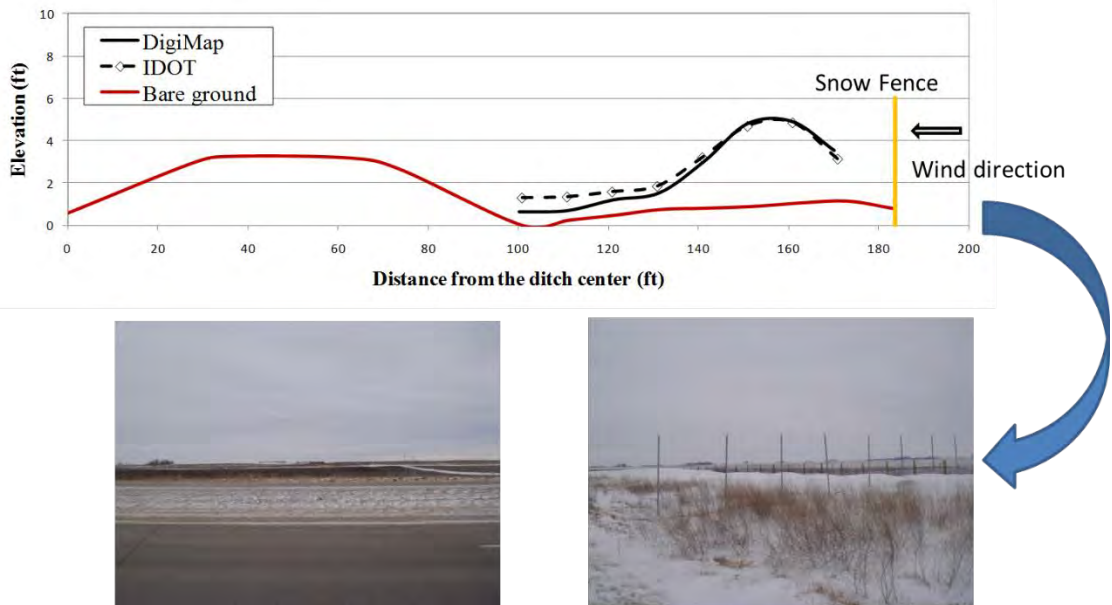Figure 33. Snow deposition profiles (A1 fence, December 16, 2010).

Figure 34. Snow deposition profiles (A2 fence, December 16, 2010).
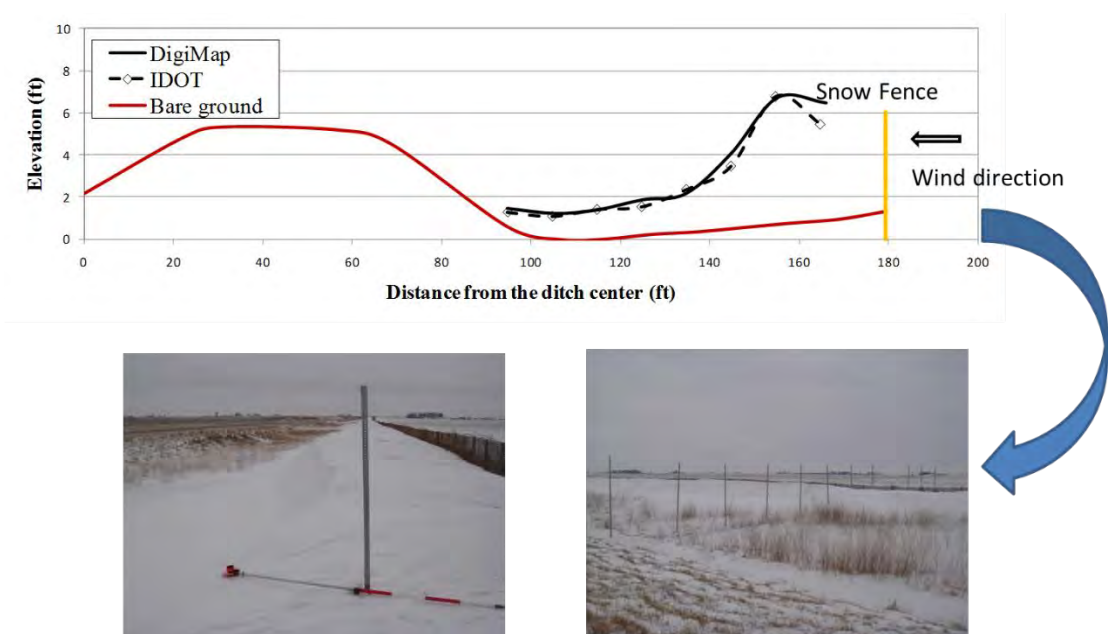
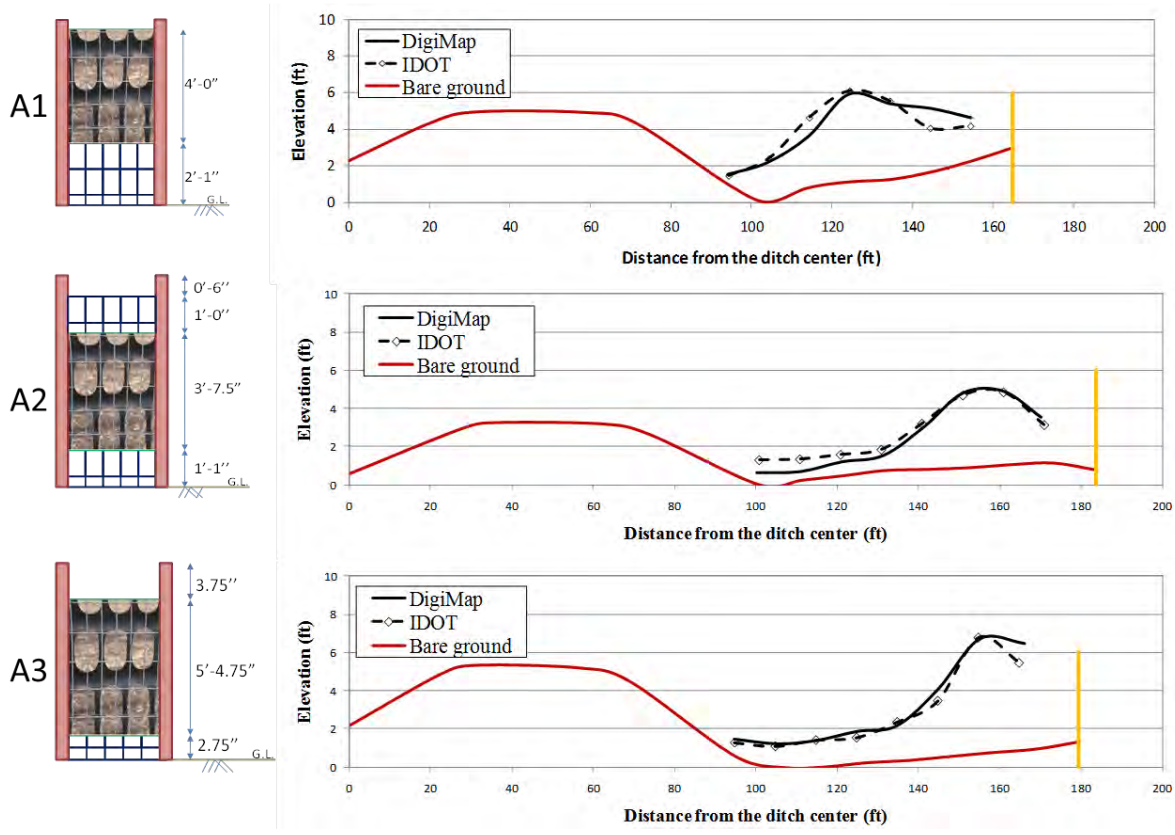Figure 35. Snow deposition profiles (A3 fence, December 16, 2010).

Figure 36. Comparison of snow deposition profiles be the three surveying methods (December 16, 2010).
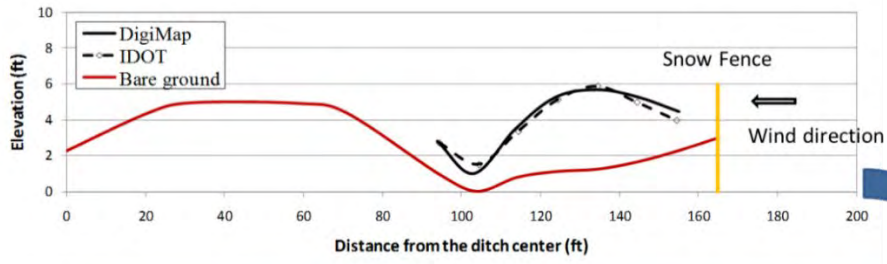
Figure 37. Snow deposition profiles (A1 fence, January 20, 2011).
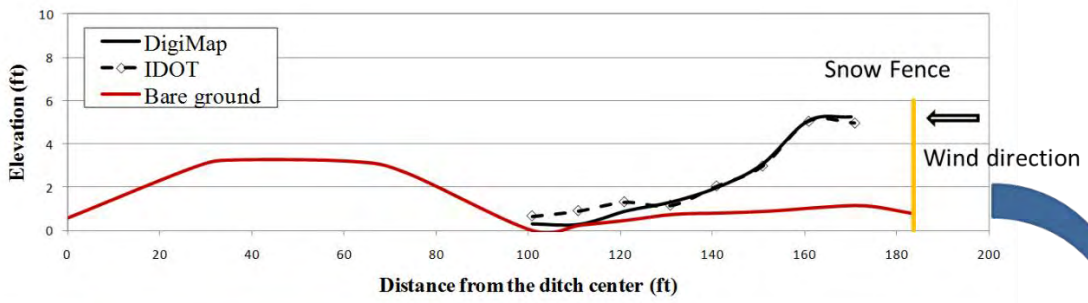

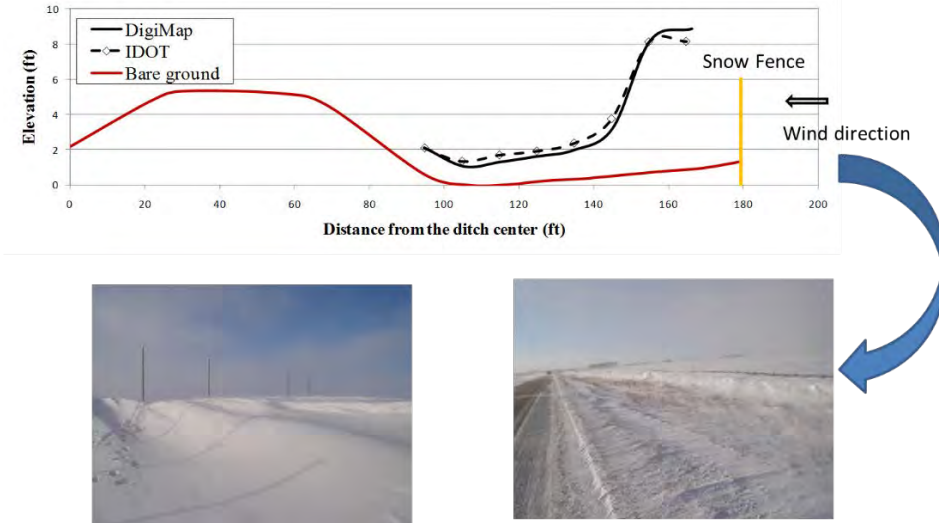Figure 38. Snow deposition profiles (A2 fence, January 20, 2011).

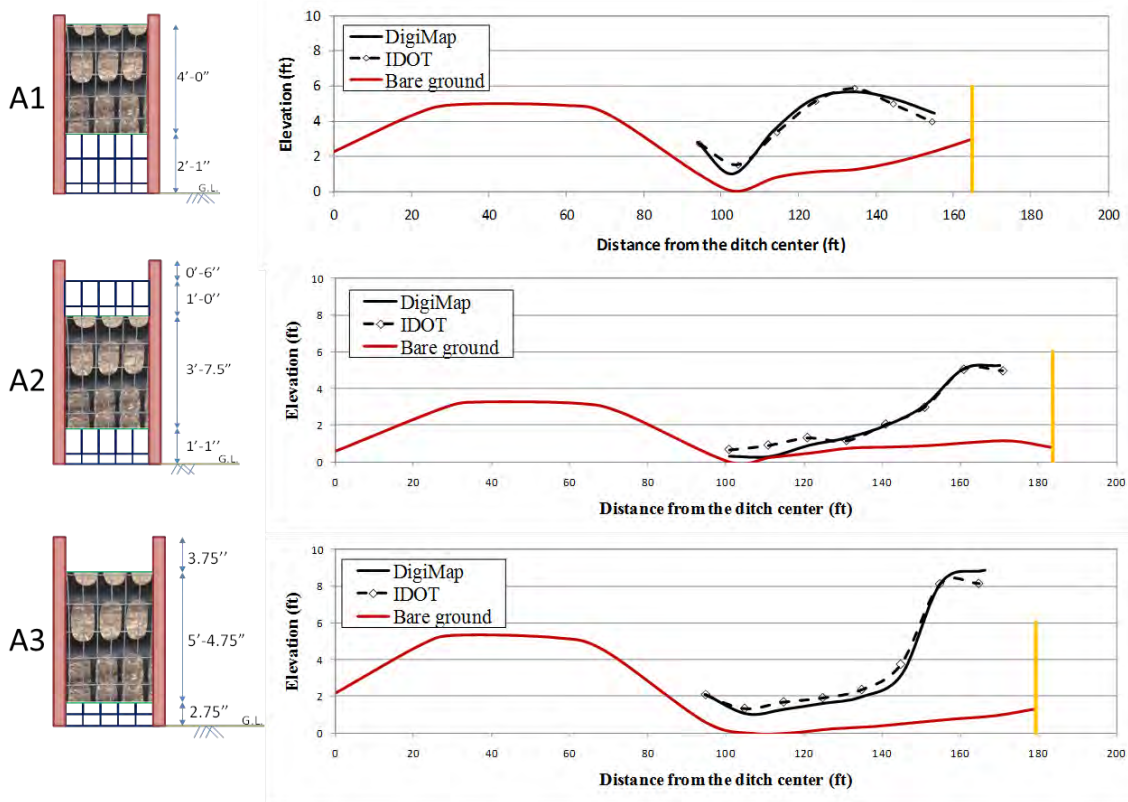Figure 39. Snow deposition profiles (A3 fence, January 20, 2011).


Figure 40. Comparison of snow deposition profiles by the three surveying methods (January 20, 2011).

2.2.7. Photogrammetry based surveying

2.2.7.1. CRP Components and Processing Steps

In this section we describe only the salient features of the processing steps for CRP measurements. More details about the technique's general principles and methodologies can be found in (Luhman et al., 2011). Specifics for aerial and terrestrial photogrammetry can be found in (Matthews, 2008) and (Schenk, 2005), respectively. The implementation of CRP consist three components: camera calibration, field survey and digital photogrammetric analysis. To generate 3D terrain model, the photogrammetric software requires four inputs: images of photographed area, camera interior orientation, camera exterior orientation, and geographic information of ground control points (GCP). The photogrammetric processing for obtaining the results in the present paper was conducted with Leica Photogrammetry Suite Project Manager (LPS Project Manager) which is a component of ERDAS EMAGINE software (LPS, 2009). LPS Project Manager has the ability to extract 3D terrain information from an image pair.

The CRP raw images are typically taken at some distance from the volume that needs to be evaluated and in most of the cases using a large angle between the camera optical axis and the vertical passing through the volume. This results in a large geometric distortion of the imaged volume. To correct geometric distortion, the camera interior orientation is required as illustrated in Figure 41a (LPS, 2009). This orientation is obtained using camera optical characteristics (e.g., focal length, principal offset and radial distortion) and a complementary calibration. The camera exterior orientation and Ground Control Points (GPC) locations are determined using specific measurements at the site (see Figure 41b). Exterior orientation includes the position and angular orientation of cameras with respect to the targeted measurement area. This information is subsequently used to establish spatial relationship between different images with overlapping areas. GCPs are specified by the operator and can be materialized by small stakes or temporary markers positioned sturdy on the ground in the vicinity and on the volume to be surveyed. GCPs need to be surveyed using alternative topographic tools. Their actual coordinates need to be associated with the image coordinates through a manual operation. LPS software requires at least three GCPs for each set of images.
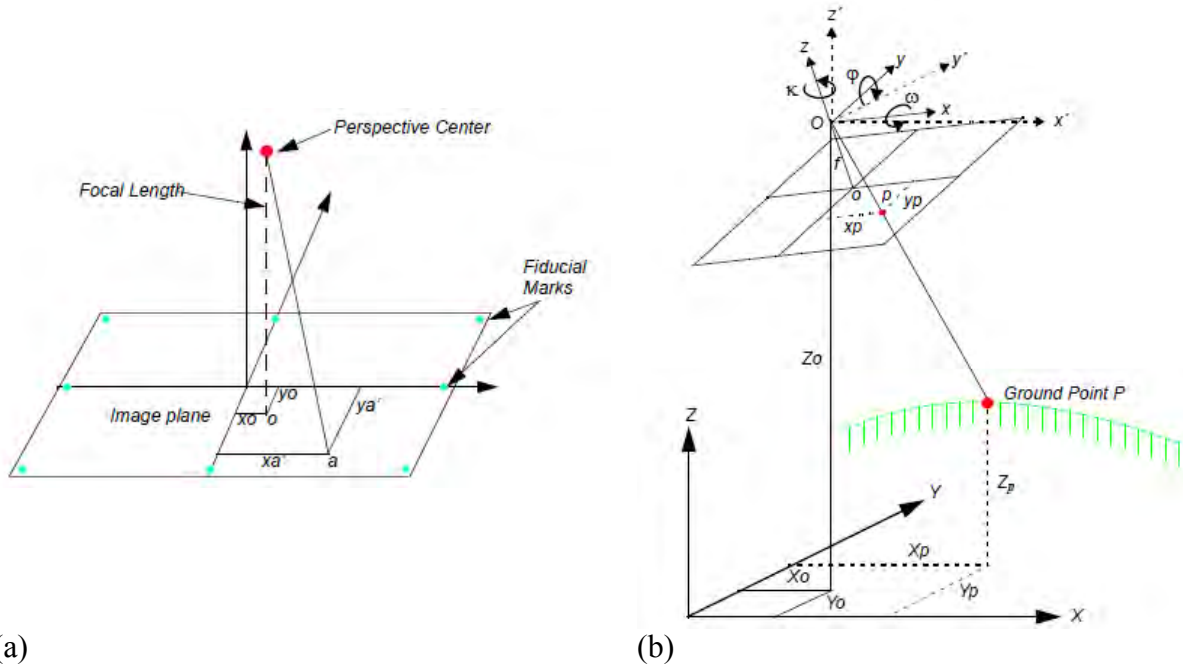
(a)   (b)

Figure 41. Interior and exterior orientation information: a) internal geometry (e.g., focal length, fiducial marks, lens distortion etc.); b) elements of exterior orientation (e.g., camera-to-image angles, ground control point position etc.). Source: LPS (2009), pages 31 and 35.

One of the initial steps of the digital photogrammetric process is the sub-pixel stereo matching (Matthews, 2008). As the resolution and quality of digital photography have improved significantly in past decades, sophisticated photogrammetric software (e.g., LPS Project Manager and Photo modeler) was developed to automate the execute sub-pixel matching between similar graphic patterns in image pairs captured with different cameras. These common points within overlapping areas of multiple photographs are automatically distinguished by the software and identified as tie points, i.e., points of high probability to represent the same location over the surface of the volume to be mapped (Figure 42). The computer-generated tie points are used in conjunction with the available GCPs to scale in physical coordinates the volume to be evaluated quantitatively as a geometric object.
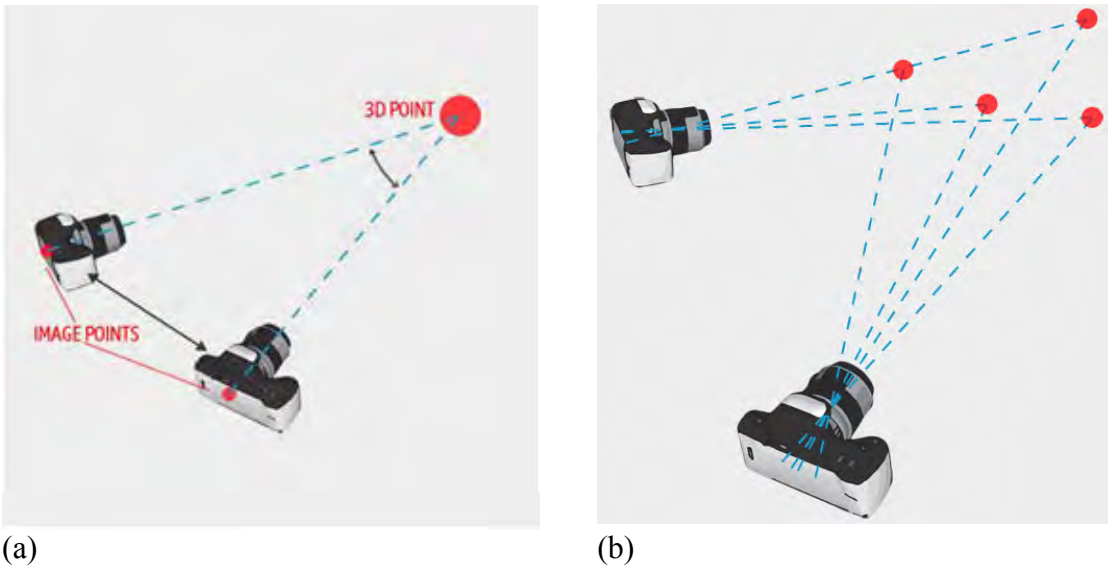
(a)   (b)

Figure 42. a) A pair of cameras focusing toward a 3D object; b) common points distinguished by each camera images (Source: http://www.photomodeler.com/products/how-it-works.html).

Subsequently, the coordinates of tie points are calculated using digital triangulation based on the survey of the geo-spatial location of the GCPs. Triangulation is a type of geographic interpolation that assigns calculated coordinates in unmeasured areas (areas between the known GCPs). Once the accuracy of tie points coordinates is observed, automatic terrain extraction tool (special feature in-build in ERDAS EMAGINE software) is used to provide a cloud of points of known coordinates (couple of thousands) covering the volume to be reconstructed. The procedure to obtain the cloud of points is visualized in Figure 43 using actual images from the case study used for illustration in the present paper. This figure also illustrates the major steps involved in the CRP process performed with the ERDAS IMAGINE software. The coordinates of the cloud of points obtained from the software as the output data were plotted using Tecplot software package (Tecplot 360, 2011) to quantitatively visualize the volume.
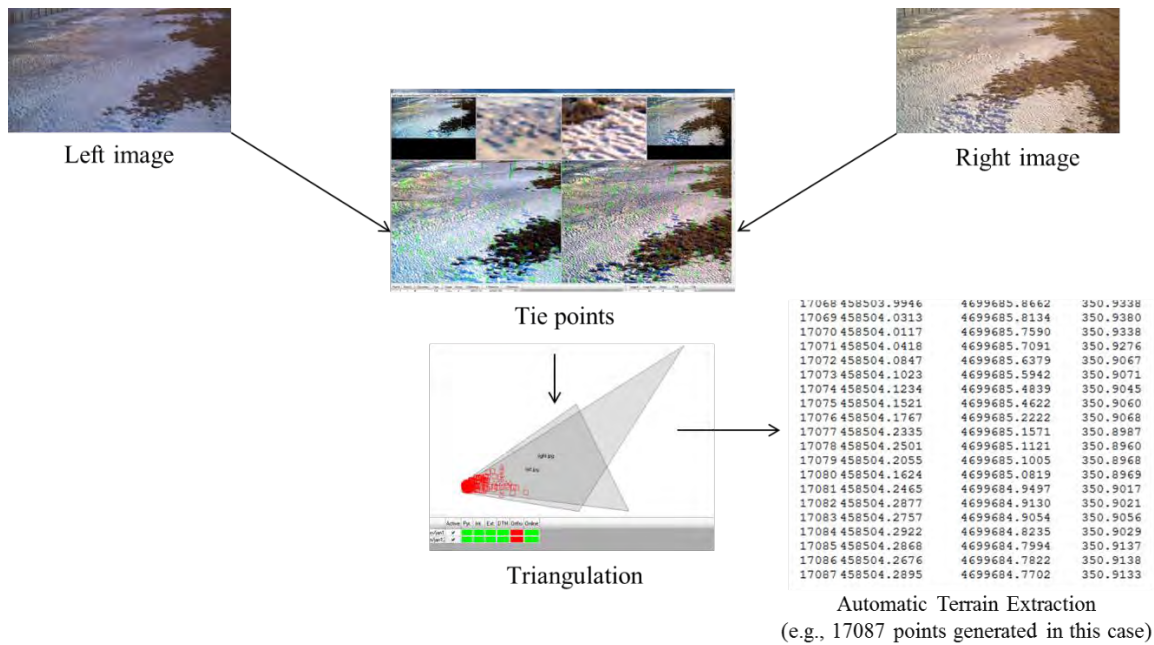
Figure 43. CRP process performed in the ERDAS IMAGINE software.

2.2.7.2. CRP survey site

The field measurements presented in this study based on the CRP method were taken at a fenced portion of Highway 20 near Williams (Figure 44). The site is exposed to about 5 months of winter conditions (from late-November 15 to early April) with an average snowfall of about 13 cm and an average dominant wind speed of 50 km/h blowing perpendicular to the fence direction. Presented herein are only estimates of the snow volume obtained based on CRP surveys.
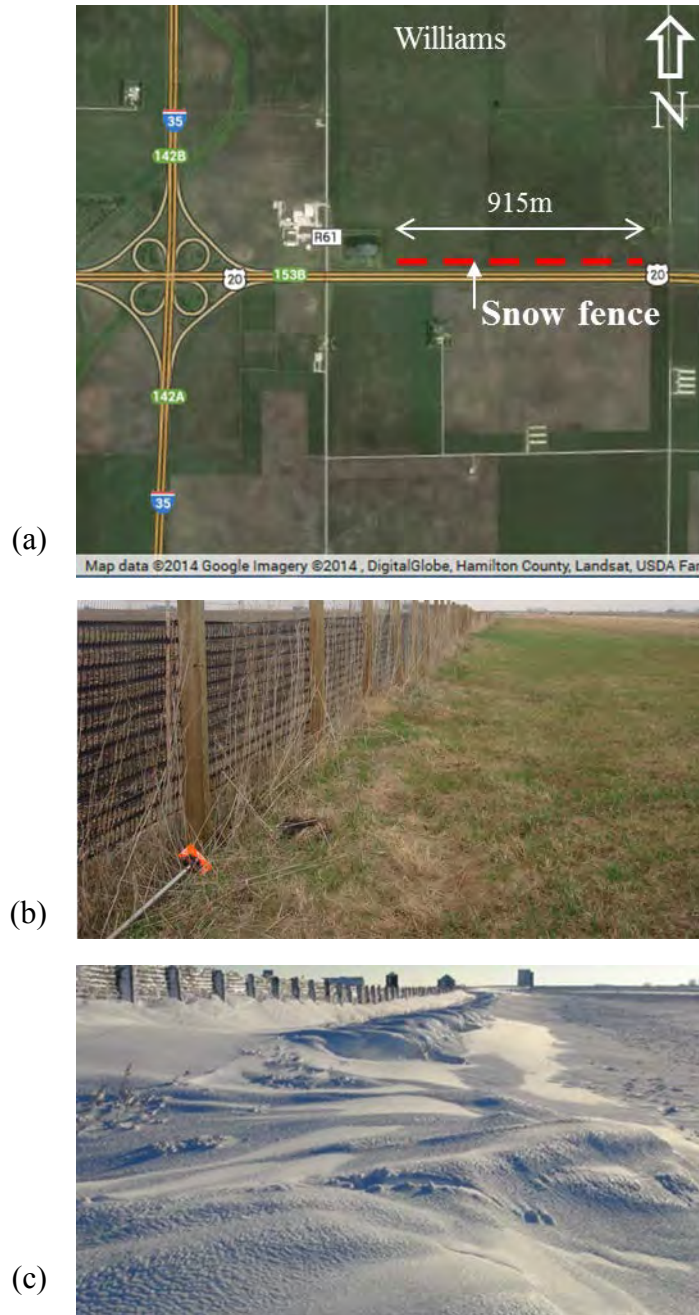
Figure 44. CRP survey site located on Highway 20, Williams, Iowa, U.S.: a) site location on Google map; b) photo of the bare-ground site (November 2012); c) snow retained by the snow fence (December, 2012).

2.2.7.3. Experimental arrangement for the synoptic measurements and real time monitoring

Three types of cameras, as displayed in Figure 45, were tested for the CRP measurements. After evaluating each of them, we decided that the i65 GAME Spy camera is the best option. Images for CRP were acquired with a commercially-available Moultrie i65 GAME Spy camera fit with a cell-

phone based transmission unit (www.moultriegamemanagement.com). This camera, characterized by 8mm focal length, 5mp native resolution sensor, and 2.2μm x 2.2μm pixel size, can continuously capture photo frames or video segments up to the point of filling the camera memory card (32 GB in our case). The off-the-shelf camera was installed in a weatherized plastic case (see Figure 46a). Embedded in the case were also a Global Positioning System (GPS) sensor, a backup battery, and solar panel connected to the battery. The customized system containing all the above-described components resulted in a stand-alone, self-powered observational node with real-time data transmission capabilities. The raw images for CRP were provided by a pair of such web-cameras set to record images every hour. Sample images acquired with the pair of cameras set of a pole illustrated in Figure 46b. An ancillary Moultrie Game Management System supported by the web-camera producer allowed accessing the acquired images in near-real time (see Figure 46c). The camera web-platform also allows to remotely control the camera operation parameters such as the sampling frequency for the recording. Images were often received with some delay depending on weather and communication conditions at the site. Besides of acquiring images for the CRP analysis, which was the primary role of the system, it was also useful in alerting the team on the proper timing to get out to the site for simultaneous measurements with the other instruments.

In addition to the continuous recordings with the dual-camera system, the snow deposits were mapped in situ using synoptic measurements over the CRP imaged area using alternative survey instruments during and after the major storms. There were three alternative measurement approaches used for this purpose. First, a set of marker poles were installed at the observation site using the spatial arrangement sketched in Figure 47a. The points of contact between the marker poles and the bare ground were surveyed before the winter season for providing reference surface for volume calculations. During the synoptic measurements the depth of snow at each marker pole was determined by directly measuring the distance from the snow surface to the tip of the poles with a measuring tape. The marker poles also provided fixed GCPs for supporting the CRP process during the whole extent of the video recordings. The second, and most often used as an alternative survey measurement approach, was a GPS based real-time kinematic (RTK) survey conducted as illustrated in Figure 47c. The major components of RTK survey equipment are shown in Figure 47d. The RTK synoptic surveys included all marker poles as well as at additional points (see Figure 47b) in the imaged area before, during, and after the storm events. The third snow-volume survey method consisted in measurements with total station (Topcon GTS 235 Total Station).

GaugeCam (M7-RC550WS)	I65 GameSpy	SONY (IPEAL SNC-RZ25N)
• Resolution: 932 X 1317 • Focal length: 8mm or 12mm • Self-powered • Wireless communication module wireless • Weather proofed • SD Card • Remote control Assessment: Camera still in development revealed numerous problems in setting and operation	• Resolution: 6 MP (2484 x 2136) • Focal length: 35 mm • Embedded GPS • Temperature measurement • Self powered • Wireless communication module • Remote control (limited) control16GB SD card Assessment: OK	• Resolution • Focal length: • Temperature measurement • Need power supply • Wireless communication module LAN • Remote control (positioning & image acquisition) • SD Card Assessment: The need for power and dimensions preclude its usage

Figure 45. Instrument acquisition: the three types of cameras tested in the study
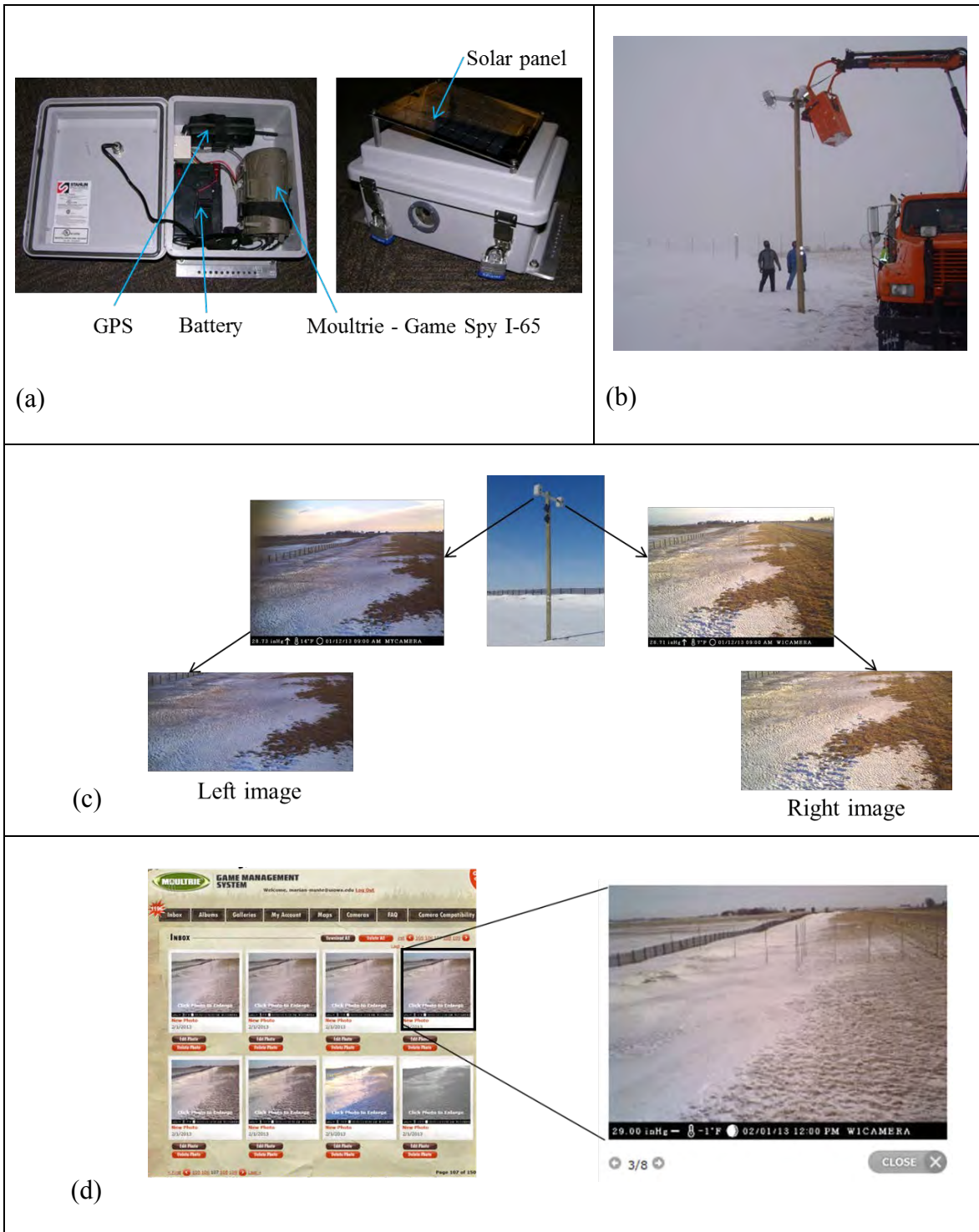
Figure 46. The image-based system used for site monitoring: a) the camera assembly; b) camera installation in the pole; c) raw images acquired for CRP processing; d) the real-time, web-based image-management platform.
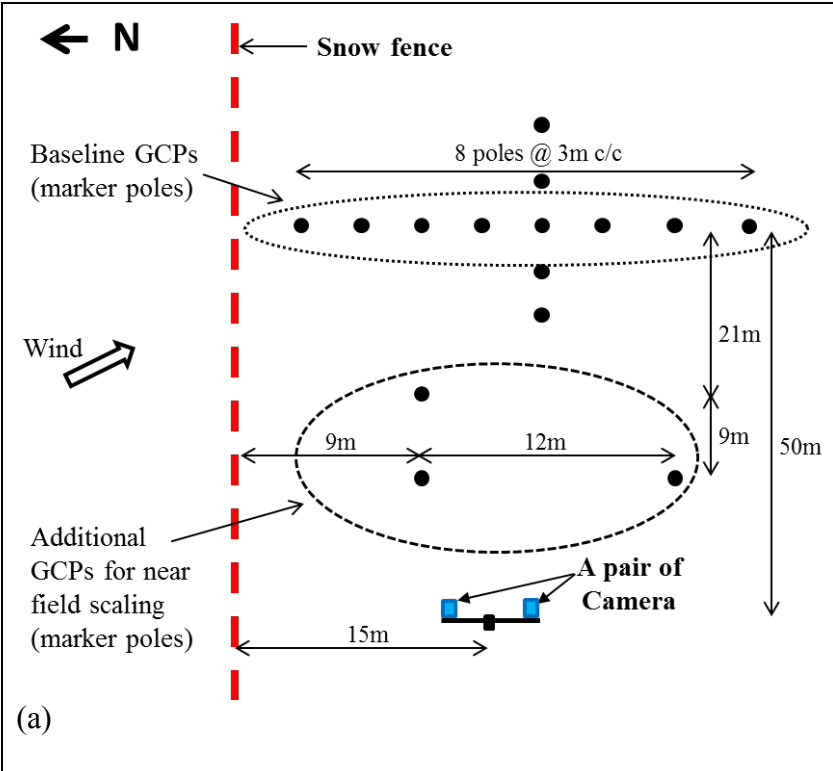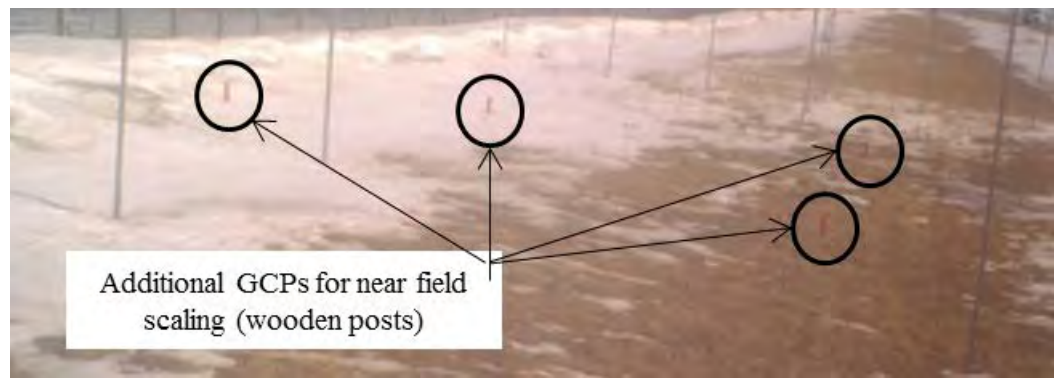
Figure 47. Experimental arrangement of the site and RTK field survey: a) schematic diagram with 15 in-situ markers poles as GCPs (not at scale); b) a photograph displaying 4 wooden posts as additional GCPs; c) a close up view of the GPS surveying at the GCPs and the RTK survey equipment components.

2.2.7.4. Operational Issues

The operation of the Moultrie cameras and their data communication system were analyzed during the first winter using the protocol described in Figure 48. None of the camera units displayed problems related to power (solar panels), image blockage (due to diminished visibility during storms) and mechanical failure (loose internal or external connections). However, not all of them were operated throughout the whole season. Therefore, further investigation of operational issues of Moultrie cameras was conducted during the summer (see Figure 49) at the IIHR laboratory and also at a field site located at Hwy 1 in Iowa City, IA. The analysis performed for each camera is tabulated in Figure 50. It was found that the SD card needed to be formatted before using despite the fact that it has 12GB memory capacity. The summer test was helpful to fix the operational issues of the cameras and to make sure that all the cameras worked properly. If one camera was found to have problems, it was replaced with a new camera.

Camera operation failures (Moultrie; Game Spy I-65)						
Hwy 20 (Plastic snow fence)				I-35 (Living snow fence)		
Site B1	Site B2	Site B3		Site 4	Site 5	
Cam 1	Cam 2	Cam 3L	Cam 3R (with comm.)	Cam 4	Cam 5L	Cam 5R (with comm.)
Stopped* March 27, 2013	Stopped April 4, 2013	Stopped January 18, 2013	Stopped April 12, 2013	• Stopped December 27, 2012 • Auto started February 12, 2013 • Stopped again in the same day	Stopped March 24, 2013	Stopped January 2, 2013

Figure 48. Protocol to determine camera operation reliability (2012-2013 winter season).

(a)

(b)

Figure 49. Summer test: a) monitoring at the IIHR laboratory; b) deployment and monitoring at a culvert site in Willow Creek, Hwy 1, Iowa City, IA.

Camera operation failures (Moultrie; Game Spy I-65)						
Cam 1	Cam 2	Cam 3L	Cam 3R	Cam 4	Cam 5L	Cam 5R
*Memory card full Stopped March 27, 2013 (2500 pics) **(Now working)**	*Memory card full Stopped April 4, 2013 (2500 pics) **(Now working)**	Camera Problem (under investigation)	*Memory card full Stopped April 12, 2013 (2700 pics) **(Now working)**	Battery problem **(Now working with a new battery)**	*Memory card full Stopped March 24, 2013 (2280 pics) **(Now working)**	Battery problem (Camera OK)

Figure 50. Results of summer test: Camera operation and communication.

After fixing the issue with the formatting of the SD card, all of the cameras worked well throughout the second winter season except for a pair of cameras installed for the first time upwind of the fence. The strong wind in the region situated upwind of the fence, where two cameras were installed, is one reason why the battery could not run for a longer period compared to the other cameras installed downwind of the fence (see Figure 51). One needs to further investigate this issue before installing cameras upwind of the fence.

Camera operation failures (Moultrie; Game Spy I-65)							
Hwy 20 (Plastic snow fence)						I-35 (Living snow fence)	
Site B1	Site B2	Site B3 South (Downwind of fence)		Site B3 North (Upwind of fence)		Site B4 East	Site B4 West
Cam 1 (w/o comm.)	Cam 2 (w/o comm.)	Cam 3L (with comm.)	Cam 3R (with comm.)	Cam 4L (with comm.)	Cam 4R (with comm.)	Cam 5 (with comm.)	Cam 6 (with comm.)
Nov 1 – Jan 29 Feb 20 – May 2	Nov 1 – May 2	Nov 1 – Feb 25 Apr 25 – May 2	Nov 1 – May 2	Nov 27 – Feb 27	Nov 27 – Jan 26	Jan 29 – May 2	Nov 1 – May 2

Figure 51. Camera operation reliability (2013-2014 winter season).

### 2.2.7.5. Implementation of Experimental Protocols

Synoptic measurements were carried out after each significant snow storm. During these measurements, the snow accumulations at the baseline points and additional points associated with the marker poles (see Figure 47a) were thoroughly surveyed. In order to secure good sets of GCPs for CRP, additional points dispersed over the imaged area (Figure 47b) were surveyed with the various techniques available. The number of GCPs for the CRP measurements was continuously increased during the successive trips until the accuracy of the snow volume estimation with CRP

was attained within a prescribed level. A total of 19 points over the image area of 50m x 30m were deemed necessary to accurately map snow deposits at this site using the CRP. During the synoptic measurements still photos were captured with the dual camera systems to support the CRP sensitivity analysis and estimation of accuracy through comparisons of various alternative measurement approaches. The site visits for synoptic measurements were also occasions for checking the status of each camera assembly component and to download the recorded images for subsequent processing.

The CRP analysis was conducted on the images acquired in the field after retrieving them from the cameras (typically once every three weeks). Given that the main role of this experimental study was to estimate volumes of snow captured by the snow fence over the whole duration of a snow storm, the synoptic measurements acquired immediately before and after a storm event suffice. Taking advantage of the continuous imaging at the site attempts were made to test the capabilities of CRP image acquisition system to provide snow accumulation rates as the storms develop. Such a capability enables additional insights in the details and phases of the snow accumulation process. Figure 52a illustrates a sequence of continuous and synoptic measurements acquired during a storm at the experimental site. In this figure, Protocol 1 (P1) approach denotes synoptic measurements where the CRP snow volume measurements were paired with in-situ alternative surveys and consideration of additional GCPs in the imaged area. Protocol 2 (P2) approach entails CRP measurements obtained from continuous monitoring and use of GCP coordinates provided only by the fixed marker poles deployed at the site, therefore not requiring visit of the site.

Figure 52b illustrates the sample comparison between the elevations of the snow accumulations across a section as obtained with the P1 and P2 measurement approaches. The agreement between the two profiles confirms the reliability of the CRP to map snow deposits using either of the acquisition protocols. There are only few successful storm event tracking documented with both P1 and P2 protocols because the trips were cost- and effort-extensive. Moreover, the snow storms at this site have a typical duration of 1-2 days therefore involving night time periods (see Figure 52c). During night time, the web-cameras equipped as described above do not produce images. This limitation can be overcome for smaller storms if an alternative installation with illumination during night time can be added to the imaging assembly. For large storms the system, however, even the additional lighting is not sufficient to produce sufficient illumination at the area of interest if only conventional lighting means are considered.
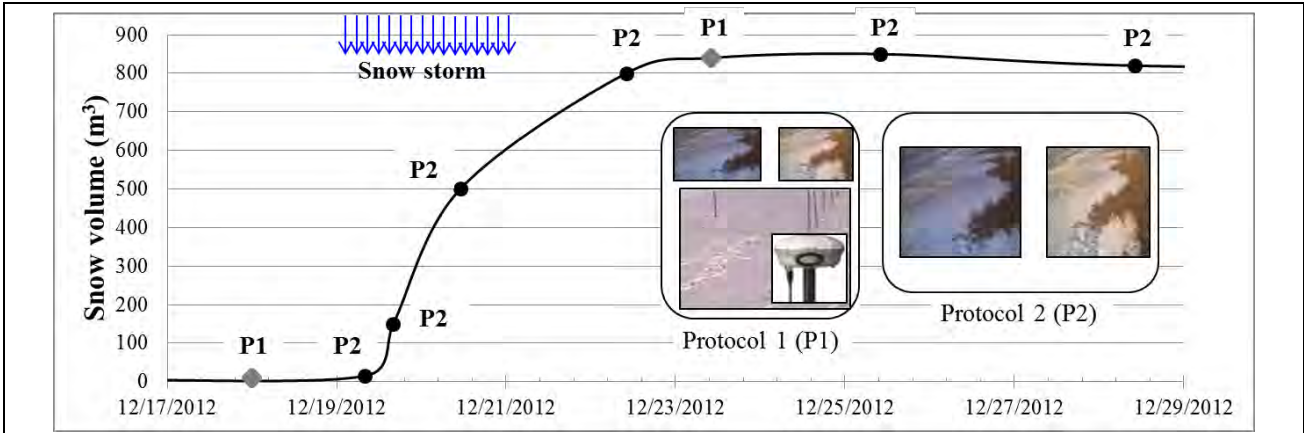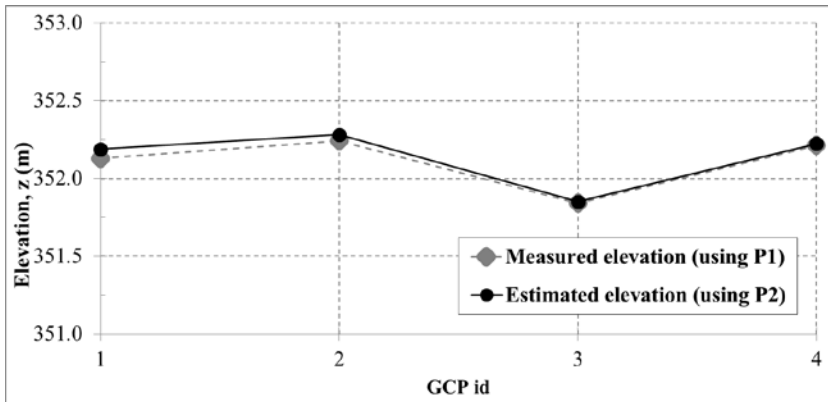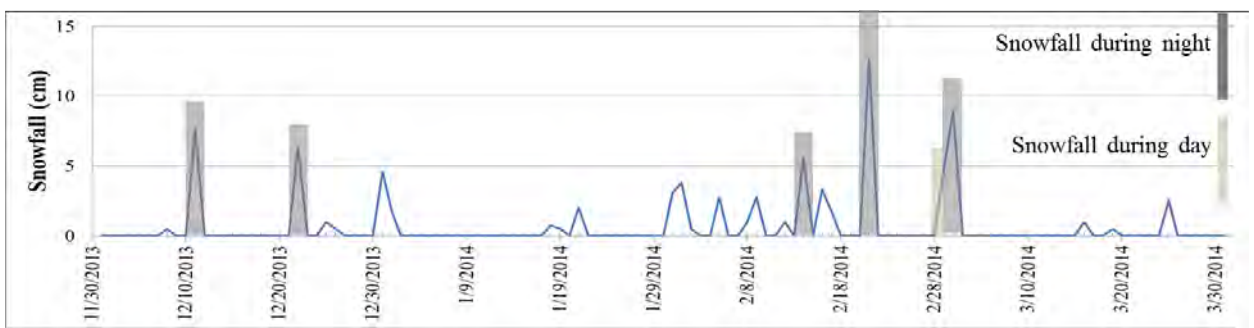
Figure 52. Tracking snow storm events:
a) combination of continuous and synoptic measurements during the duration of a storm;
b) comparison of a cross section through the snow deposit using protocols P1 and P2;
c) snow-storm timing and duration at the study site (winter season 2014). Data source: www.mesonet.agron.iastate.edu.

2.2.7.6. Sensitivity Analysis

The critical review of the case studies conducted with CRP as main surveying tool provided numerous practical hints for technique's implementation. Given the non-sophisticated, off-the-shelf equipment used in the study, the authors tested the CRP implementation at various sites that

resemble case studies previously reported in the literature. One of this surveys was conducted to a culvert site and is presented here for illustration purposes (see Figure 53). This site was surveyed with equipment and operating conditions similar to those used to investigate the snow fence deposits, i.e., framing size (of about 1500 m^2) and 15 GCPs. Intermediate processing parameters and final results of the culvert survey are indicated in Figure 53.
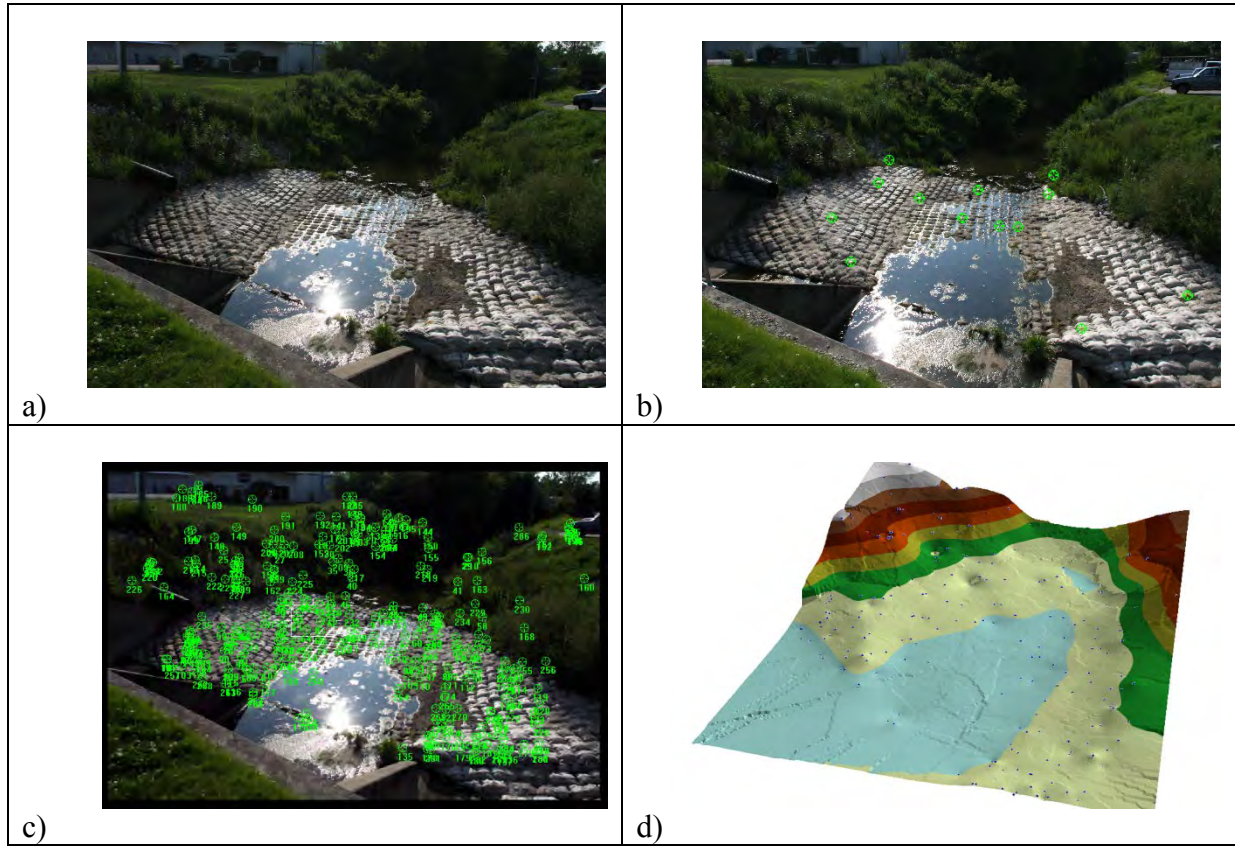

Figure 53. CRP implementation at a culvert site: a) left image; b) right image including the GCPs for survey; c) tie points created by the software; d) final results of the CRP survey.

The good results obtained for the survey of the culvert site confirmed that the CRP image acquisition and measurement protocols are adequate for the scope of this study. However, it was obvious that there are considerably differences between the texture-rich surroundings at the culvert site and the snow surface with the main being the lack of prominent color gradients or geometrical texture. These differences pose upfront challenges for CRP processing of the snow surface images requiring adequate attention during the technique implementation. Consequently, the authors further explored the sensitivity and accuracy of the CRP to various parameters involved in snow surface mapping through additional tests described below.

2.2.7.6.1. Ground control points density and distribution

A number of 12 GCPs were initially used for our application to train the CRP software in the processing stage. 8 of these initial GCPs are distributed along a line crossing the snow deposits created by the now fence, as illustrated in Figure 47a. This GCP arrangement was suggested by the mostly two-dimensional shape of the snow deposits at fences. The GCP axis perpendicular to

the fence direction is labeled as baseline GCPs. Processing successively the same image pairs by removing gradually GCPs from 12 to 8 and eventually to 4 led (as expected) to a loss in the accuracy of the snow surface reconstruction. The results of this tests are illustrated in Figure 54. The snow surface is better resolved along the GCP line and deteriorates rapidly with in the area without GCPs. The total range of the resolved free-surface elevation (absolute values) is also changing with the number of GCPs used in processing.
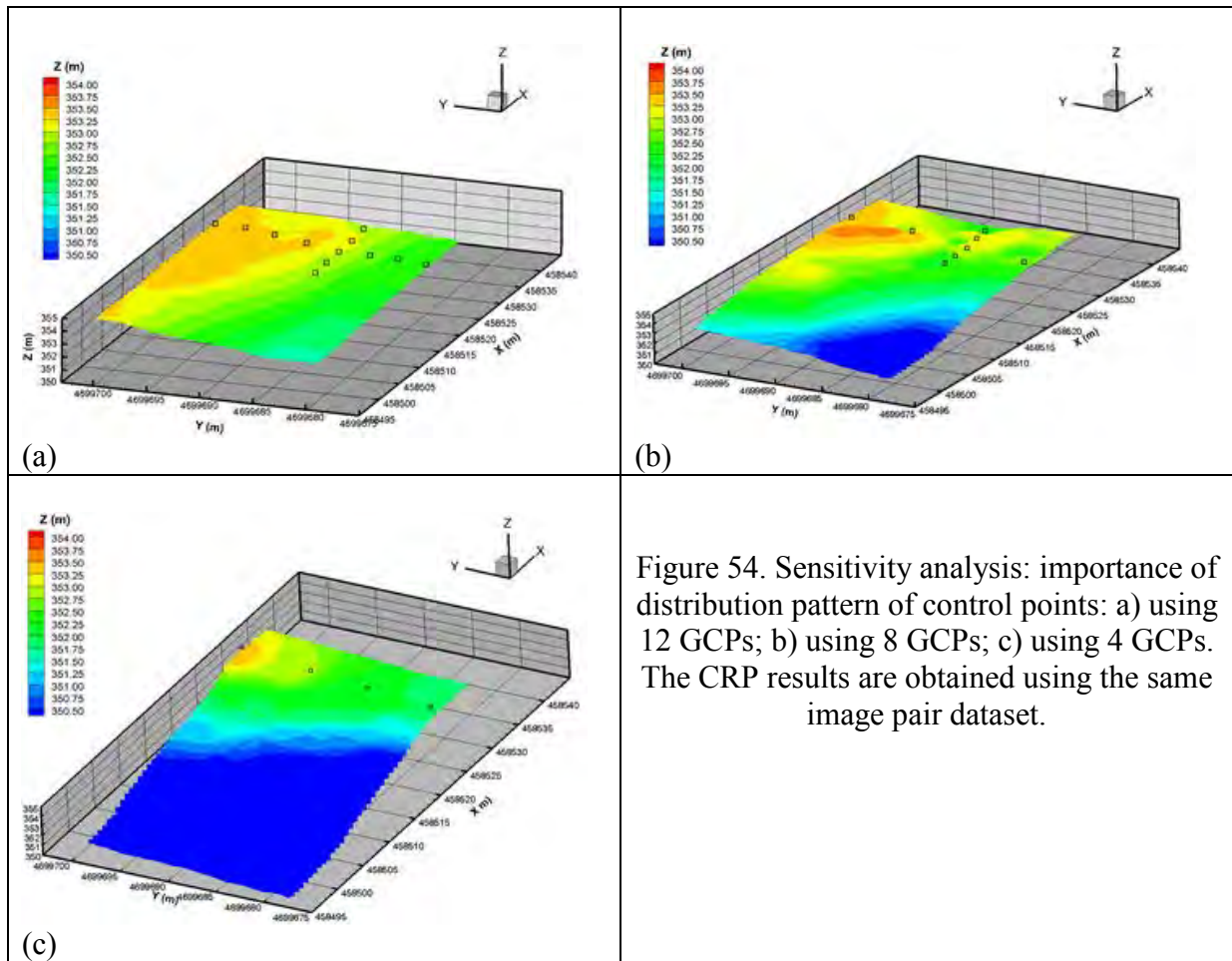

(a)

(b)

(c)

Figure 54. Sensitivity analysis: importance of distribution pattern of control points: a) using 12 GCPs; b) using 8 GCPs; c) using 4 GCPs. The CRP results are obtained using the same image pair dataset.

Based on these preliminary observations, the number of points was subsequently increased to 19. More importantly, the additional points were mostly placed in the near field area (labeled additional GCPs in Figures 47a and 47b). The CRP analysis with increased number of GCPs proved their efficacy by leading to a better reconstruction of the actual deformations of the snow free surface and an increase in the area with a well-defined topology compared with the results obtained with less GCPs. The assessment of the accuracy for the sensitivity tests reported herein is based on the comparison with the alternative measurements used in the synoptic measurements (see Table 1).
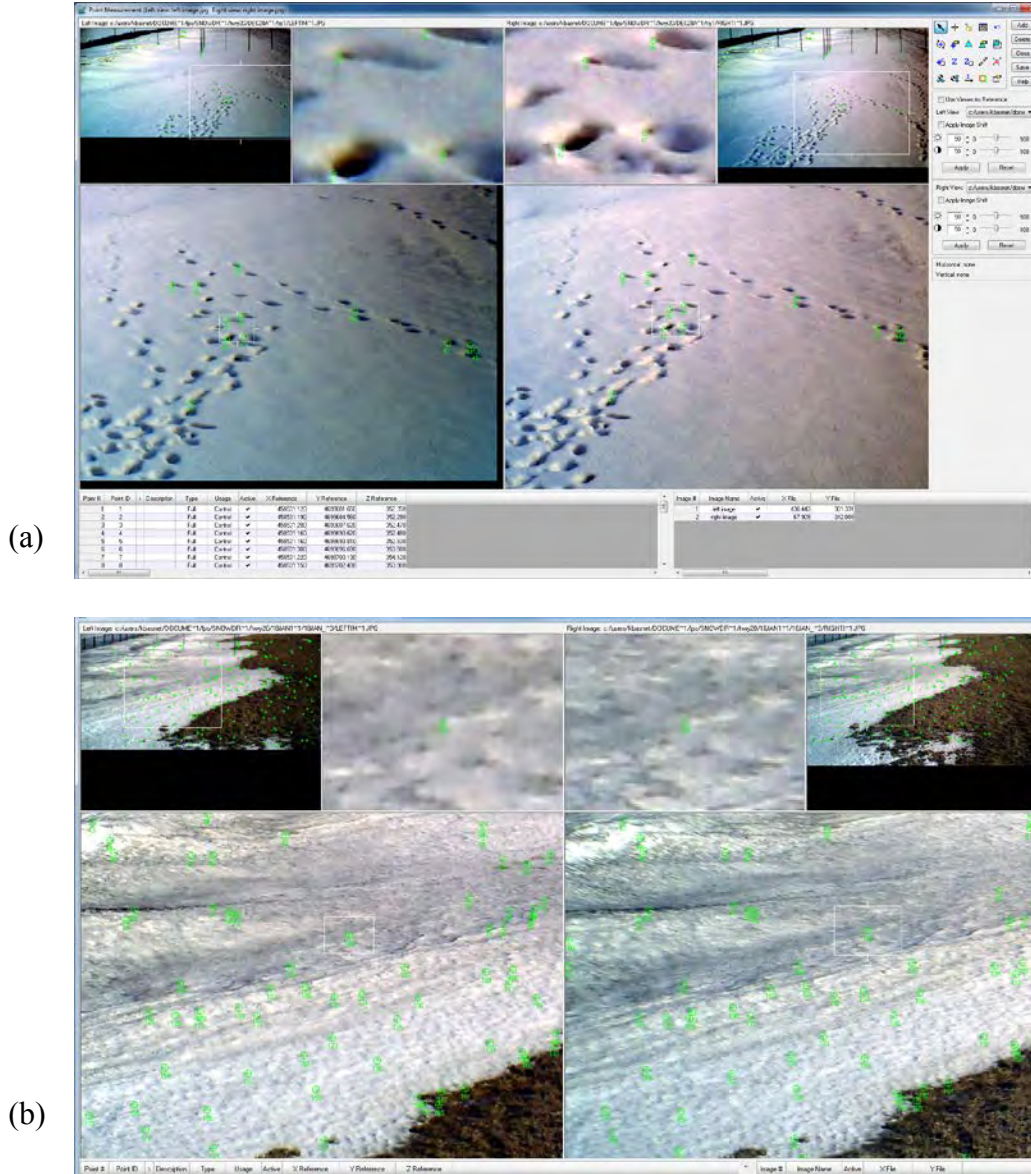
2.2.7.6.2. Surface texture

(a)

(b)

Figure 55. Texture effect on the tie point density (ERDAS screen shots): a) a limited number of tie points are generated on fresh created snow deposits; b) a sufficient number of tie points are generated on images after the snow packages through melting.

The surface of the fresh snow deposits is practically without apparent texture in the recorded images. Moreover, the smoothness of the shapes and the bright white color do not create many distinguishable features in the images. These image features are in stark contrast with surfaces used other CRP implementation cases reported in previous studies. Figure 55a clearly illustrates the connection between the lack of texture and the number of tie points identified by the software. It is obvious that the far field area does not practically contained features to trace the surface. In the near field, the footprint of the steps created by the crew working at the site have produced a multitude of recognizable features in both images. The software CRP software easily creates tie points over the footprints as shown at the bottom of Figure 55a.

The situation is somewhat improved for older snow coverage as shown in Figure 55b. Snow melting and transitions between bare and snow covered areas (as illustrated in this figure) will provide more distinguishable features on the surface to be mapped that in turn will facilitate the creation of tie points by the CRP software, as illustrated in Figure 55b. The examples provided above clearly illustrates difficulties in photogrammetric processing induced by the nature of the imaged area. For the same site, instrumentation, and image acquisition protocol the technique displays greatly different efficiency in reconstructing the topography of the surface. There are situations where the surface cannot be mapped at all because of the absence of tie points. In the later situations, the only solution for CRP mapping is the creation of artificial image features such as by spreading light materials over the fresh snow falls as described next.
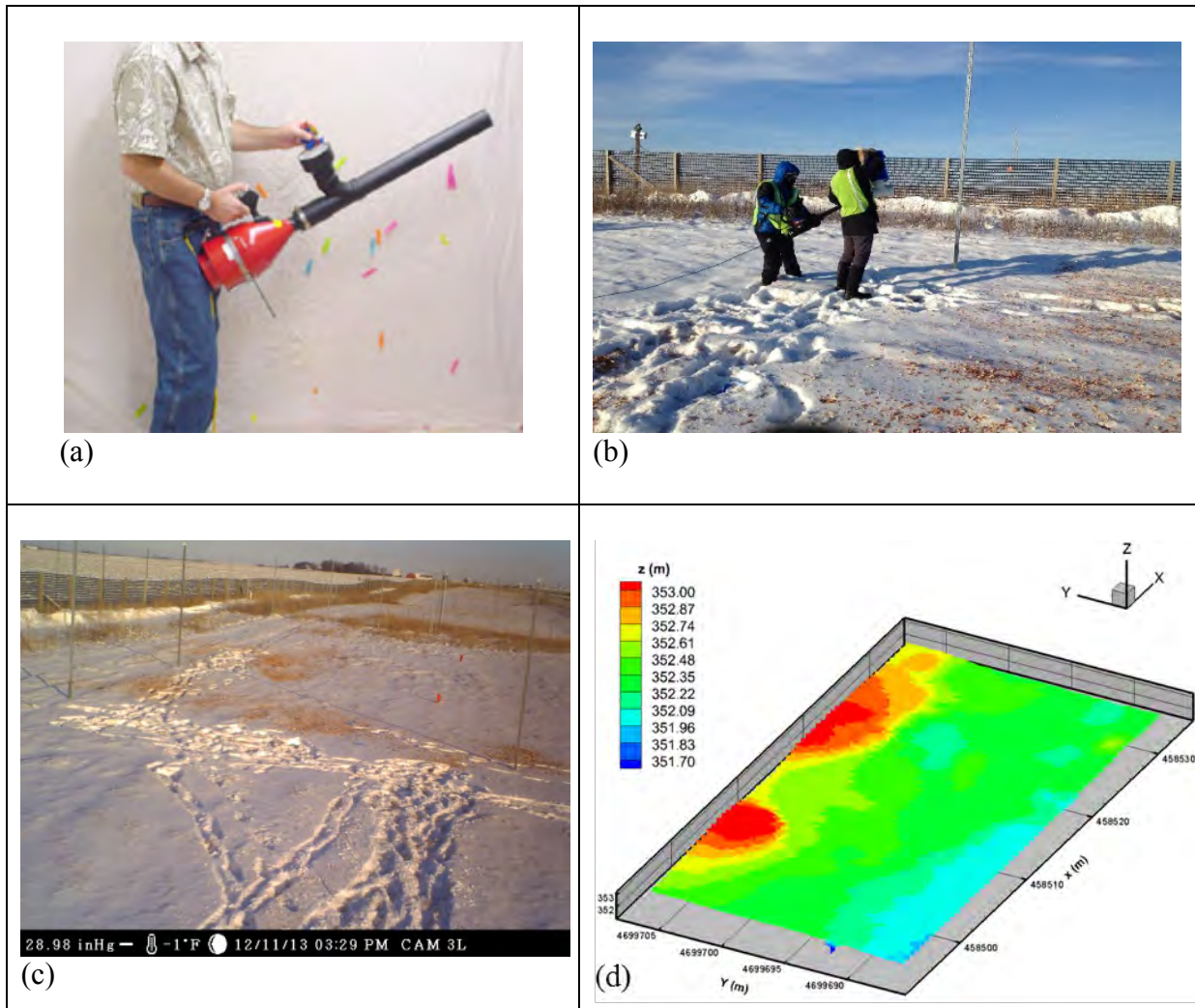

Figure 56. Improvement of the surface texture by addition of light materials spread over the snow volume surface: a) confetti volcano (http://www.aerotechnic.com); b) use of the cannon at the experimental site; c) snow free surface seeded with mulch and leaves; c) results of CRP processing using the seeded surfaces.

We also tested the benefits of the addition of artificial texture over the snow deposits using dried leaves and light wood chips spread at the survey location (see Figure 56). This material is non-intrusively distributed over the snow surface using specially designed particle blowing cannons that spread the material in an efficient way over the entire area of interest. The conventional use of these cannons is for shooting a continuous volume of confetti through air. They are built in various sizes, configurations, and operating modes. They can be deployed at any site using electric power produced by portable generators (http://www.aerotechnic.com).

2.2.7.6.3. CRP mapping accuracy

Although the CRP technology is a mature technique and has been widely used, its accuracy documented with alternative instrumentation is seldom available (Yakar and Yilmaz, 2008). The CRP 3D reconstruction is based on measured quantities (e.g., the distance from the camera to object, angle between the camera providing images), equipment characteristics (e.g. optical parameters for the imaging camera) and statistical and image processing methods (e.g., pattern recognition, spatial interpolation). Assessment of the sources of errors from all the technique components is a complex task and it is beyond the scope of the present paper. An end-to-end direct comparison of the CRP results with measurements acquired with alternative instruments are reported here as a surrogate for the uncertainty analysis.

The comparison is made between the snow profiles obtained with CRP and RTK at selected locations of the mapped area. Five arbitrary points are used for training the photogrammetry processing, as illustrated in Figure 57a. The elevations from CRP and RTK surveys for those 5 points are plotted in Figure 57b. The numerical values of the x- and y-coordinates (CRP results) with respect to measured values (RTK data) are determined based on the mapped length (50 m) and width (30m) respectively. The total elevation difference (highest to lowest) between the CRP and RTK for the entire mapped area is 2.02 m which is close to the total fence height (2m) used as reference. The percentage errors of the CRP results for the compared points are displayed in Table 2. The largest difference between the CRP and RTK mapped point in this profile is about 31 cm that is equivalent to 15.5%. These differences are collectively attributed to the poor resolution of the camera, the limited number of GCPs, and the difficulties to optimally recognize features in the images.
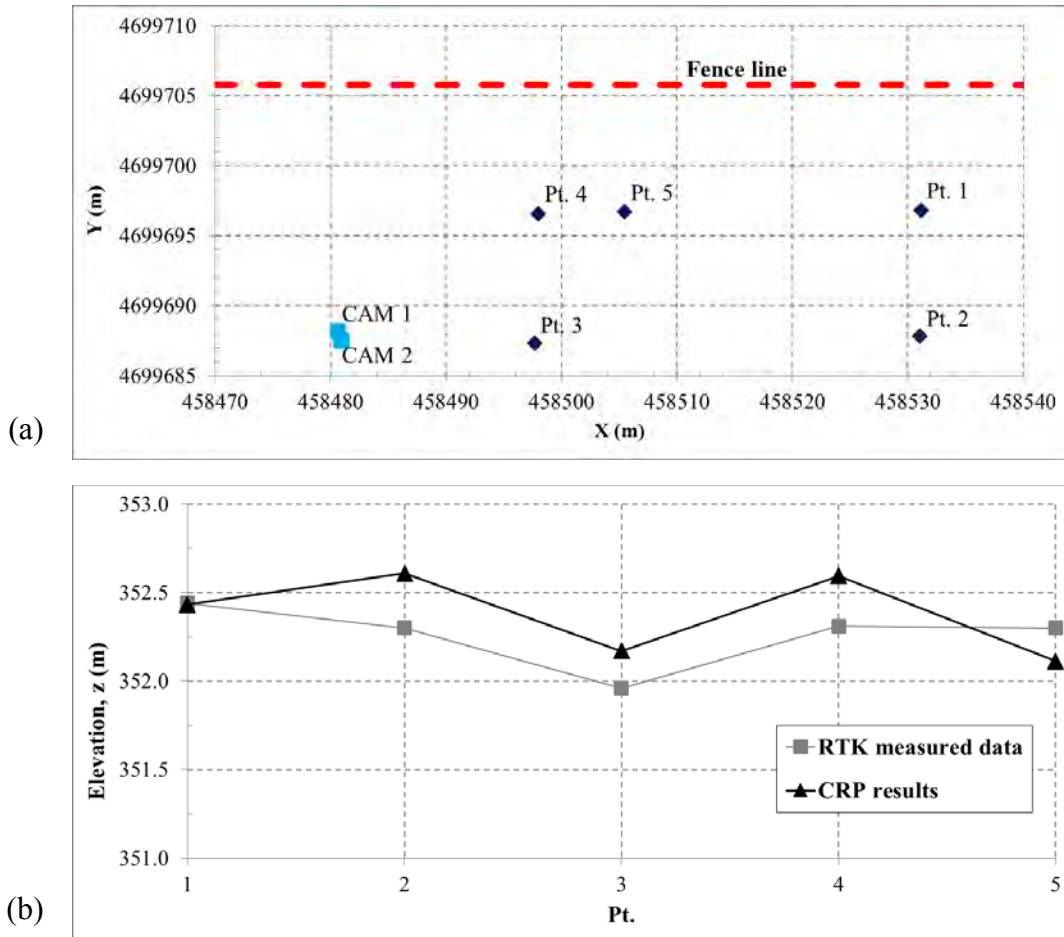
(a)

(b)

Figure 57. Comparison between computed CRP results and RTK measurements at the experimental site: a) location of arbitrarily selected five imaginary points; b) comparison between snow free surface profiles acquired with the two techniques.

Table 2. Evaluation of the accuracy of CRP results.

Pt.	$|\% error|$		
	X	Y	Z
1	0.14	0.03	0.4
2	2.12	0.78	15.5
3	0.9	0.23	10.6
4	0.76	0.75	14.2
5	0.57	0.1	9.3

3. USE OF A JOINT MODELING AND EXPERIMENTAL APPROACH TO DEVELOP A METHOD TO OPTIMIZE FENCE DESIGN

The new methodology to develop a method to optimize snow fence design is presented next. The methodology was specifically applied to lightweight plastic snow fences whose standard porosity is 50%. All experiments were conducted at the Williams site. The idea was to try to obtain a best design for fences with a lower porosity (30%) that, at least in principle, have a higher capacity to retain snow. The parameter that had to be optimized is the relative bottom gap of the fence, which is expected to be higher than the corresponding value for fences with a porosity of 50%.

As already mentioned, all three fence designs tested during the first winter at the Williams site had a fence porosity of 50%. One of them (A3) had a total height H 1.9 and a relative bottom gap G/H=0.08. This is the conventional design used by the IDOT for plastic snow fences. As the main goal of the present project is to study the performance of lower porosity fences with P=30% which need larger relative bottom gaps, it is interesting to first understand what is the effect of G/H on the amount of snow retained by the fence and on the shape of the snow deposit for fences with P=50%. As the fence porosity decreases, the potential for the snow deposit to advance toward the fence, fill the bottom gap and eventually touch the downwind side of the fence increases. Once that happens, the snow fence capacity to further reduce snow drift is negligible. To understand this effect, the relative bottom gap was increased to 0.2 for design A2 and 0.34 for design A1.

The other goal of the field testing conducted during the first year was to understand how the snow retaining capacity and performance of fences with P=50% changes with the relative bottom gap for a constant snow fence height h and for a constant total fence height, H. This is why the fence height was kept the same (h 1.25) for fence designs A1 and A2, while the total fence height was kept the same (H 1.9) for fence designs A1 and A3.

The snow deposition profiles after the most severe snow event recorded during the first winter are compared in Figure 58. As expected, fence design A3 performs the best in terms of the total volume of snow deposit per unit length (direction parallel to the road and fence) and the streamwise extent of the region of high snow deposition relative to the fence. Comparison of snow profiles for cases A1 and A3 shows that maintaining the same total fence height while increasing substantially the bottom gap greatly reduces snow deposition in the immediate vicinity of the fence and pushes the region of high snow deposition away from the fence. In fact, the relative bottom gap for design A1 is sufficiently high such that the snow deposit within the bottom gap is negligible. However, the total volume of snow deposited behind the fence is much smaller compared to that observed for design A3. Though part of the difference is due to the larger fence height (by 50%) of design A3, clearly the performance of design A1 is poorer than that of design A3.

If the fence height is kept constant (designs A1 and A2), results in Figure 58 show that the shape of the snow deposition profile changes qualitatively past a threshold value of G/H. The snow deposition profile for design A2 is qualitatively very similar to that observed for design A3, which is not the case for design A1. For fences with P=50%, design A1 has clearly a too large G/H. The ratio of the volume of snow deposit for designs A3 and A2 is about 2.5, which is significantly larger than the ratio of the fence height (1.5) for the two designs. This suggests that the relative bottom gap for design A2 (G/H=0.2) is too high. It is very likely the ratio will be closer if the fence

would have been built with the same height as for design A2, but with G/H close to the value used for design A3 (G/H=0.1).

Figure 59 compares the velocity magnitude distributions for designs A1, A2 and A3. The plot in Figure 59c contains a long and relatively thick region of reduced velocity magnitude downwind of the fence and close to the ground. The results for design A2 (Figure 59b) are qualitatively similar, though the streamwise extent of this region is significantly lower than that observed for design A3 and the average velocity magnitude within this region is somewhat higher. The strong horizontal momentum of the jet-like flow originating within the bottom gap region of design A1 is the main reason why no significant snow deposition is observed for design A1 close to the fence.
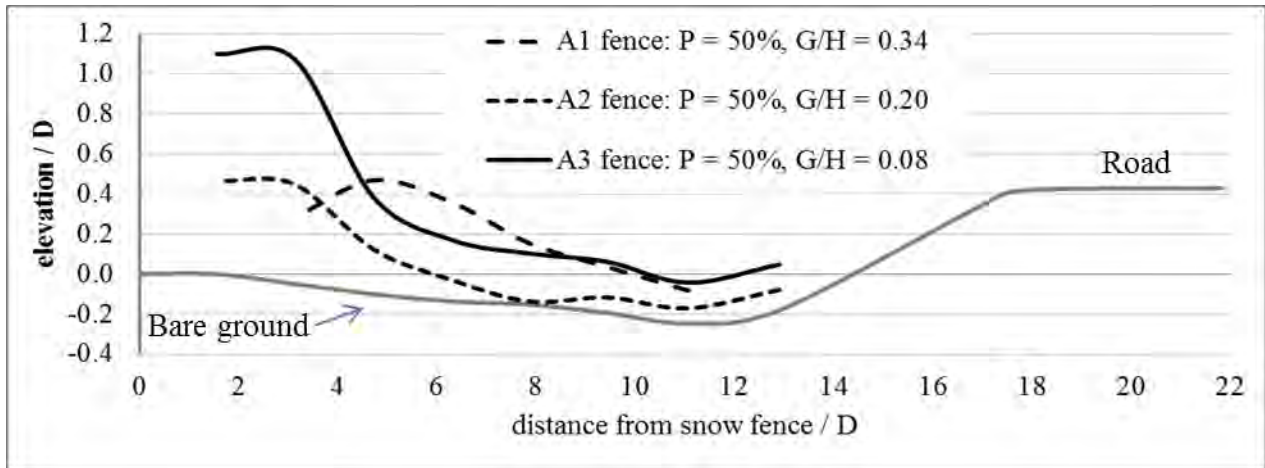

Figure 58. Snow deposition profiles behind the fence designs tested during the first winter (A1, A2, and A3). D (= 2m) is the length scale characterized by average fence height. The fence is located at distance from snow fence = 0D.
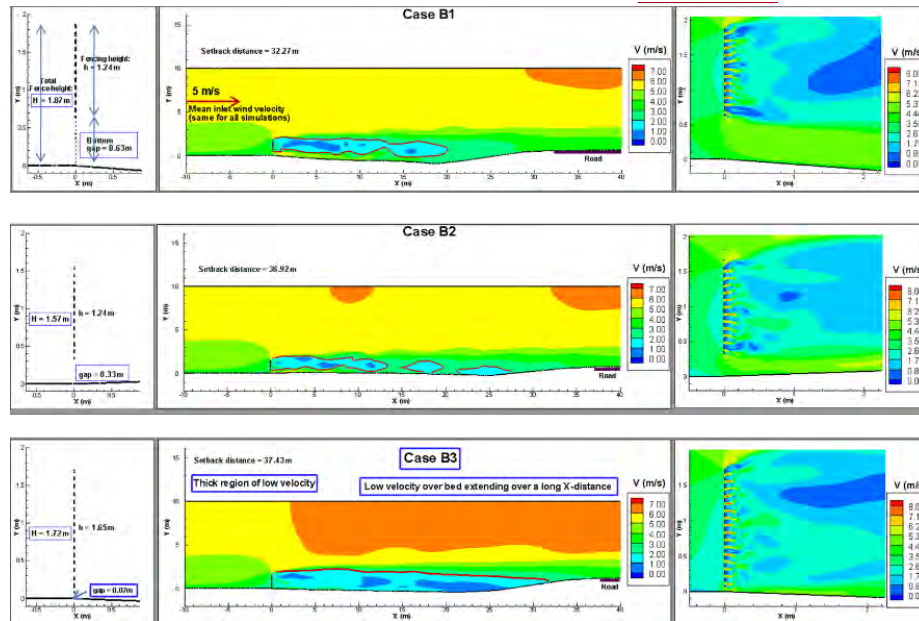
Figure 59. Distribution of velocity magnitude around and downstream of the fence designs (A1, A2 and A3 in Table 4) with a porosity of 50% tested during the first winter.

The next step was to try to come with other designs that would produce a relatively long and thick bottom layer of low velocity magnitude. The other idea was to relatively increase the bottom gap as the porosity was reduced. Before varying the porosity, several other designs denoted Case 1 to Case 5 in Table 4 with the same porosity but with different fence heights and relative bottom gaps were undertaken. The only fixed parameter was the distance between the fence and the road. Parameters in Cases 1 to 3 are, in fact, very similar to those in Case A1 to A3, respectively. Results in Figures 60 and 61 confirm that Case 3 is the optimum with respect to the criterion chosen to evaluate the performance of a given design; that is the formation of long thick bottom region of low velocity magnitude.

Table 3 also contains the other simulations performed with fences with a porosity which was different from 50% or for fences of different design (e.g., inclined fences) compared to the standard design used for fences with a porosity of 50% that were undertaken with respect to the base case (A3 also denoted B3) that was found to be the best design for fences with a porosity of 50%. Cases 6 to 10, 16, 17, 19, 20 and 21 correspond to standard vertical fences with a porosity of 30%. The main parameter varied was the relative height of the bottom gap. As results in Figures 62, 63, 66 and 68 show, the most promising design among these 5 cases corresponds to Case 7 that will be denoted B2 and to case 16 that will be denoted B1. This design was then tested in the field together with the best design for fences with a porosity of 50% denoted B3. Then a similar parametric study was undertaken for fences with a higher porosity of 70%. As shown by results in Figures 64 and 65 corresponding to Cases 11 to 15, the region of small velocity magnitude was situated at large distances away from the fence which suggests most of the snow deposition will occur at large distances from the fence. Or, especially for locations with narrow rights of way, the optimum design will retain most of the snow in the immediate vicinity of the snow fence. So, none of these designs were chosen to be tested in the field. Case 18 considered an inclined fence. The problem is that as a result of the fence inclination the region of low velocity magnitude got away from the bed at some locations. This idea was also abandoned. Finally, Cases 22 and 23 in Figure 69 show

that using 2 lower height fences instead of a larger height standard fence can also induce a relatively thick region of low velocity magnitude. The best design should have an increased relative bottom gap for the downstream fence (Case 23). However this idea was not pursued further because the main focus was on fences that can be placed in regions with narrow rights of way. Using 2 smaller fences requires a larger distance between the upstream fence and the road compared to the case when only one fence is used.

Table 3. Matrix of simulations.

| Fence	Porosity (%)	Total fence ht "H" (m)	Bottom gap (m)	Plastic fence ht. or Fencing ht. "h"(m)	Setback distance (m)	Remarks
A1		1.87	0.63	1.24	32.27	
A2		1.57	0.33		36.92	last year
A3		1.72	0.07	1.65	37.43	
1	50		0.56	1.42		
2		1.98	0.26	1.72		
3			0.15	1.83		B3: chosen from last year
4		1.5	0.26	1.24		
5		1.29	0.05			
6			0.61	1.63		
7		2.24	0.46	1.78		B2: Proposed
8	30		0.15	2.09	35.54	
9		1.8	0.26	1.24		
10		1.5	0.05			
11			0.56	1.24		
12		1.8	0.26	1.54		
13	70		0.05	1.75		
14		1.5	0.26	1.24		
15		1.3	0.06			
16	30		0.61	1.91		B1: Proposed
17		2.52	0.46	2.06	40	
18	50					Inclined fence
19			0.15	2.37		
20		1.8	0.2H = 0.36m	1.44	30	
21	30		0.2H = 0.2m	0.8		
22		1			20	2 fences @ 20m spacing
23			0.05m and 0.2m	0.95m and 0.8m		Different bottom gaps
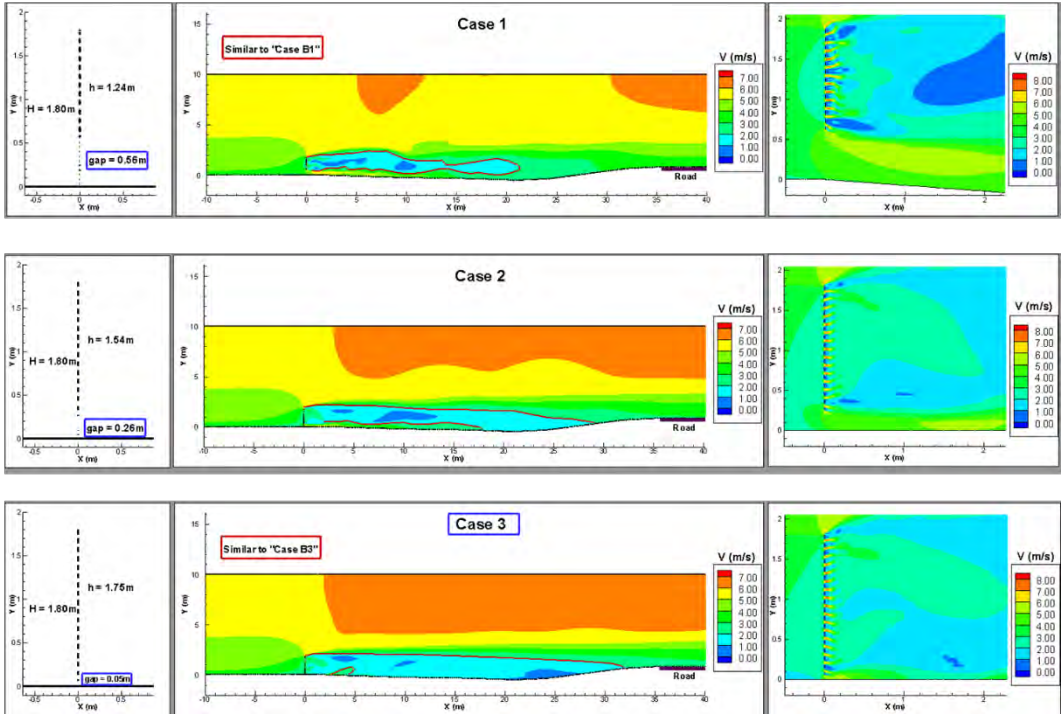
Figure 60. Distribution of velocity magnitude around and downstream of the fence designs with a porosity of 50%, setback distance of 35.5m.
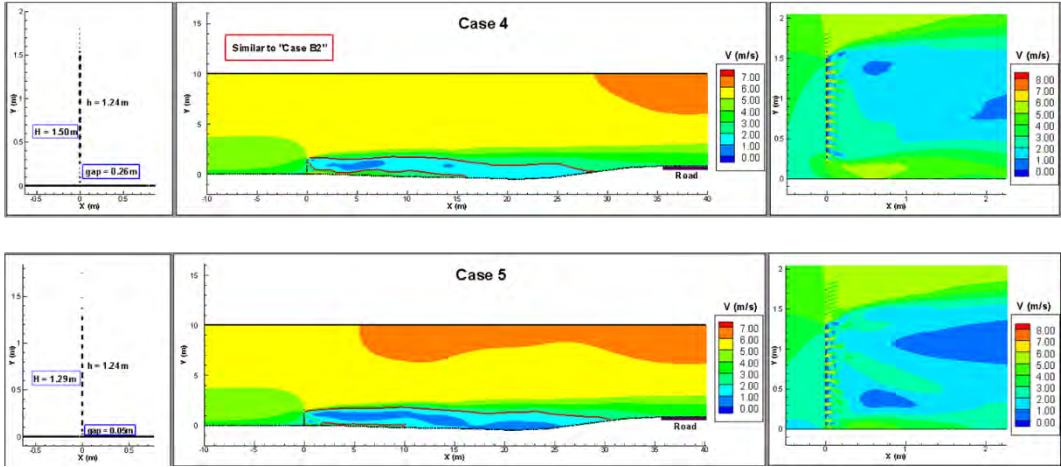

Figure 61. Distribution of velocity magnitude around and downstream of the fence designs with a porosity of 50%, setback distance of 35.5m.
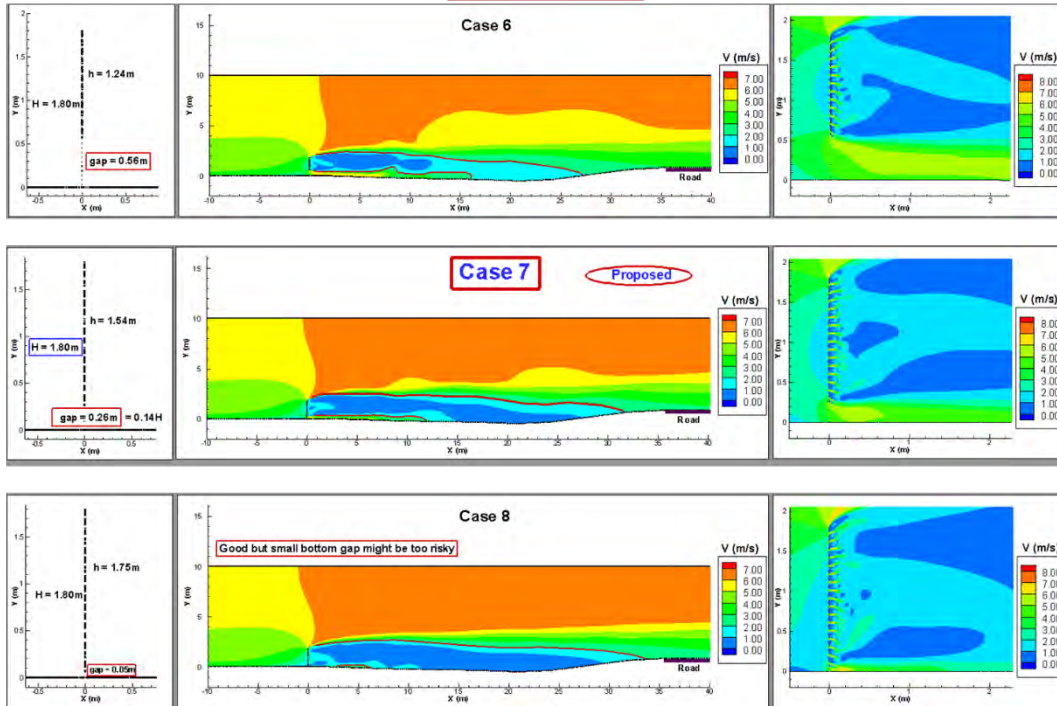
Figure 62. Distribution of velocity magnitude around and downstream of the fence designs with a porosity of 30%, setback distance of 35.5m.
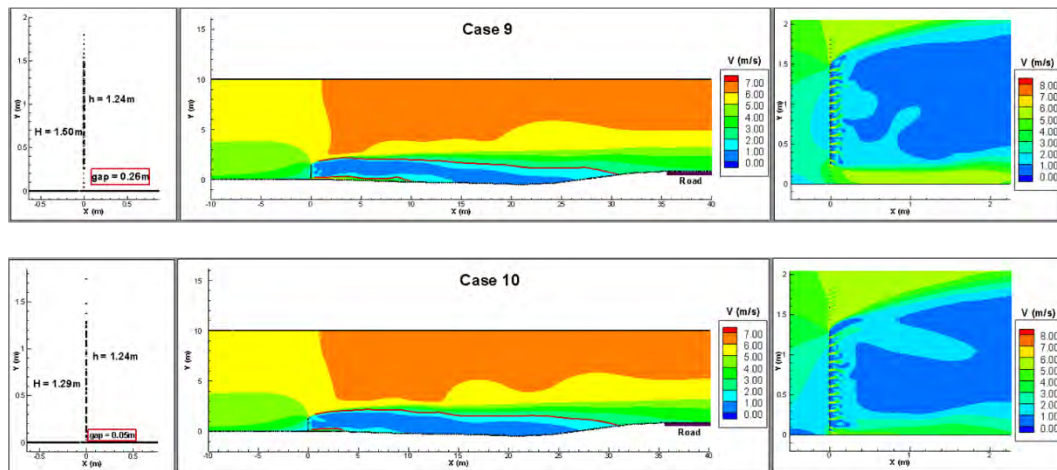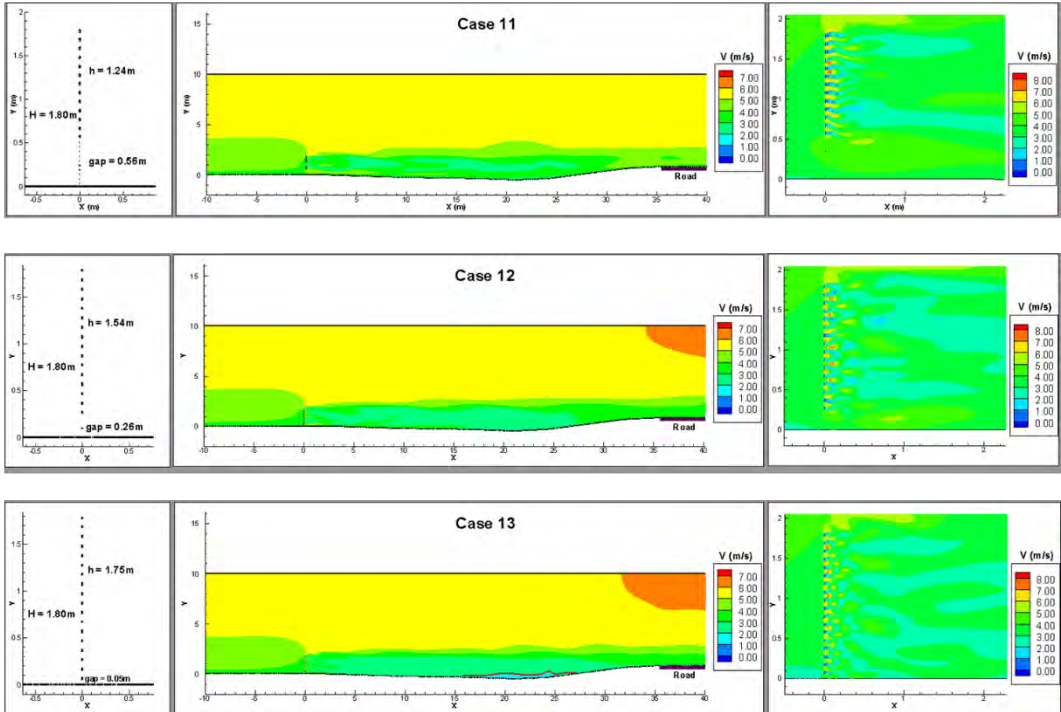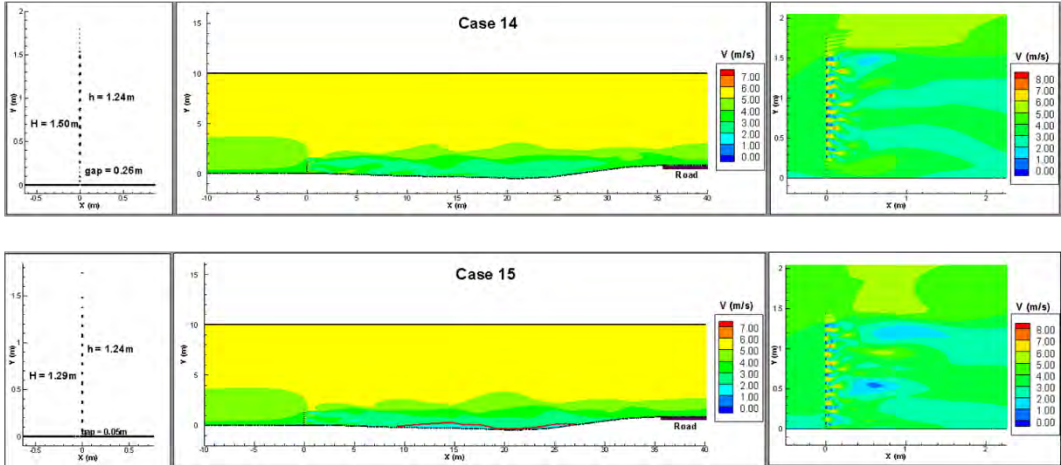

Figure 63. Distribution of velocity magnitude around and downstream of the fence designs with a porosity of 30%, setback distance of 35.5m.

Figure 64. Distribution of velocity magnitude around and downstream of the fence designs with a porosity of 70%, setback distance of 35.5m.

Figure 65. Distribution of velocity magnitude around and downstream of the fence designs with a porosity of 70%, setback distance of 35.5m.
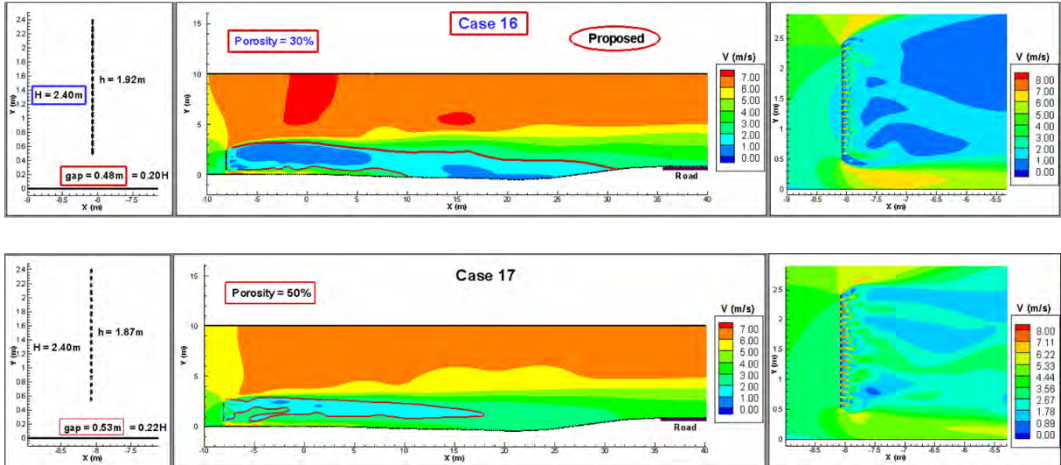
Figure 66. Distribution of velocity magnitude around and downstream of the fence designs with a porosity of 30% and 50%, setback distance of 40m.
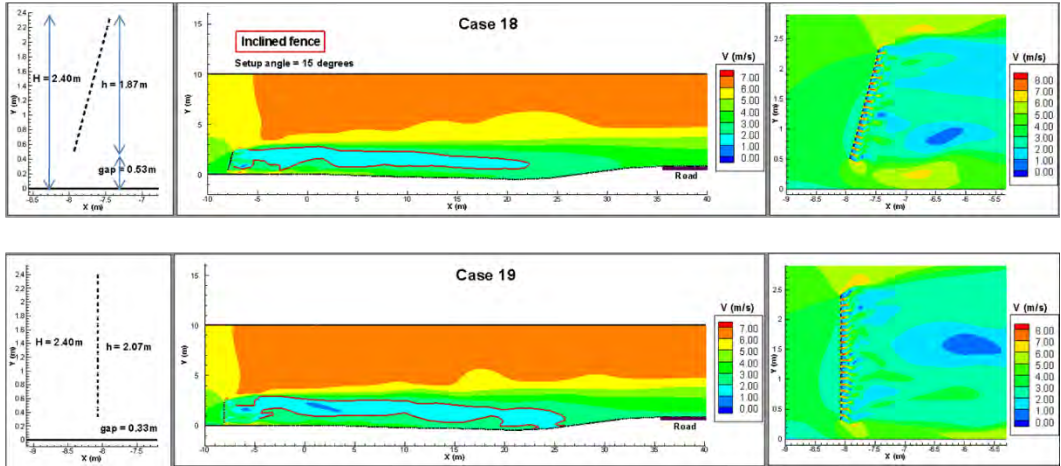

Figure 67. Distribution of velocity magnitude around and downstream of the fence designs with a porosity of 50%, setback distance of 40m, for inclined and vertical fence.
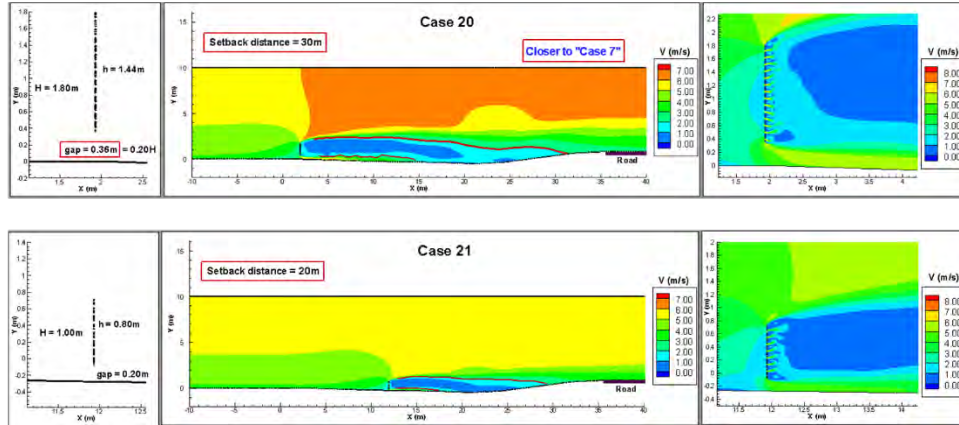
Figure 68. Distribution of velocity magnitude around and downstream of the fence designs for a porosity of 30% with setback distance of 30m and 20m.
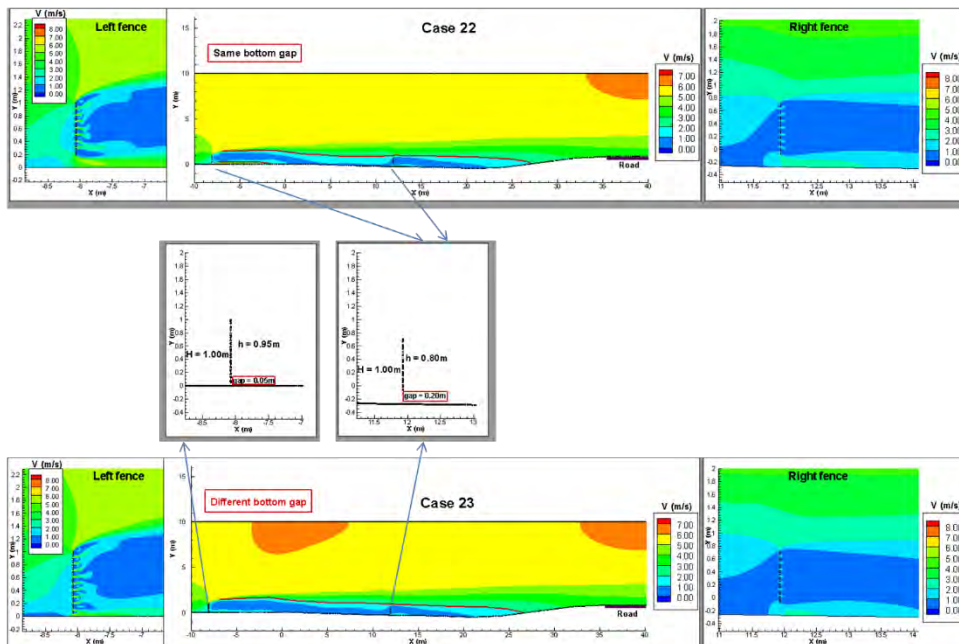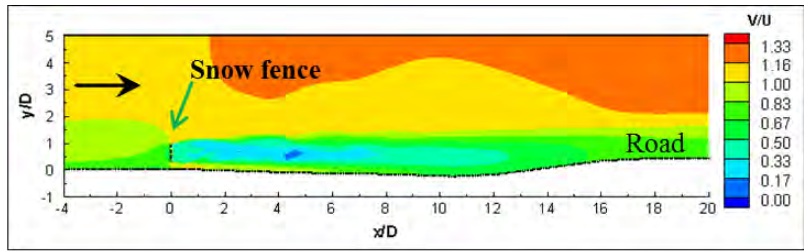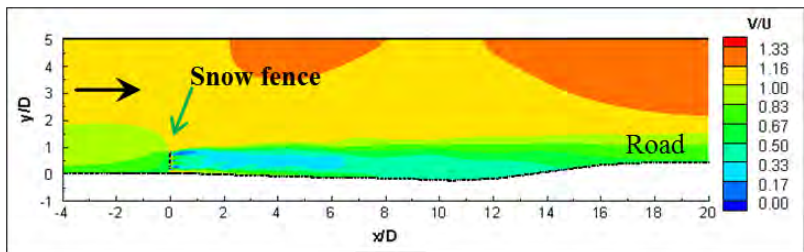

Figure 69. Distribution of velocity magnitude around and downstream of the double fence designs with a porosity of 30%, spacing of 20 m, setback distance of 20 m for same bottom gap fence designs and different bottom gap designs.

As already discussed, as part of the parametric study, we performed a number of simulations for fences with P=30% in which G/H was varied between 0.1H and 0.4H by keeping either h or H constant. Two of the designs (B1 and B2) that appeared to be the most promising based on the fact that the velocity magnitude field predicted by the simulation contained a long and relatively thick bottom region of reduced velocity magnitude (see Figures 71 and 70c) were tested in the field during the next winter. Besides these two new designs, the design A3 (also denoted B3) that worked the best for fences with P=50% was also tested. The fence height, h, in the cases with P=30% (design B1 has G/H=0.25 while design B2 has G/H=0.2) was about the same as that of design A3. One should also mention that the information presented in Figures 59 and 70 for the
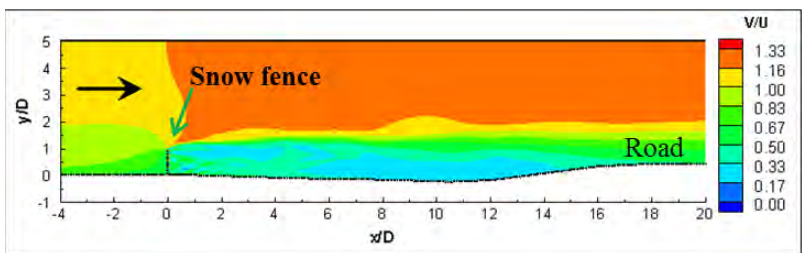
A1, A2 and A3 cases is equivalent. In one of the figures the data is presented in nondimensional form while in the other the velocity distribution is presented in dimensional form.

(a)

(b)

(c)

Figure 70. Distribution of velocity magnitude around and downstream of the fence designs with a porosity of 50% tested during the first winter (A1, A2, and A3). a) A1 fence: P=50%, G/H=0.34; b) A2 fence: P=50%, G/H=0.20; c) A3 fence: P=50%, G/H=0.08. D (= 2m) is the length scale characterized by average fence height and U (= 12m/s) is the mean incoming wind velocity. The fence is located at x = 0D.
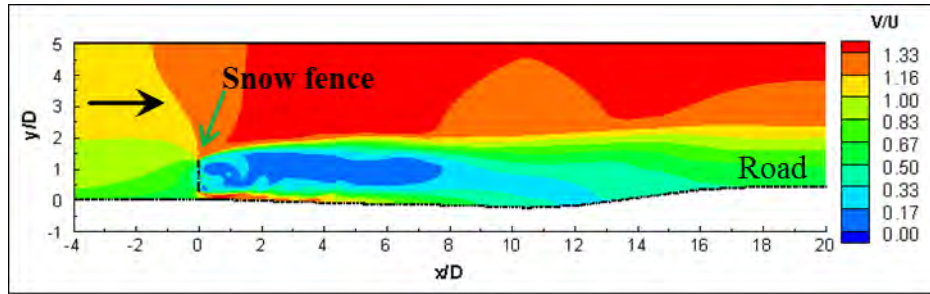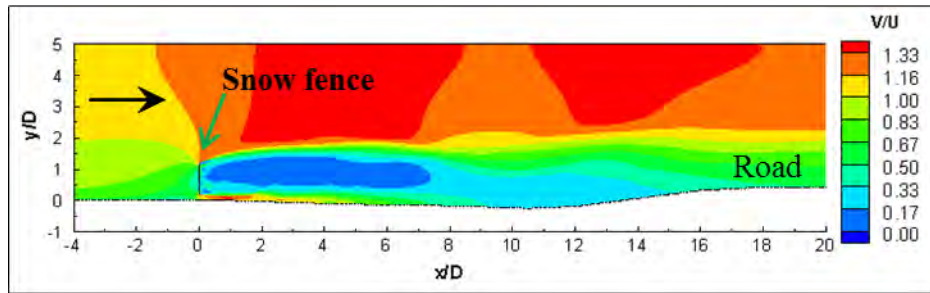
(a)

(b)

Figure 71. Distribution of velocity magnitude around and downstream of the fence designs with a porosity of 30% tested during the second winter (B1 and B2). a) B1 fence: P=30%, G/H=0.25; b) B2 fence: P=30%, G/H=0.20. D (= 2m) is the length scale characterized by average fence height and U (= 12m/s) is the mean incoming wind velocity. The fence is located at x = 0D.
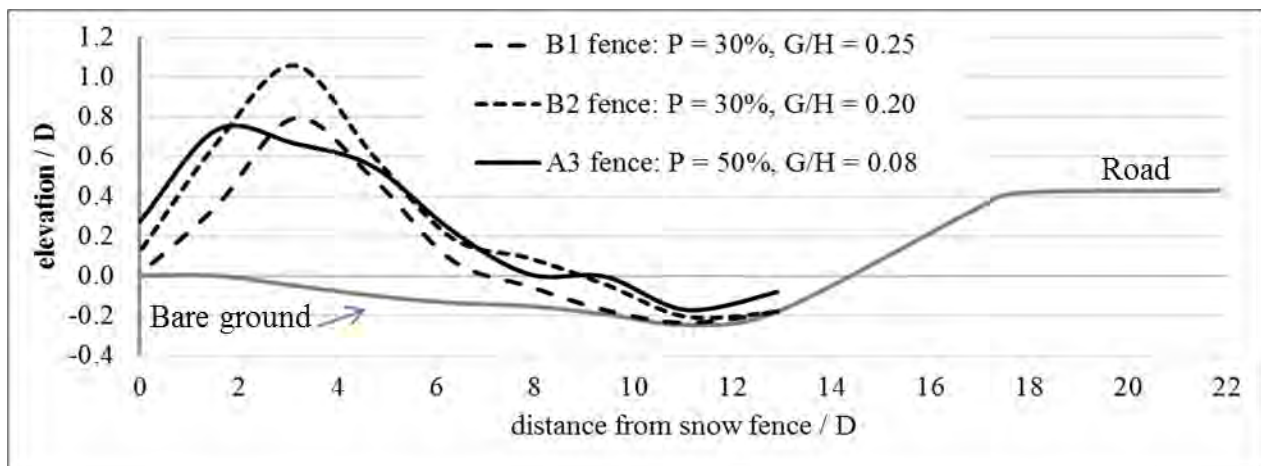

Figure 72. Snow deposition profiles behind the fence designs tested during the second winter (B1, B2, and A3). D (= 2m) is the length scale corresponding to the average fence height. The fence is located at x= 0D
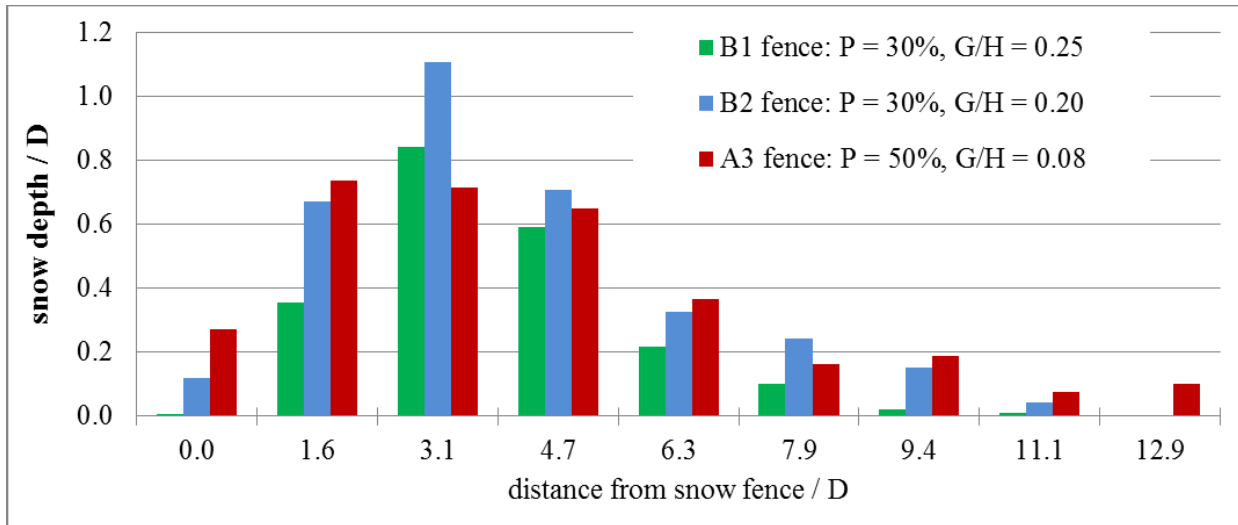
Figure 73. Comparison of snow depths deposited at 9 different downwind distances from the fence location for the three fence designs tested during the second winter (B1, B2, and A3). D (= 2m) is the length scale corresponding to the average fence height.

Figure 72 compares the snow deposition profiles measured after the most severe snow event recorded during the second winter. The total volume of snow deposit per unit length for designs B1 and B2 are by about 12% lower and 7% larger, respectively, than that for design A3. So, one can argue that all three designs retain a comparable amount of snow. However, there is an important difference in the snow deposition patterns. The length of the region where significant snow deposition occurs extends up to 20-25 m from the fence for the two designs with P=30% while the same region extends up to 30-35 m from the fence for design A3. For a snow event of slightly larger magnitude than the one analyzed in Figure 72, the region of snow deposition induced by the A3 fence design will reach the road.

Figure 73 compare the snow depths at each marker pole position along the marker pole line behind the three fences. The other problem with design A3 when compared to B2 and especially to B1 is the large snow height at the fence location. The snow level for design A3 is 0.55m, which means all the bottom gap region is filled with snow. The snow level within the bottom gap is around 0.5G for design B2 and is insignificant for design B1 (see Figure 73). This means that both designs with P=30% will continue reducing snow drifting on the road in the case of a larger snow event or if a subsequent snow event will occur a short time after the one analyzed in Figure 74. In conclusion, design B2 retains more snow but also has a smaller future capacity to continue accumulating snow compared to design B1. So, it appears the optimum G/H value for fences with porosity P=30% is situated somewhere in between 0.2 and 0.25 and the overall performance of these lower-porosity fences is better than that of design A3.

Figure 74. Views showing snow deposition close to the fence immediately after the end of the largest snow event during the second winter: a) B1 fence (P=30%, G/H=0.25 ; b) B2 fence (P=30%, G/H=0.2); and c) A3 fence (P=50% and G/H=0.08). The red lines indicate bottom of the fence.

4. USE OF PHOTOGRAMMETRY FOR REAL-TIME, CONTINUOUS MONITORING OF SNOW ACCUMULATION AT SNOW FENCES

Tracking of a snow event using automated image acquisition is an attractive aspect of CRP for this types of practical applications. For exemplification purposes, a 12.75 cm snowfall produced by a storm in the winter season of 2013-2014 is reported herein. The site was visited prior to the storm to conduct synoptic measurements (Protocol 1). During the event, the survey was made with images acquired with continuous monitoring (Protocol 2). Following the event, synoptic measurements were conducted again. The results reported below are obtained using only Protocol 2 measurements, i.e., un-assisted image recording using a minimal number of GCPs deployed in the field are only used for CRP processing. The RTK measurements obtained during and after the storm using Protocol 1 were acquired in very few cases. They are used in the reported example to confirm that the accuracy of the volume change estimation was within the desired accuracy. Images of the experiments and processing results are shown in Figure 75. The budget of snow change following the storm is presented in Figure 76.

The initial volume of 362 m^3 of snow deposited downwind the fence before the storm was increased to 443 m^3 due the fresh snow fall (see Figure 76). Full understanding of the snow drifting process as well as the evaluation of the efficiency of the fence retention capacity require knowledge of the wind and temperature variation during the storm. This information is typically available from meteorological stations surrounding the measurement locations. For our case study, six stations surrounding the site area were used to compile the meteorological information. It can be seen that the temperature remains roughly constant during the snow storm, making the analysis of snow tracking process more substantial compared to a situation where snow melting can affect the estimations. Similarly, the duration of the storm was short hence minimizing the potential effects of snow deposit compaction. The dominant wind driving the snow accumulation at the fence is about 55 km/h for the storm duration blowing perpendicular to the fence. This type of information combined with the dynamic monitoring approach of the snow volume change is critical for providing new insights in the investigation snow drifting processes.
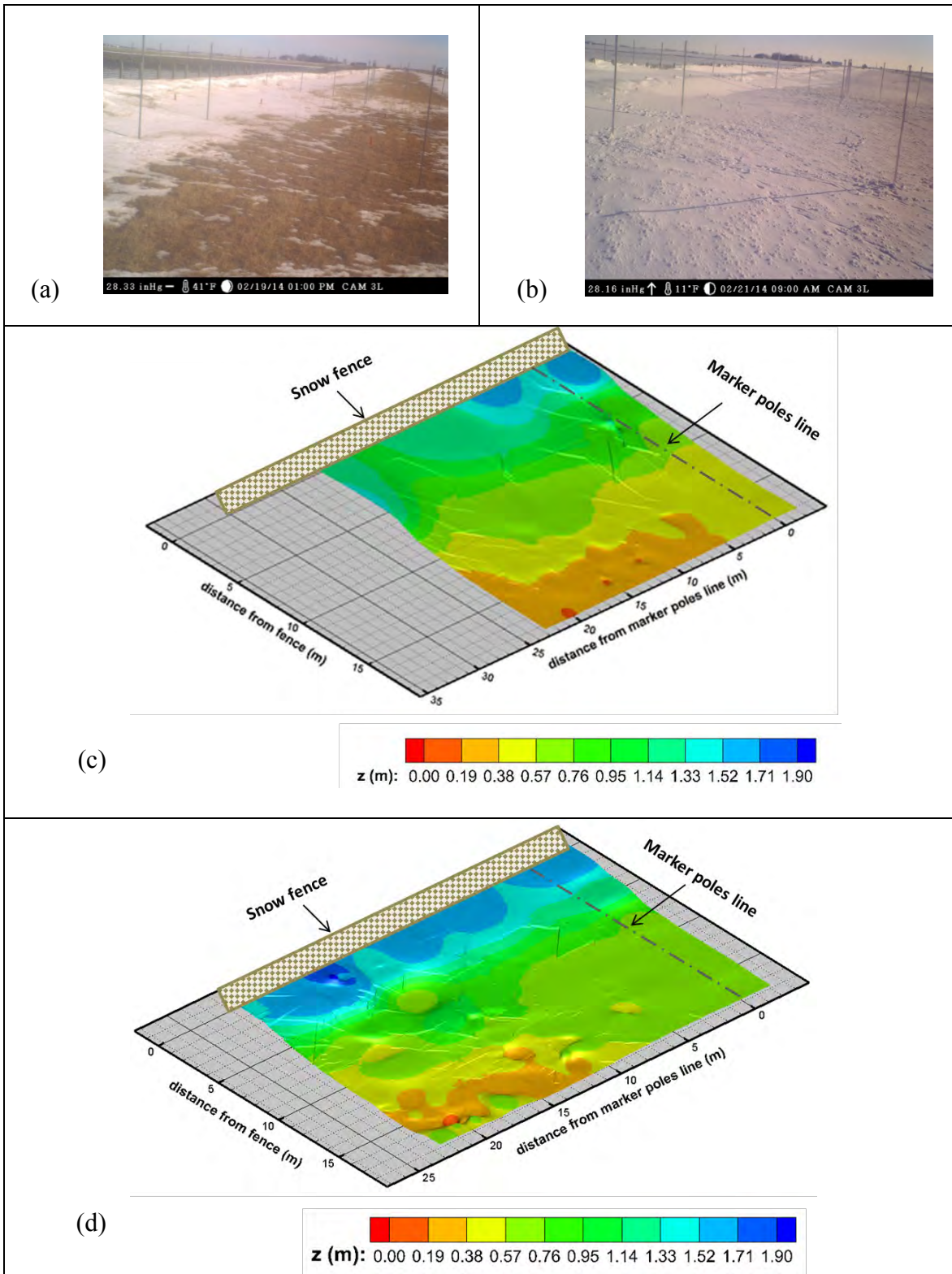
Figure 75. Snow tracking event using CRP: a) image of the pair before the storm; b) image of the CRP pair after the storm: c) mapping of the snow deposit before the storm; d) mapping of the snow deposit after the storm.
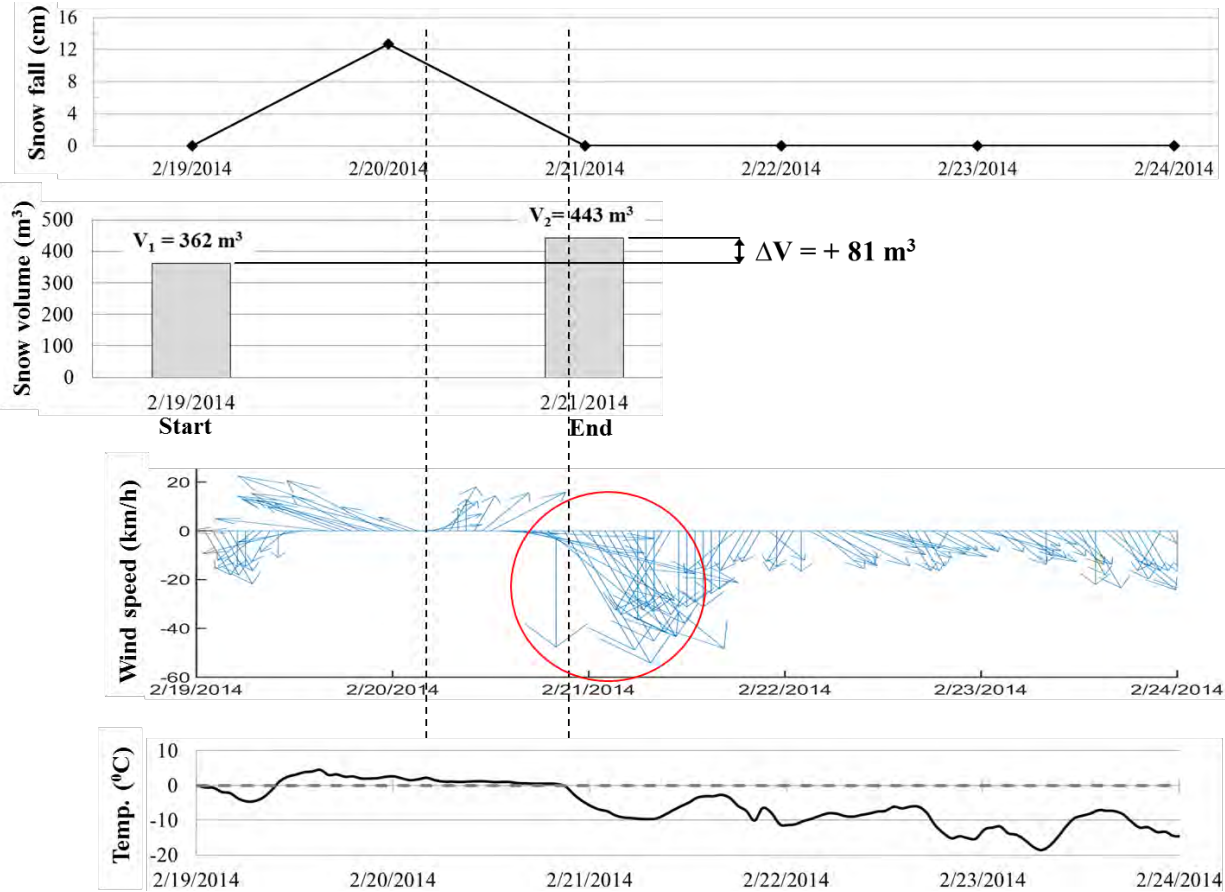
Figure 76. Illustration of the snow accumulation budget in a snow storm in conjunction with the time series of wind and temperature variation during the event. The significant snow fall period for the event is represented by the time period in between 2 parallel black dashed vertical lines. Red circle shows the direction of dominant wind (55km/h) for the event that is about perpendicular to the fence. Gray dashed horizontal line in the temperature plot represents freezing temperature. Data source for snow fall, wind and temperature: www.mesonet.agron.iastate.edu.

5. ADDITIONAL FIELD MONITORING OF SNOW FENCES AND NUMERICAL SIMULATIONS

5.1. OTHER FIELD SITES

As part of the present study, two additional sites (the Anamosa site on HW1 and a site situated on the I-35 road) were instrumented and monitored with similar equipment as for the Hwy 20 site (Williams). The Anamosa site feature three-dimensional snow transport features driven by local topography. The site was equipped with a temporary plastic snow fence during the 2010-2011 winter. The I-35 site was selected to observe retention of snow drifting by living snow fences. Three distinct lines of vegetation parallel to the road were in place at the I-35 site.

5.1.1. The Anamosa Site: Structural snow fence

The location of the Anamosa site is shown in Figure 77. This site is known to experience serious snow drift problems over winters where snow precipitation is large. The road is 6-ft lower than the adjacent land on the West side and is situated at approximately the same level with the adjacent land on the East side of the road. Figure 78 shows the pre-survey photographs of this site. The dominant wind direction was found to be from West to East while the road roughly runs from North to South. The narrow right-of-way limits the distance at which the fence can be places. A temporary snow fence (plastic) was installed during the first winter when the snow deposits were monitored. The snow fence was placed on a property adjacent to the road on the West side of the road, as shown in Figure 79. An electric pole was found in the site, as shown in Figures 79b and 79d. The pole was used to set the GPS camera for monitoring the snow accumulation during storm events.
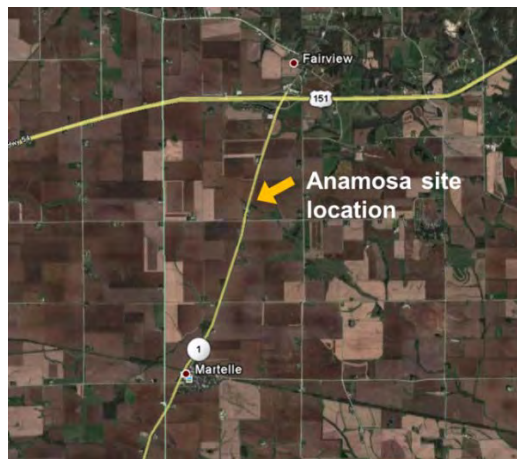

Figure 77. Anamosa site location from an aerial photo: Mile marker 118, Hwy 1, Anamosa.

Figure 78. Pre-survey performed at the Anamosa site (November 14, 2010).

Marker poles were installed at the observation site (see Figure 80). The marker poles were set perpendicular to the road in between the snow fence and the road shoulder. The marker poles were surveyed before the winter season at the ground level. After each storm, the snow deposits were mapped over the imaged area to capture the profile of the snow deposit produced by the snow fence. Direct tape measurements and DigiMap methods were also used in this site for the purpose of calculating the bareground profile and the snow profiles. Figure 81 and 82 display the comparison of the snow profiles measured using several surveying methods along with the bareground profile for two different events during the first winter. Similar to results obtained at the Williams site, the results given by the different surveying methods are in close agreement.

a)

b)

c)

d)

Figure 79. Pre-survey performed at the Anamosa site: a) View of the West side of the road; b) View of the road looking Eastward (road marker 118); c) Land adjacent to the West side of the road. The snow fence was placed about 70 ft away from the road; d) Pole suitable for positioning the camera.
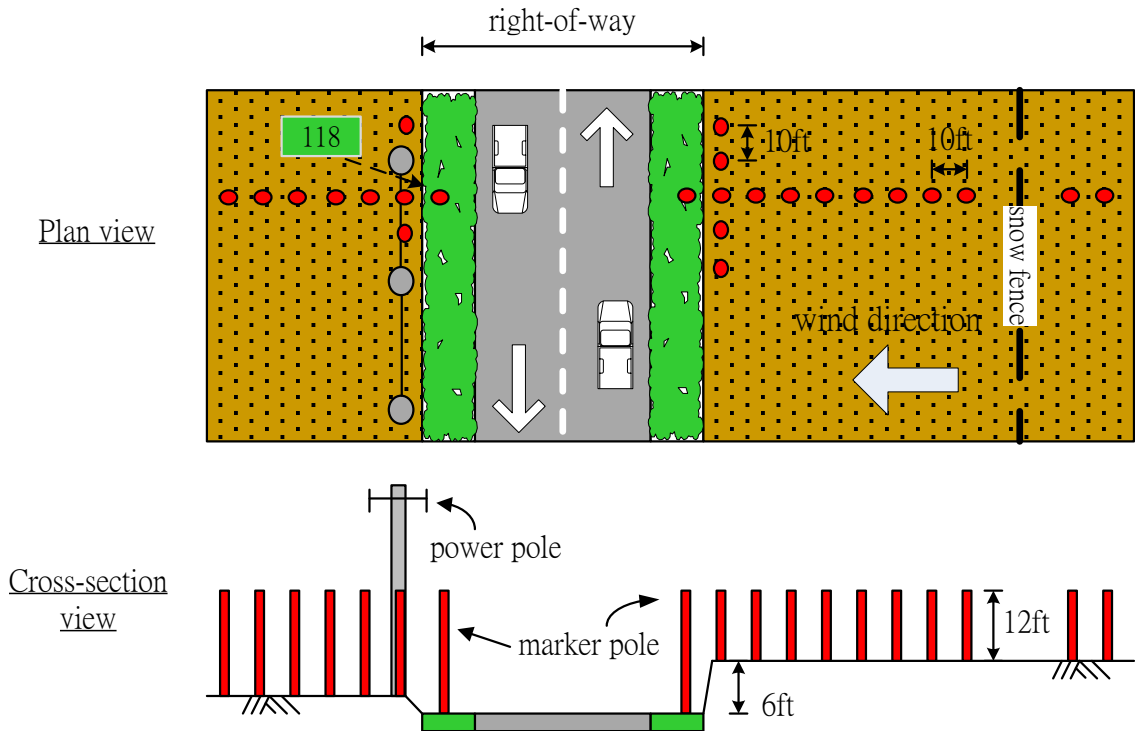
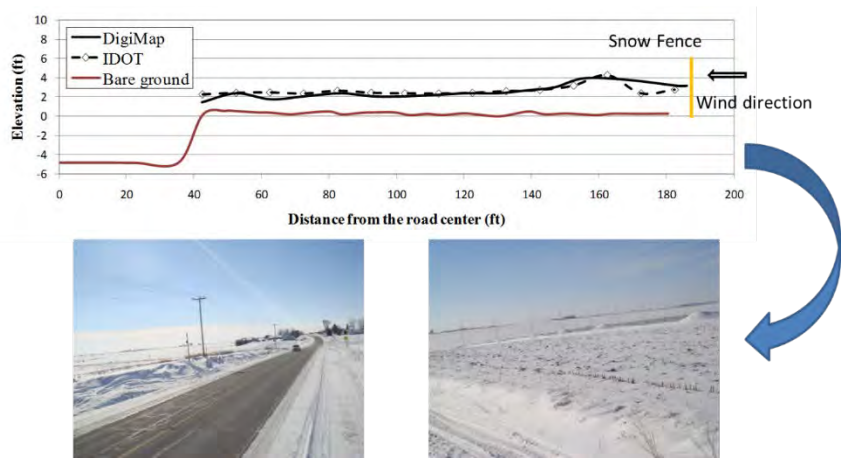Figure 80. Marker pole deployments at the Anamosa site

Figure 81. Snow deposition profiles at the Anamosa site (January 20, 2011).
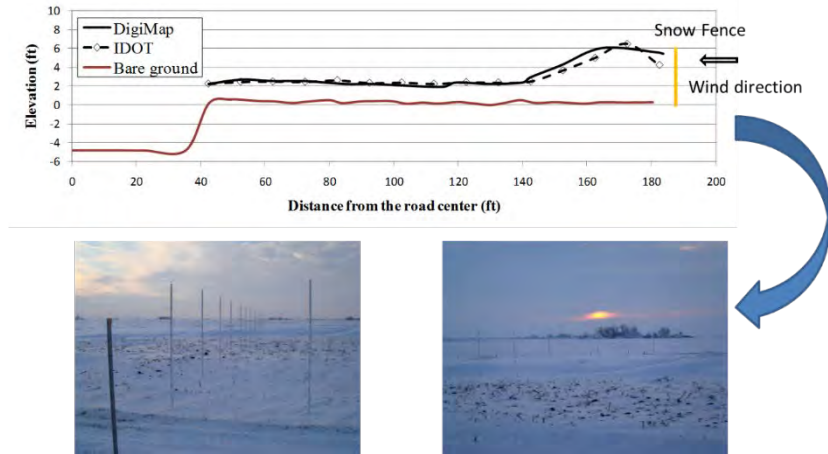
Figure 82. Snow deposition profiles at the Anamosa site (February 5, 2011).

5.1.2. The I-35 Site: Living snow fence

One of the most common types of living snow fences in Iowa consists of multiple rows of corn. Other popular types of snow fences include the planting two rows of trees or shrubs parallel to the roadway. The initial goal of this part of the study was to optimize the design recommendation for living snow fences containing rows of corn. Unfortunately, this was not possible due to the increased price of corn which led the owners to cut the corn until the road. As a result, after discussions with the AC committee it was decided to perform monitoring of a living snow fence containing trees and shrubs as a proof of concept exercise.

Besides the Williams site, field monitoring of the efficiency of living snow fences was performed on the I-35 road, not far from the Williams site. The position of the site is illustrated in Figure 83. A view of the I-35 site is shown in Figure 84. The living snow fences at both sides of the road were monitored. The road level at this site is higher than the adjacent landside. The dominant wind direction is NW to SE (see Figures 86 and 87), and the road runs on the N-S direction with a very narrow right of way compared to the Williams site. The shoulder makes a difficult access for the PIV truck and LiDAR measurements for normal conditions. During storms, measurements might require the creation of pull over areas such that the PIV truck does not interfere with the traffic. The view in Figure 84 also displays the web cameras installed at the pole used to monitor the site remotely.
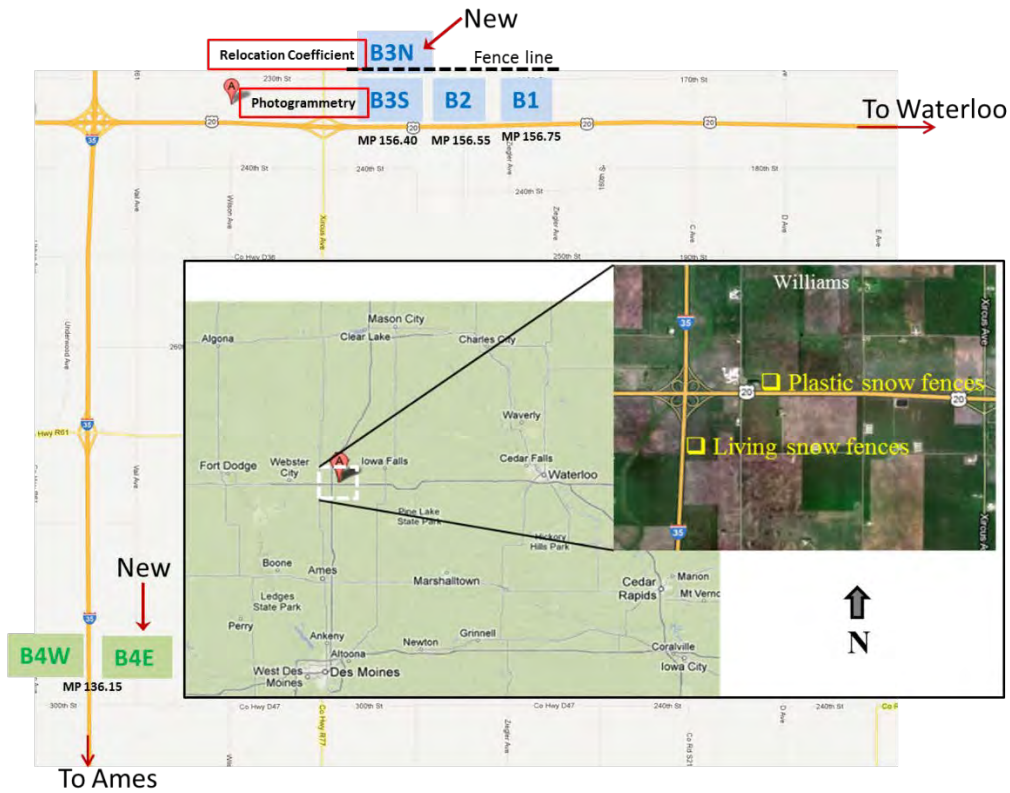
Figure 83. Site location of living snow fence at the I-35 site.

Figure 84. View of the I-35 site with the living snow fence protecting it

Marker poles arranged as shown in Figure 85 were installed at the observation site. Similar to the procedure adopted at the Williams site, marker poles were needed to assist the topographic surveys. The marker poles were set perpendicular to the road in between the snow fence and the road shoulder. The marker poles were surveyed before the winter season at ground level. After each storm, the snow deposits were mapped over the imaged area to capture the 3-D topology of the snow deposit produced by the snow fence.

Figure 85. Marker poles layout at both sides of the I-35 site.

Figure 86. Snow deposition after a snow storm close to the living snow fence at west side and the living snow fence at the east side.

Figure 87. Analysis of snow deposition at different areas of the living snow fence present at the west side of the I-35 road.
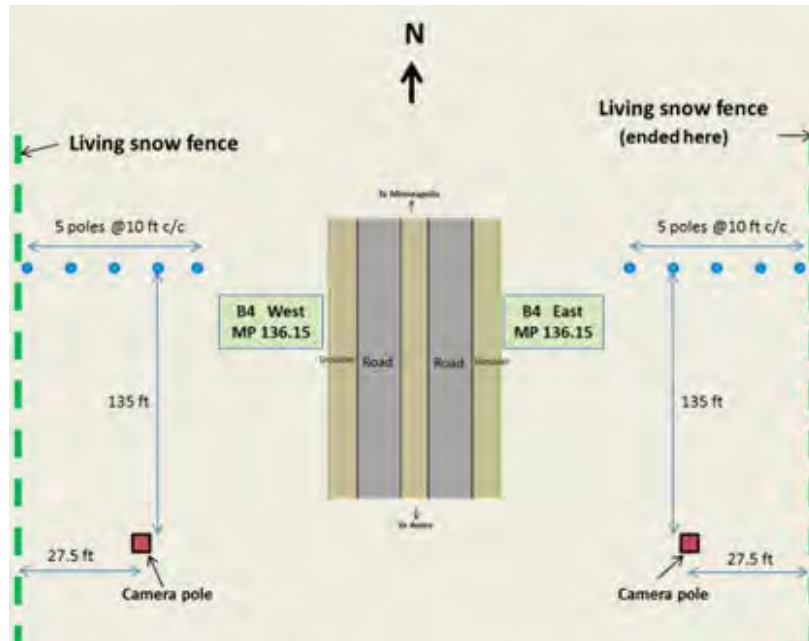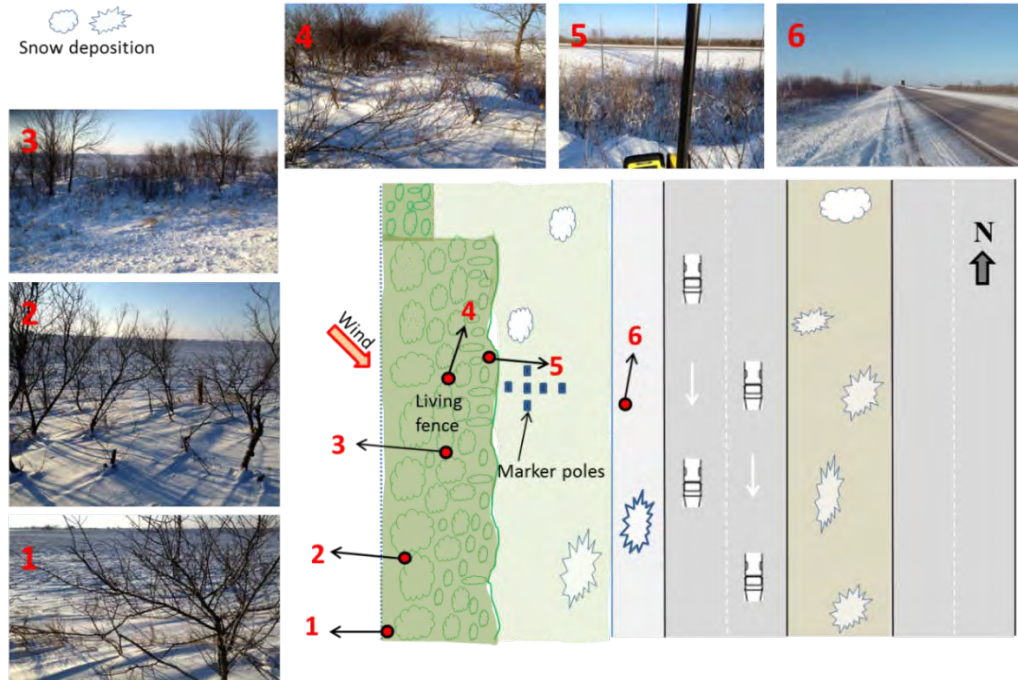
The efficiency of the living snow fence at each side of the road was analyzed during several snow events. Images of the snow accumulation at the site were captured from different angles, as shown in Figures 86 and 87. After investigating the snow accumulations at the site during numerous snow events in both the first and the second winter seasons, it was found that the living snow fence on the west side performed the best compared to that on the east side. This result makes sense as the dominant wind is oriented from the NW to the SE direction. Overall, the living snow fence at the I-35 site worked well over the two seasons the field monitoring was done. Unfortunately, the characteristics of the living snow fence were fairly variable along the road. As a result, we were not able to assess the efficiency of different designs of living snow fences (e.g., in terms of the height and width of the vegetation at the site, its average porosity, etc.) under close to identical conditions.

5.1.2.1. Simulation of flow past living snow fences

As already mentioned, the joint experimental and numerical approach to improve the design of snow fences exemplified in the previous sections for plastic snow fences can be used for any types of snow fences provided that one can test several fence designs at the same site under close to identical conditions. One of the main step of the design procedure is to perform numerical simulations of the airflow past fences with different designs. Based on the numerical results a subset of the designs considered will be chosen to be tested in the field. As a proof-of-concept in the present subsection we tried to simulate the flow past one of the living snow fences present at the   I-35 site. For this, pictures of the living snow fences were analyzed to determine the extent and the typical size of the vegetation at that site over a length of the road where the vegetation characteristics were close to constant. Basically, that site contains four rows of vegetation. The

first row is more mature and contains a row of trees while the last three rows, situated closer to the road, are much younger and of smaller height. The average diameter of the branches (9 cm for the tree trunk and 3 cm for larger branches) was used to determine the size of the porosity elements within the porous regions. The porous regions were assumed to have close to constant porosity, which is a good approximation of real conditions. Figure 88 shows the 2D computational domain with the location and spatial extent of the two living snow fences. Also shown in an inset is the distribution of the porous elements within the porous regions. If more detailed data is available from field observations and lab measurements of the porosity of the vegetation present at the site, this information (e.g., variable porosity within the different porous regions) can be easily incorporated in the numerical model.
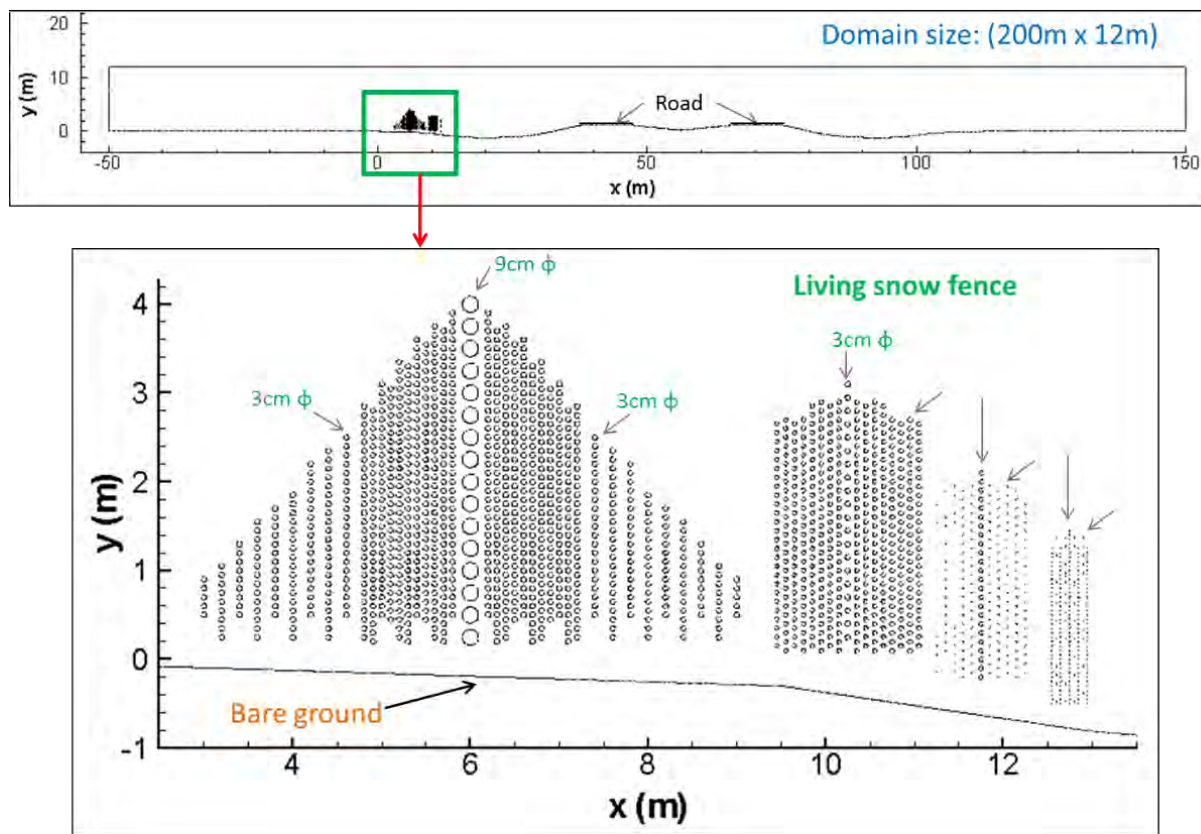
Figure 88. Computational domain and geometry of the living snow fence in the numerical model based of the living snow fence present on the west side of the I-35 site.

The other main variable that has to be given is the porosity value. Typical values of the porosity for trees and bushes ranges for 90% to 98%, though even lower values can be observed during the winter time when the leaves are all gone. As a proof of concept we performed three simulations with porosities of 90%, 95% and 97.5%, respectively, which is representative of the range of porosities expected for the living snow fences present at the site. Similar to the cases when simulation past plastic snow fences were performed, a fine mesh that resolves the wakes of all the porosity elements was generated. The mesh was gradually refined as one gets away from the

porous regions. Several views of one of the meshes used to perform simulations are shown in Figure 89.

Figure 89. Mesh around the bed and elements of the porous region corresponding to the living snow fence.
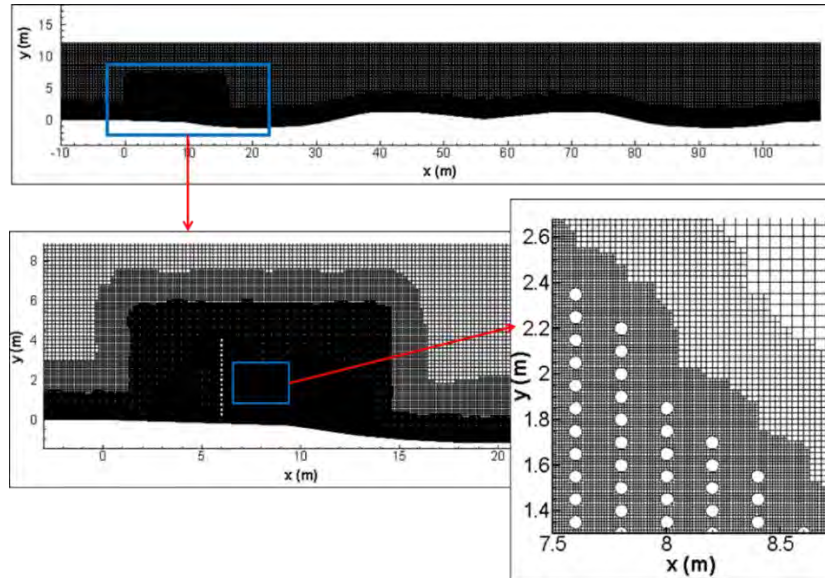
Figures 90 and 91 compare the velocity magnitude flow fields and the 2D streamline patterns from the three simulations. Using the same analysis as the one performed for plastic snow fences, one can conclude that among the three designs analyzed the 95% porosity case has the best chance of working well in the field. The design with a lower porosity of 90% predicts the formation of a region of low near-bed velocity downstream of the living fence, but this region extends over the road. This suggests that for stronger snow events, the presence of the living fence can induce snow deposition on the road side situated closer to the fence. Moreover, the turbulent kinetic energy distributions in Figure 92 show that very large tke values are induced over the road, including at the level of the drivers. This can create another problem that negatively affects traffic safety. The problems are much less for the other two designs tested.

In the case with a porosity of 95% the region of low velocity magnitude does not extent over the road and more than that, velocity magnitude is small inside the ditch where snow accumulations is acceptable. The case with a porosity of 97.5% does not appear to be able to slow the airflow past the living snow fence enough to create the conditions for large deposition of the snow flakes immediately downwind of the fence. This is also suggested by the 2D streamlines patterns in Figure 91 where there is no evidence of the solving down of the flow to start forming a recirculation region. The patterns are fairly similar to those observed for plastic snow fences with a porosity of 70%. Of course these findings have to be confirmed using monitoring in the field.

The present method is particularly well suited for analysis of the performance of living snow fences where the main vegetation elements can be easily described in terms of mean size and solid volume fraction. Living snow fences consisting of arrays of corn are an excellent example. However, for the reasons mentioned before, we were not able to monitor a site where corn was used as a living snow fence.
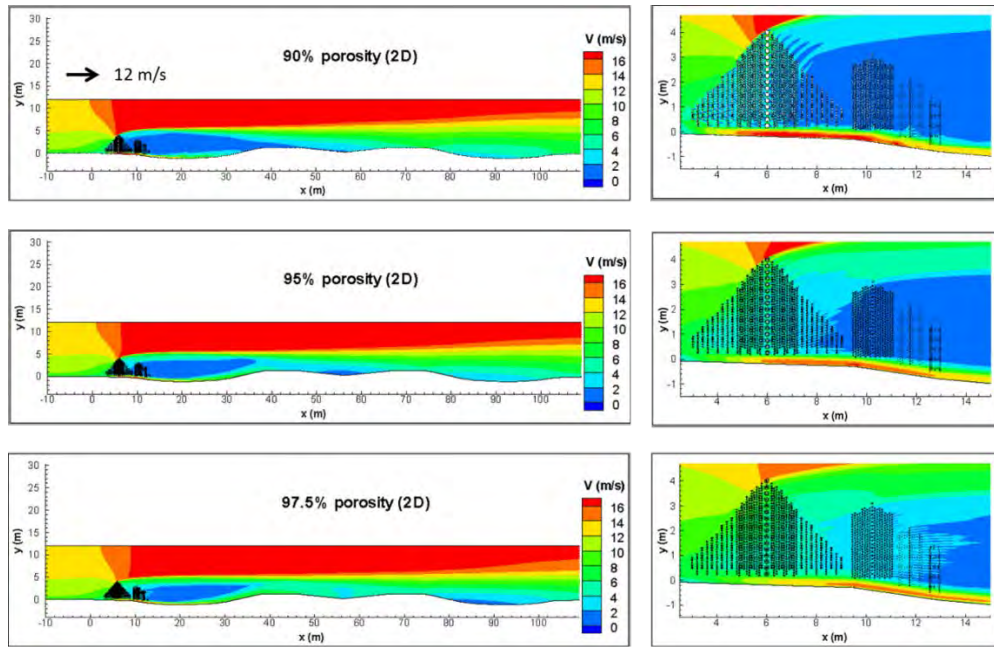
Figure 90. Effect of living snow fence porosity on mean velocity magnitude distribution around the fence.
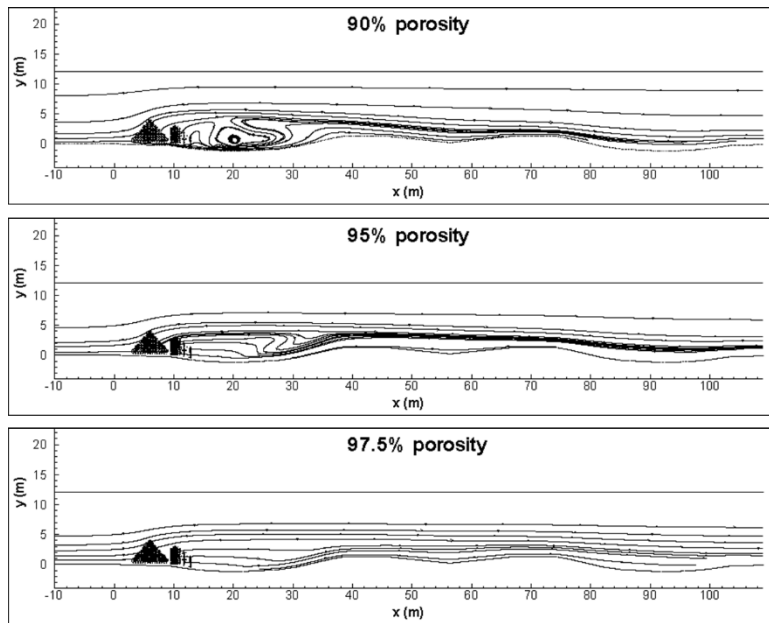

Figure 91. Effect of living snow fence porosity on 2-D streamline patterns distribution around the fence.
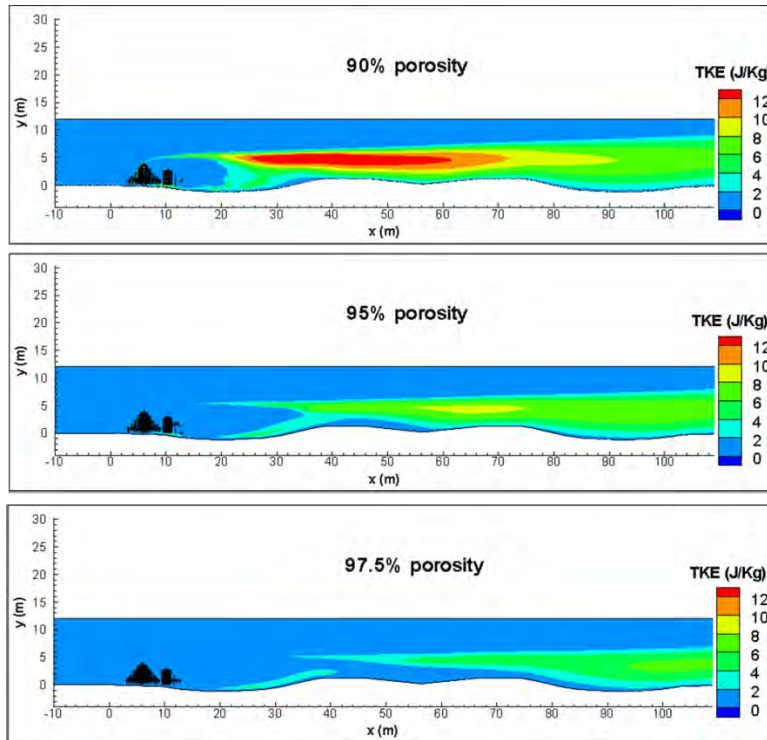
Figure 92. Effect of living snow fence porosity on turbulent kinetic energy distribution around the fence.

5.2. FURTHER INVESTIGATION OF PERFORMANCE OF BEST FENCE DESIGNS WITH POROSITIES OF 30% AND 50%

The three designs of snow fences (B1, B2 and A3/B3) were monitored during a third winter season (fourth year of the study, given that snow deposits were insignificant during the second year of the study) where the snow precipitation was very large and the snow characteristics during some of the snow events was very different than that of the typical snow events recorded over the other two winter seasons. The performances of the best fence design with P=50% (A3 fence) and the two candidates for best design for fences with P=30% (B1 and B2) were monitored in the field using the same criteria as those described for the field monitoring campaign undertaken during the second year.

The snow deposits after a major storm that occurred on January 22, 2014 are compared in Figure 93 based on pictures taken at the site. The snow characteristics were similar to those of the major snow events during the previous two winter seasons. Following this major snow event, the bottom gap of the two 30% porosity designs (B1 and B2) is not filled with snow, while the bottom gap of the conventional 50% porosity design (A3) is already filled with snow.   Thus the better performance of the newly proposed designs with a porosity of 30% and a relative bottom gap clearance of 0.2-0.25 were found to work better compared to the conventional design.

The largest snow storm during the third winter season occurred on February 21, 2014. The interesting fact about this storm was that icy rain was recorded on February 20, 2014. This was

followed by massive snow precipitations on February 21, 2014. To investigate the effectiveness of the 30% and 50% porosity design for such special conditions, the snow deposition patterns around and near the three fences (B1, B2 and A3) are compared during the icy rain event (February 20, 2014) in Figure 94 and immediately after the end of the snow event with regular type of snow (February 21, 2014) in Figure 95.

Analysis of Figure 94 allows us to focus only on the effects of the icy rain on the fence. The plastic surface of all the three fences is covered by the icy rain. Since the bottom gap of the A3 fence is already covered by the snow prior to the icy rain event and the remaining part of the fence (plastic surface only) is also covered by the icy rain, one can expect the A3 fence will act as a solid fence with about 0% porosity and its capacity to alleviate snow drifting problems during the February 20 and 21 events will be negligible. Meanwhile, the bottom gaps of the B1 and B2 fences are still not filled by snow or ice. Though during the time the ice fills the openings of the plastic snow fence the capacity of these fences to retain snow is reduced, this capacity is non-negligible.

Figure 95 compares the snow deposition patterns around the three fences immediately after the end of the largest snow event on February 21, 2014. The snow profiles obtained from field measurements before and after the most significant snow event during the 3rd winter season for the three fence designs are compared in Figure 96. As expected, the B3 fence was completely submerged by snow because this fence behaved as a solid fence with no bottom gap after the icy rain event on February 20, 2014. Therefore this snow fence was not able to protect against snow drifting effects past February 20, 2014. Meanwhile, a significant part of the B1 and B2 fences were still not submerged under deposited snow close to these fences. The plastic surface of the B2 fence (G/H=0.2) was covered by icy rain but the fence was not completely submerged by deposited snow. Therefore B2 fence will act as a solid fence but only in the case of continuation of the largest snow storm. More importantly, the plastic surface of the B1 fence (G/H=0.25) not submerged under deposited snow was already free from icy rain coverage on February 21, 2014. This means that the B1 fence continued to work as a regular snow fence during the largest snow storm on February 21, 2014.
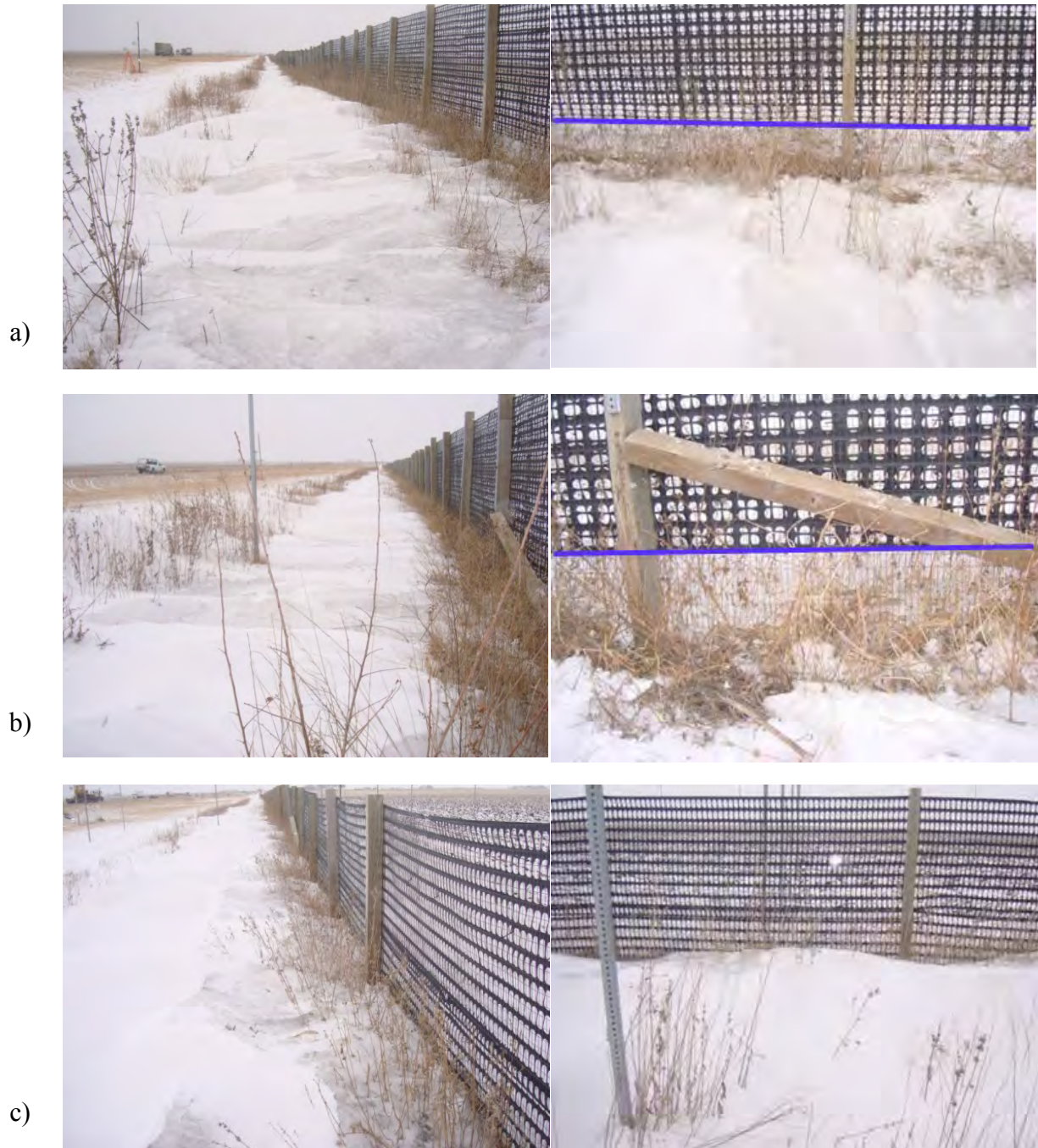
Figure 93. Views showing snow deposition close to the fence on January 22, 2014 immediately after the end of one of the significant snow events occurring during the third winter season: a) B1 fence (P=30%, G/H=0.25 ; b) B2 fence (P=30%, G/H=0.2); and c) A3 fence (P=50% and G/H=0.08). The blue lines indicate bottom of the fence.

Figure 94. Views showing snow deposition close to the fence during the icy rain event on February 20, 2014 which is followed by the most significant snow storm of the third winter season on February 21, 2014: a) B1 fence (P=30%, G/H=0.25 ; b) B2 fence (P=30%, G/H=0.2); and c) A3 fence (P=50% and G/H=0.08). The blue lines indicate bottom of the fence.

Figure 95. Views showing snow deposition close to the fence immediately after the end of the largest snow event during the third winter season: a) B1 fence (P=30%, G/H=0.25 ; b) B2 fence (P=30%, G/H=0.2); and c) A3 fence (P=50% and G/H=0.08).

In conclusion, the field monitoring study conducted during the 2013-2014 winter season reconfirmed the main conclusions of the previous field monitoring study that the optimum design corresponds to plastic snow fences with a porosity of 30% and a relative bottom gap of 0.25%. The additional important finding was that the design continues to work well for even more severe snow events containing regular snow than those observed over the previous years and that the design did not fail even for events that were characterized by the presence over a limited time of icy rain precipitations.
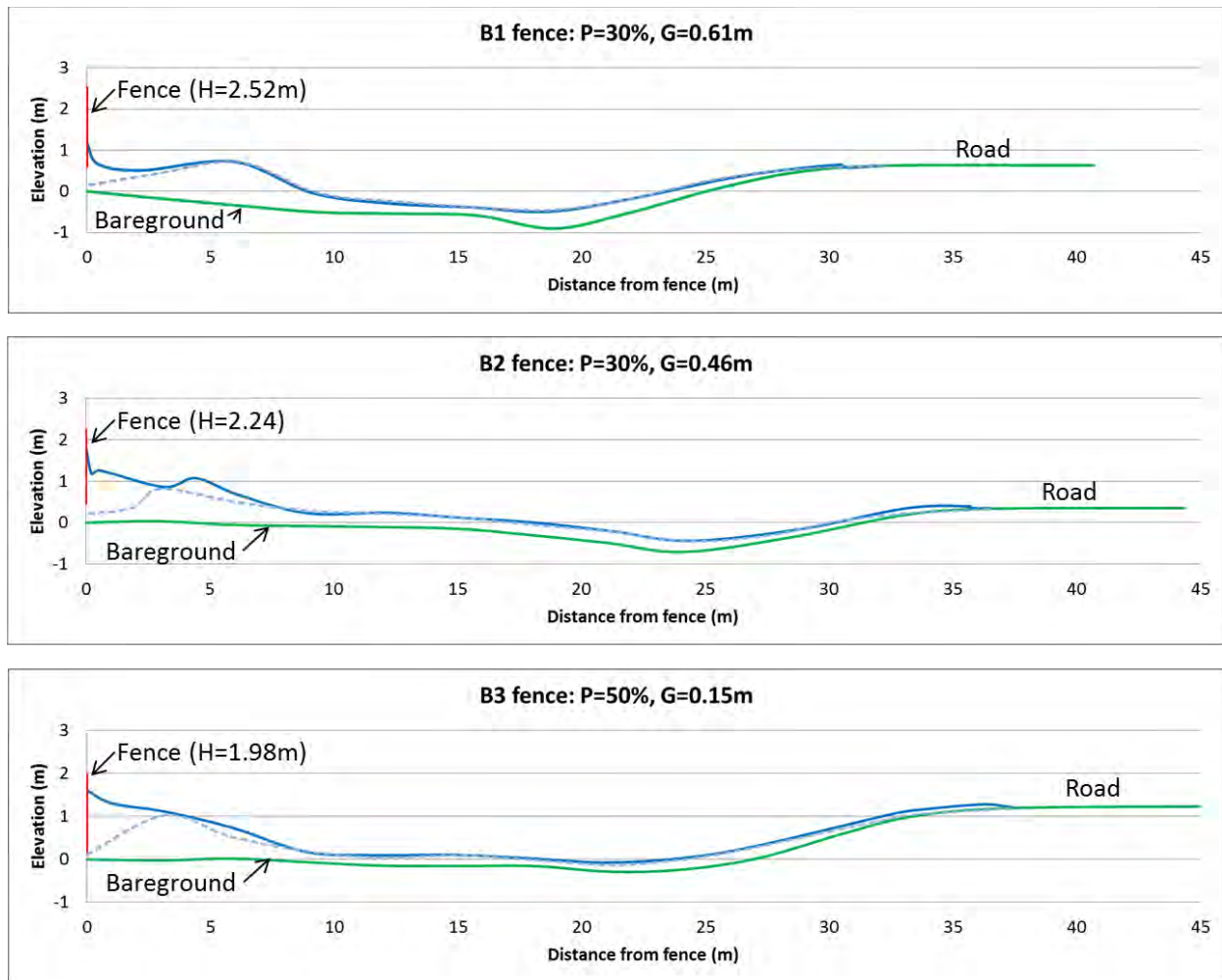
Figure 96. Snow Profiles at the end of two major storm events during the third winter season
(———— Feb 21, 2014 and - - - - Feb 15, 2014).

5.3. NUMERICAL SIMULATIONS OF FLOW PAST BLOWER-TYPE SNOW FENCES

Besides the classical types of snow fences used by the IDOT, the present study investigated other non-conventional types of snow fences that can be used for protection against snow drifting in regions with narrow rights of ways. Such snow fences were successfully used especially in Asian countries (e.g., Japan) and European countries. Figure 97 shows one such blower snow fence containing airfoil snow plates placed on a relatively large road in Spain. Field monitoring at that site has shown this type of snow fences are very effective to alleviate snow deposition on the road and increase driver visibility during major snow events. Observe that the snow fence is placed in the immediate vicinity of the road, as opposed to classical snow fences where the fence is placed at a distance from the road that is a multiple of the fence height. In the example shown in Figure 97, 6 airfoil plates are disposed uniformly over the whole height of the fence but other design contain airflow plates only on the top part of the fence. The plates are fixed in place using vertical posts. While in some cases the elements are simple plates oriented at a certain angle with the

96

vertical, in other cases the plates are formed from 2 or more straight elements oriented at different angles with the vertical or with plates that have the shape of an airfoil (see Figures 98, 99, 100, 101). Of course as the shape of the airfoil becomes more complex, the cost of the snow fence increases. The main design variable is the angle between the different components of the plates and the vertical. A second variable is the length of the plate. Finally, the height range and the number of plates disposed on the fence and the bottom gap are also important design variables. Several studies used field monitoring, laboratory experiments and numerical simulations to optimize the performance of these fences (Haniu et al., 1995, Sakamoto et al., 2001, Nieto et al. 2010). Final design solutions are generally different from group to group. For example, Figure 102 shows snow deposition profiles from a series of field experiments performed with blow-off snow fences of conventional design and with an optimized design by Sakamoto et al (2001). Based on both wind tunnel and field observation experiments the performance of the blow-off snow fence with airfoil plates of improved design was found to greatly reduce the amount of snow deposited on the road and in its immediate vicinity compared to blow-off snow fences of conventional design.

Though more expensive than conventional fences, they may be the only option for cases where narrow rights of way do not allow to install standard fences at a sufficient distance from the road such that the snow retained be these fences does not extend over the road. The principle of these new types of snow fences is in a way opposite to that of a classical snow fence, in the sense that they are designed to impede the deposition of snow in their vicinity. To be effective, such snow fences, generally called blow-off snow fences, have to be placed in the immediate vicinity of the roads. Sakamoto et al. (2001) found that the airfoils of blow-off snow fences, when correctly designed, can prevent the alternating rolling-up of the bottom gap flow and the separated shear layer separation the top of the snow fence. Optimum configurations were designed to impede the alternating rolling of the airflow behind the snow fence.

Their main limitation is that they are effective in impeding snow deposition over a limited distance, so their use for very wide roads like highways containing ditches is problematic. Still, such solutions are of interest. As such, some numerical simulations were performed to understand the aerodynamic effects associated with the presence of airfoil plates on the air flow fields in the vicinity of the blow-off snow fence. This also demonstrates the capacity of the numerical model to deal with very different types of snow fences and to produce detailed information of the mean velocity and turbulence statistics close to the fence and over the road protected by the fence. Such information can be used to optimize the design of any type of snow fences, while taking into account the aerodynamics mechanism used to protect against snow drifting effects may be very different for one type of snow fence compared to other types.
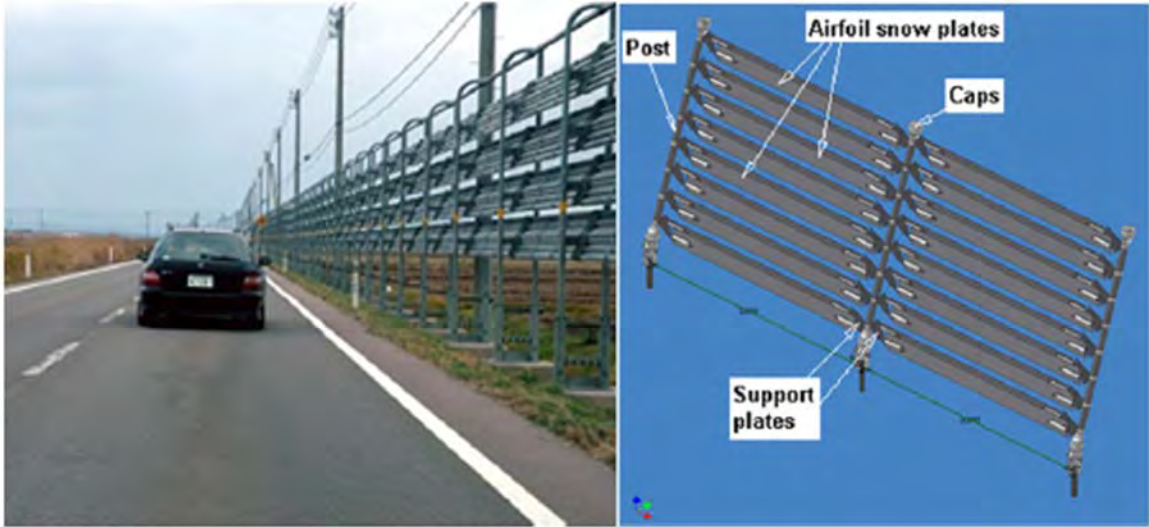
Figure 97. View of a snow fence with airfoil snow plates: At the side of an actual road (left) and its CAD design (right) (from P. J. Garcia Nieto et. al, 2010).
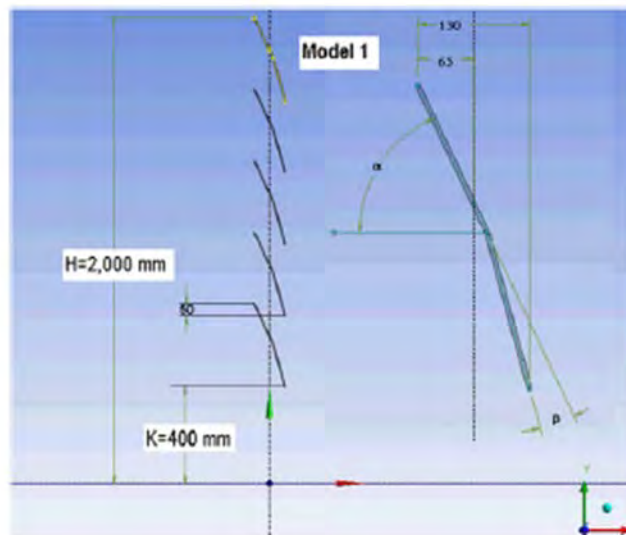
Figure 98. Shape of the snow fence containing airfoil plates considered in the numerical study of P. J. Garcia Nieto et al. (2010).
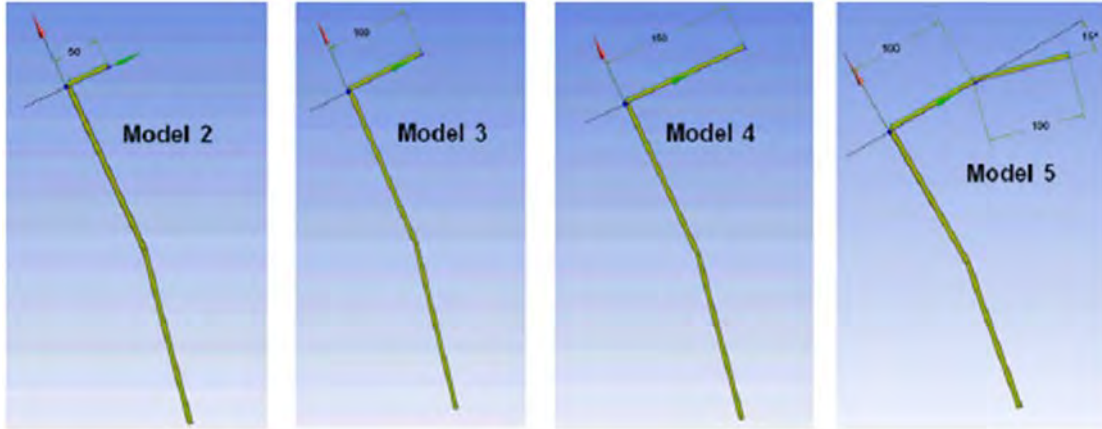
Figure 99. Variations of the basic shape considered in the numerical study of Garcia Nieto et. al, (2010). The main design variables were the length and shape of the flaps of the upper plate of the blow-off snow fence.

H: Snow fence height
β: Setup angle
K: Bottom gap

(a) Snow fence with Joukowsky snow

(b) Snow fence with circular arc snow

(c) Conventional snow fence with flat snow plates

Figure 100. Blow-off snow fence configurations considered in the field and laboratory study of Sakamoto et. al (2001). Besides the angle of the plates, the shape of the plates was a main design parameter.

99

Figure 101. Circular arc airfoil snow plate used in the study of Sakamoto et. al (2001).

Figure 102. Field observations showing snow deposition profiles after a major snow event where blow-off snow fences of different designs were tested (from Sakamoto et. al, 2001).

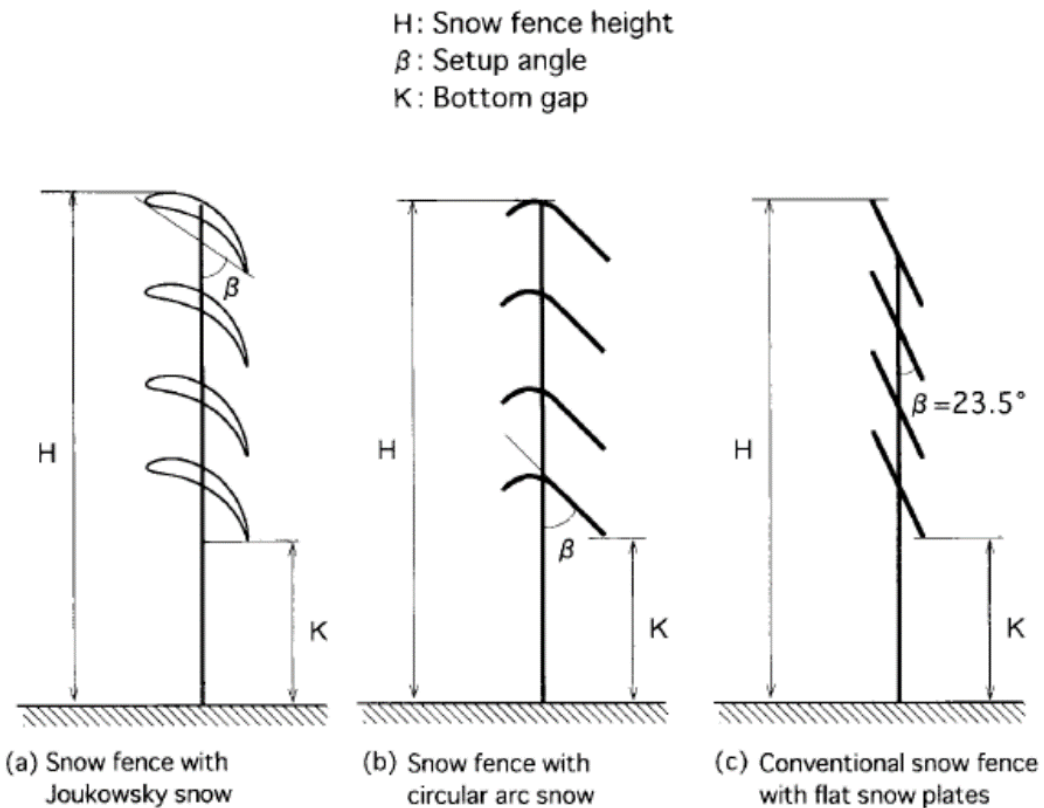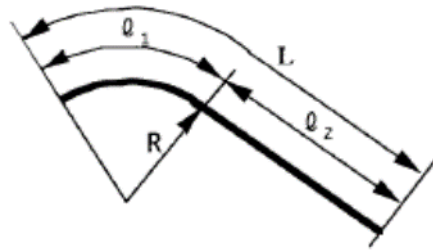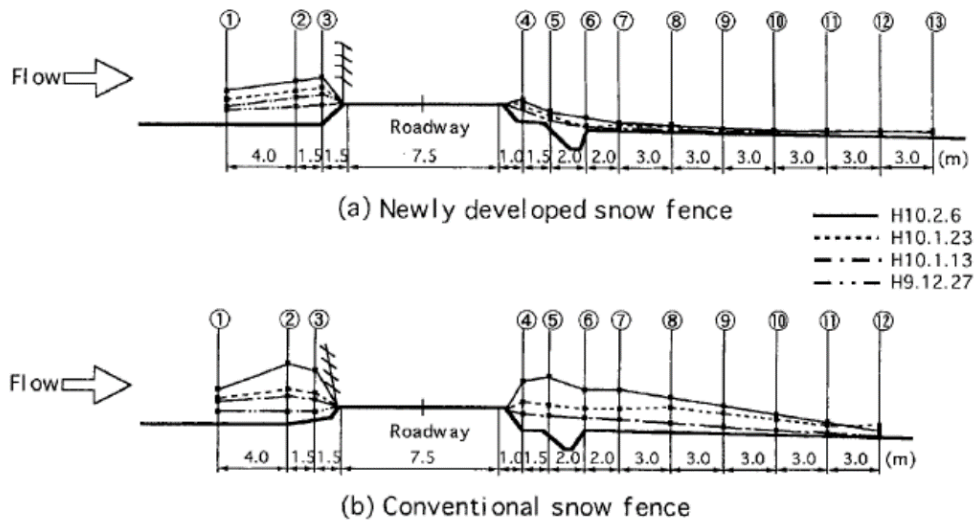Part of the present study, several simulations were performed for a road containing a ditch, which is a very common configuration for Iowa roads. One should mention that most of the studies available in the literature showed that blow off fences can work very well for narrower roads without a ditch in between the lanes that divides the traffic in opposite directions. Several ideas were tried starting with the conventional solution of placing a blow-off fence on the road side. The second idea was to place two identical blow-off fences one on the road side toward the wind is blowing and one on the side of the other lanes, close to the end of the ditch. A third design consisted of using a different design for the downstream blow-off fence that has a higher capacity of advecting flow toward the surface of the road lanes (see cases BT7 and BT8). Finally another idea was to propose a hybrid solution containing both a standard snow fence situated away from the road and two blow-off fences situated in the immediate vicinity of the lanes. Following the work of Sakamoto and Haniu (2001), two types of plates were considered: flat plates and deformed (circular) plates. The standard design used in the present simulations is also based on their work. For the modified blow-off fence design that was supposed to increase the blow off capacity of the fence compared to the standard design, the bottom gap was reduced from 1.2 m to 0.8 m and the number of plates was increased from 4 to 5. A third parameter that was varied was the angle of the plate for the circular plate design (0.62 m in case BT4 vs. 0.95 m in case BT5). The total fence height was larger in cases BT7 and BT8 by about 20% compared to the other cases due to the

100

increase in the number of snow plates. Table 4 present an overview of the geometrical parameters of the blow-off fences used in the eight design set ups that were considered.

Table 4. Matrix of the simulations performed for blow-off type (BT) snow fences. Fence height is 2.8m. Single = BT fence at the edge of the road, Double = BT fence at both edges of the road and Double+ = BT fence at both edges of the road with a regular fence on one side. Both flat plates and deformed (circular) plates were considered in the study.

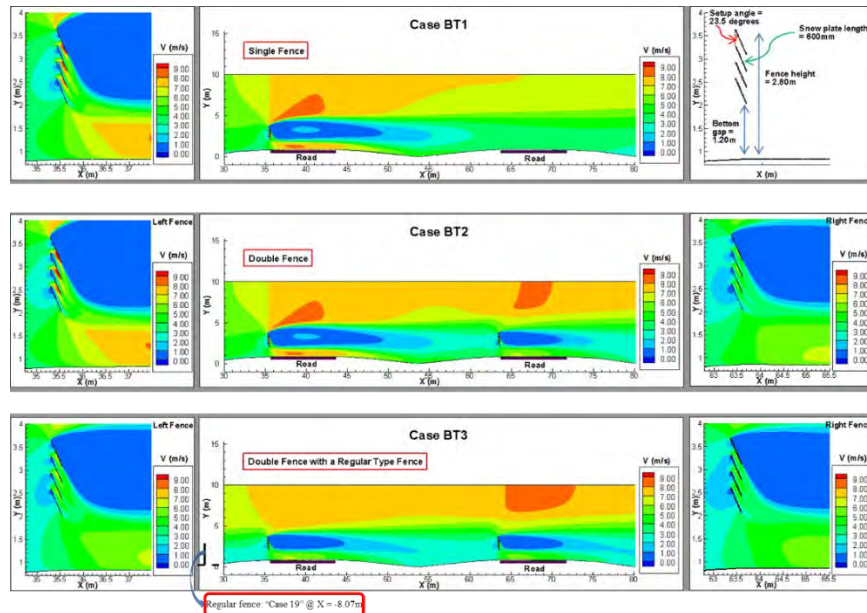| Case	Single/Double	Snow Plate type	Snow plate length (mm)	Setup angle (degrees)	No. of Snowplates	Bottom gap (m)	Fencing ht. (m)
BT1	Single						
BT2	Double	Flat	600	23.5			
BT3	Double+				4	1.2	1.6
BT4	Single		620				
BT5	Single						
BT6	Double	Circular	950	35			
BT7	Double				5	0.81	1.99
BT8	Double+						

Figure 103. Distribution of velocity magnitude on the downwind side of the blow-off snow fence for designs BT1, BT2 and BT3 (flat plates).
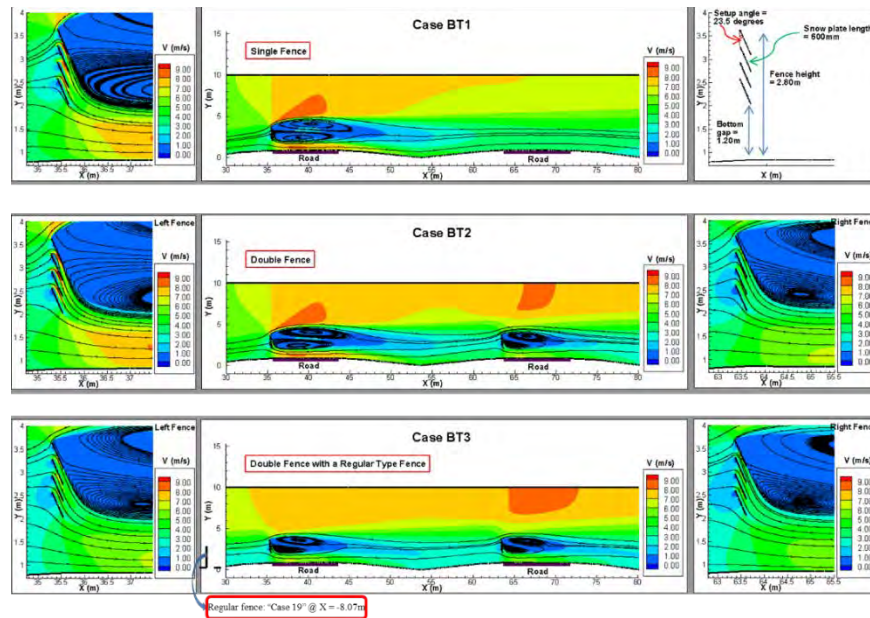
Figure 104. 2D Streamline patterns plot superimposed on the distribution of velocity magnitude for designs BT1, BT2 and BT3 (flat plates).

In the case of flat plates (Figures 103, 104), simulation results clearly show that design BT1 containing cannot protect the lanes situated on the other side of the ditch against snow deposition. This is because the spatial extent of the region of high velocity magnitude near the road surface does not penetrate over the lanes situated on the other side of the ditch. On the other hand the region of high velocity magnitude covers all the surface of the lanes situated close to the fence. This suggests that the fence offers good protection against snow drifting for those lanes. The second design (BT2) contains another blow-off fence mounted on the extremity if the lanes situated on the other side of the ditch. The design of the two fences is identical. The second fence also induces the formation of a region of high velocity magnitude near the lanes situated on the other side of the ditch. However, the spatial extent and velocity magnitudes inside this region are much lower than those recorded for the lanes situated on the opposite side of the ditch. One idea to fix this problem will be to modify the design of the second blow-off fence to increase the air flow speed close to the road by reducing the bottom gap and maybe decreasing the angle of the plates with the vertical. This option will be considered later in the context of blow off fences with circular plates. Another option (case BT3), that should be considered for cases with wider right of ways, is to use both a regular (plastic) fence situated on the upwind side of the road supplemented by two blow-off fences in the immediate vicinity of the lanes with traffic in the two opposite directions. In this case the regular fence will retain an important quantity of snow. However, for very large snow events the presence of the blow-off fences should provide additional protection against snow drifting, as the remaining snow that would normally deposit on the road will be advected away from the lanes by the airflow induced by the blow-off fences. One of the positive features of the velocity magnitude distribution in case BT3 is that the characteristics of the region of velocity acceleration near the surface of the lanes containing opposite traffic are very similar, so the use of two blow-off fences of identical design is fully justified in the present case.
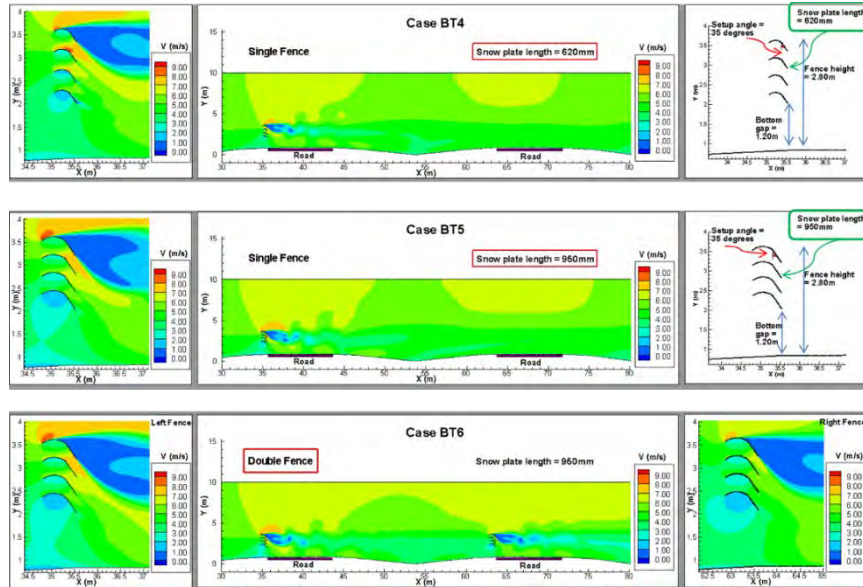
102

Figure 105. Distribution of velocity magnitude on the downwind side of the blow-off snow fence
for designs BT4, BT5 and BT6 (circular plates).

Figure 106. 2D Streamline patterns plot superimposed on the distribution of velocity magnitude
for designs BT4, BT5 and BT6 (circular plates).

Cases BT4, BT5 and BT6 (Figures 107, 108) are identical to cases BT1, BT2 and BT3 (Figures 105, 106) except that the blow-off fences contain circular plates rather than flat plates. Overall, the same qualitative differences are observed among the three designs. The velocity magnitude inside the region of high velocity amplification near the lane surface is smaller for circular plates compared to flat plates. To increase the blow-off capacity of fences containing circular plates, one can further decrease the bottom gap. Interestingly, the effect of the second blow-off fence in case BT5 is pretty small in terms of creating a region of high velocity magnitude close to the lanes with traffic in opposite direction. So, at the minimum the design of the second blow off fence should be

103

modified. Finally, the hybrid design containing both a standard fence and two blow-off fences appear to produce similar velocity and streamline patterns over the lanes containing traffic in opposite direction. The only possible concern is the relatively small amplification of the velocity over the lane surface.

Designs BT5 and BT6 were further modified by including a second blow-off fence of modified design, such that the capacity of the second blow off fence to increase the velocity near the lane surface situated next to it is larger than that of the first blow-off fence. To achieve this, the bottom gap of the second blow-off fence was decreased and the number of blades was increased from 4 to 5. Comparison of results for cases BT5 and BT7 in Figures 107, 108, 109 and 110 show that the airflow field next to the two blow-off fences of different design is now very similar. Meanwhile, it is still possible that the airflow created by the two blow-off fences is too weak near the lane surface, but this problem can be fixed by further decreasing the bottom gap or increasing the length of the blades. Comparison of results for cases where an additional standard fence was present (cases BT6 and BT8) also shows the airflow around the two blow-off fences of different design is very similar.

This analysis shows how information from numerical simulations can be used to guide the design of blow-off fences. Of course, to be able to make final design recommendations one needs to test the candidates for best design in the field under close to identical conditions, similar to the procedure followed for plastic snow fences.

Figure 107. Distribution of velocity magnitude on the downwind side of the blow-off snow fence for designs BT7 and BT8 (circular plates, the designs of the upstream and downstream fences are different).
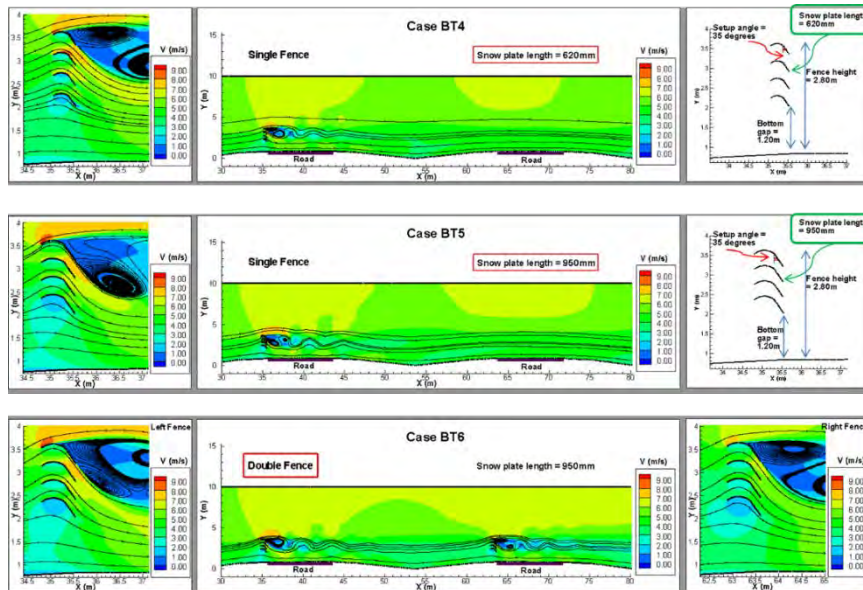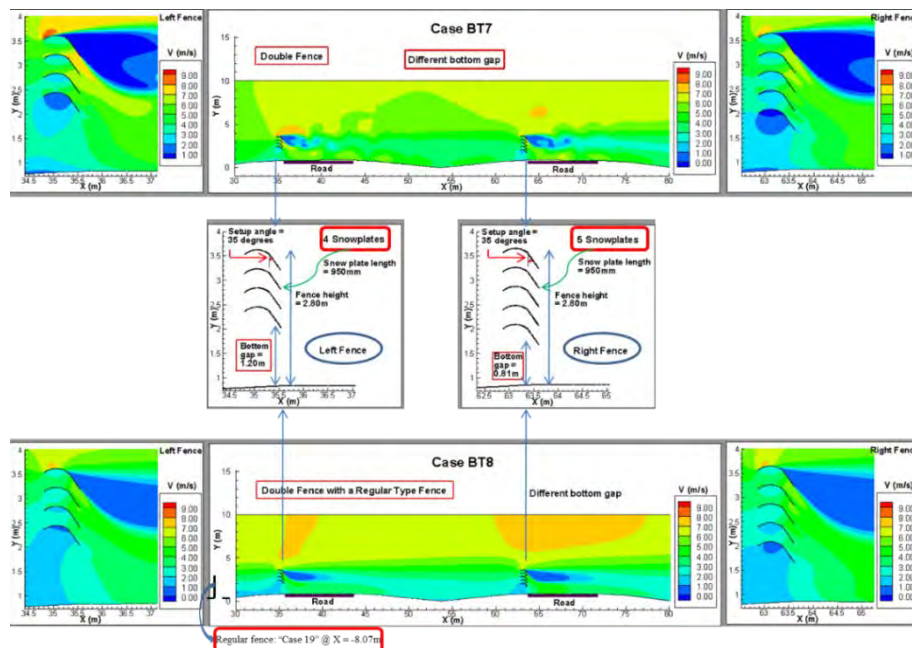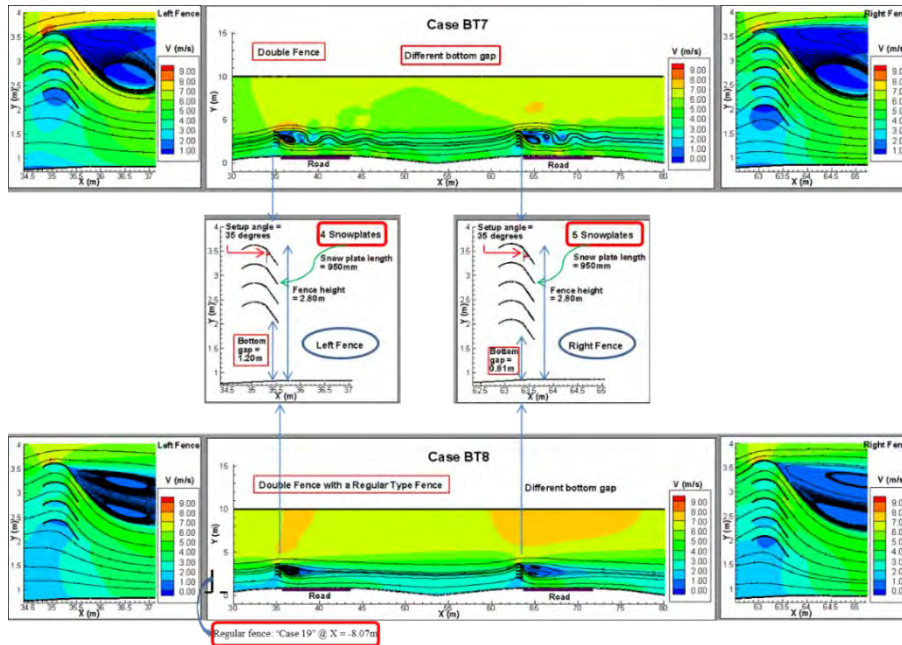
Figure 108. 2D Streamline patterns plot superimposed on the distribution of velocity magnitude for designs BT7 and BT8 (circular plates, the designs of the upstream and downstream fences are different).

5.4. ESTIMATION OF SNOW RELOCATION COEFFICIENT

5.4.1. Introduction

Currently, the Iowa DOT design guidelines for controlling snowdrifts and reducing the concentration of snow in air are based on the studies conducted by Tabler (1991, 1994, and 2003). These studies are considered "the best available information" in the area of mitigation of snow drift and represent the foundation for the Wyoming Snow Drift Profiles software (Tabler, 2006) that is the main design tool used in the IDOT. The analytical relationships developed in these studies include several empirical coefficients that were obtained empirically in Wyoming (e.g., relocation coefficient, snow-fall equivalent, maximum transport distance), hence they are of unknown accuracy when used elsewhere. The snow relocation coefficient (SRC) is the most complicated to estimate parameter while being a major factor in the outcome of the snow fence design software.

The SRC is defined as the percentage of fallen snow that will be relocated from the upwind fetch area. This value is thought to vary from 0.75 for barren windy locations (e.g., Wyoming) to 0.15 for locations with dense tall vegetation (Tabler, 2006). Studies in Siberia and Wyoming show that even on flat areas with low-growing vegetation the SRC seldom exceeds 0.7 over a winter. In the northeastern US, SRC typically ranges from 0.2 to 0.3. Given its importance and its considerable variation, the SRC evaluation requires technical assistance (provided by WYDOT Winter Services for Wyoming conditions). This type of guidance is not currently available for the Iowa conditions. Moreover, the SRC estimation is dependent on the snowfall (depth) records at a specific site. The snowfall data, as currently provided for Iowa from such sources as Iowa MESONET

(http://mesonet.agron.iastate.edu) and NOAA (http://www.nohrsc.noaa.gov), are not accurate. During the conduct of this study, there were several inferences drawn on the issues of estimation of the snow relocation coefficient that require attention. They are discussed below to provide a record of issues that requires future research.

5.4.2. Estimation of snow relocation coefficient using Tabler (1994) approach

In order to substantiate the importance of the snow relocation coefficient and to point to its weaknesses for being used in other than Wyoming conditions, a summary of the computation leading to its calculation are reproduced here verbatim from Tabler (2006), p. 37.

The relocated snow, $S_{rwe,}$, is defined as that portion of the winter's snowfall relocated by the wind, and excludes snow retained by vegetation and topographic features, or snow that hardens or melts in place (see Figure 109). The relocated snow water-equivalent is determined using equation 8 of Tabler 1994:

$$S_{rwe} = \frac{Q_{0-5}}{500\,T} \qquad (8)$$

where, Q_{0-5} is estimated from equation (9) below, T is the maximum transport distance (in meters). Usually T = 3000m (10,000 ft.) - established for Wyoming conditions. The snow transport rate, Q_{0-5}, is provided by

$$Q_{0-5} = \frac{U_{10}{}^{3.8}}{233847} \qquad (9)$$

where, U_{10} = wind speed is in m/s, is the dominant wind for the areas averaged for the winter season.
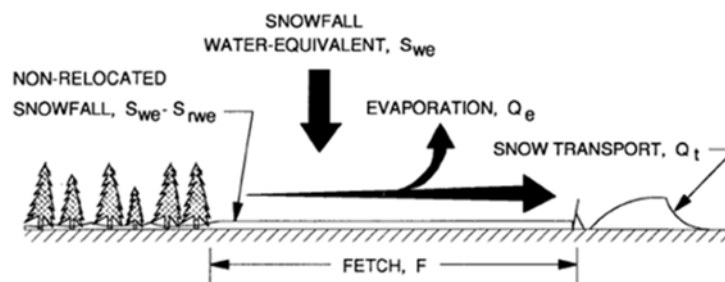

Figure 109. Diagram of the transport distance concept used to estimate evaporation loss from wind-transported snow (Tabler, 1975a).

A reasonable estimate for water-equivalent according to (Tabler, Berg et al. 1990) is

$$S_{we} = (snowfall\ depth) / 10 \qquad (10)$$

The snow relocation coefficient, *SRC*, is defined as:

$$SRC = \frac{S_{rwe}}{S_{we}}$$
(11)

As can be noted from the inspection of the relationships above, there are multiple empirical coefficients that have been established from experiments conducted in Wyoming conditions. Currently, there are no Midwestern equivalents for these parameters. Another major challenge in defining the relocation coefficient is that the Snowfall depth involved in Equation (10). This variable is typically provided by conventional meteorological stations but it is prone to considerable measurement errors.

Actually, there are few stations throughout Midwest where this important variable is measured accurately because of the challenges in the measurement process. The typical protocols used at the conventional meteorological stations (90% of the US stations) for estimation of the snow fall and snow depth are summarized for completeness below:

1. Snowfall measurement (see Figure 110):
- Measurement of new (fresh) snow deposit at the same location daily
- The depth is obtained using a tape. - Measured at the same time daily
- The white board is cleaned after each measurement.

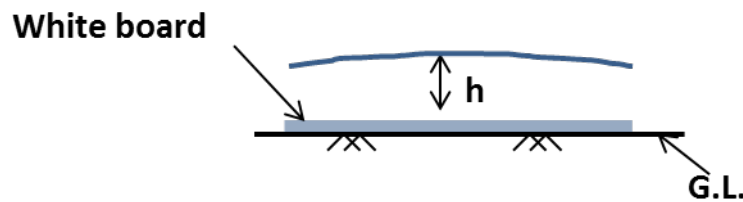Figure 110. Snow fall, h = measured height of snow deposited in 24 hours at a fixed location.

2. Snow depth measurements (see Figure 111):
- Measurement of total snow deposit at the same locations daily over aa 10 m span
- The depth is obtained using a tape measurement of snow deposited directly on the ground
- Measured at the same time daily
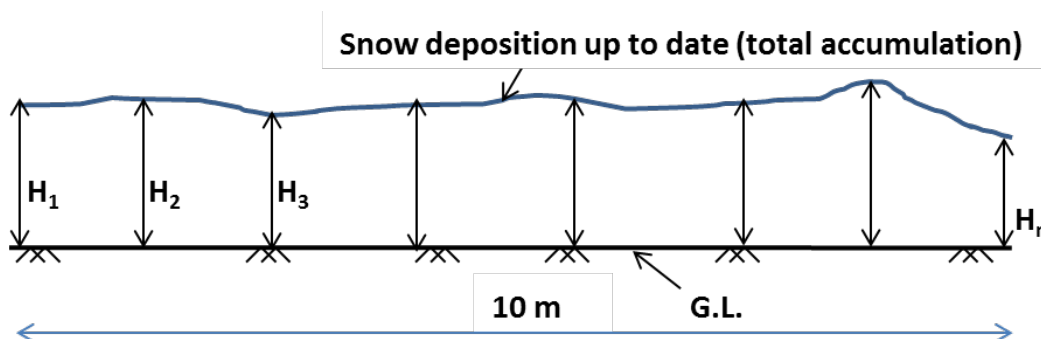- Snow depth is the average of the measured heights of snow deposit at n locations.

Figure 111. Snow depth, $H = (H_1+_2+H_3+……..+H_n)/n$.

The research team contacted data managers and specialists at Midwest meteorological stations for consultation and advice on how to best determine the snow fall rates. Excerpts from their statements are provided bellows:

- Dr. Jim Angel, State Climatologist (www.isws.illinois.edu/atmos/statecli/). The snow data available from the internet (see next) are not usable as the measurement protocols does not account for the effect of wind blowing the snow at the time of measurement. In other words the drift velocity biases the reported measurements.
- Dr. Tim Szeligo and Greg Fall (National Operational Hydrologic Remote Sensing Center, Chanhassen, MN) – no reliable measurements on snowfall as 90% are using open platforms for snow fall measurements,
- Greg Fall, Programmer NOHRSC *(http://www.nohrsc.noaa.gov/directory/bios/bio_gf.html)*. The snowfall data provided on the NOHRSC website cannot be assimilated accurately for snow-drift estimation purposes as it is modeled (not measured) using other variable forecasts. He also notified us that there are no snow course site in Iowa and surrounding states: *http://www.wcc.nrcs.usda.gov/snowcourse/snow-course-sites.html.*
- Dr. Tom Sauer – National Laboratory for Agriculture and Environment), ISU. (The laboratory measure directly the liquid water equivalent as measured by a heated precipitation gauge, but the snow collection is also problematic as the wind effect is not included in the measurements.

5.4.3. Estimation of the snow relocation coefficient for the experimental site

The lack of reliable method for measurement of the snow depth impedes the accurate estimation of the relocation coefficient. Most often, default coefficients prescribed by the guidelines are used as input for the design software. A new alternative was tested in the present study to evaluate the relocation coefficient. Specifically, we combined snow fall or snow depth data with direct measurements acquired at the experimental site. An area located upwind of the snow fence was selected for estimation of the relocation coefficient, as illustrated in Figure 112.

Figure 112. View of cameras used to record images for the experiment.

The snow relocation coefficient, *SRC*, is determined based on the following equation:

$$SRC = \quad (A-B)/A \tag{12}$$

where, *A* is the snow fall as recorded by *http://mesonet.agron.iastate.edu/request/coop/fe.phtml*), and *B* is the snow depth estimated using measurements at the site.

5.4.3.1. Estimation of the snow depth at the experimental site

We developed two protocols for conducting the field measurements for acquiring the snow depth: Protocol 1 – using direct measurements during field trips (see Figure 113); Protocol 2 using recorded images from web-camera and photogrammetry (Figure 114)

(a)

(b)

Figure 113. Protocol 1 for snow depth estimation: a) the method requires field measurements (GPS or other direct measurements); b) view of the experimental site on December 11, 2013 (relocation coefficient = 0.54).

(a)

(b)

Figure 114. Protocol 2 for snow depth estimation: a) images acquired for processing: b) view of the experimental site on December 12, 2013 (relocation coefficient = 0.71).

5.4.3.2. Snow fall data from meteorological stations

Snow data were used from available two sources: Mesonet and NOAA. Example of sample data from Mesonet and NOAA are displayed in Table 5 and 6 respectively. We compared the snowfall data that was available from both sources and found that the snow data were same for the two sources. The snow relocation coefficients calculated using equation 12 for two snow storm events are provided in Table 7.

Time series of relocation coefficients using the acquired snow depth data at the experimental site are provided in Figure 115. It can be noticed from the figure that the relocation coefficient varies

from 0.25 to 0.75 that. Given that the default value typically used in the design is 0.5, we might conclude that the estimation is realistic. However, the method based on equation 12, similarly to Tabler's (2006) method, assumes that the wind at any time is invariable acting along the dominant wind direction established as an annual average. Figure 116 clearly shows that this assumption does not hold and the wind varies considerably in magnitude and direction during a snow storm from day to day, and even from hour to hour. Figure 117 illustrates long-term series of the relocation coefficient over several winter months. Given that most of the snow accumulation occurs during snow storm, it is obvious that these methods are very crude approximations of the actual field conditions. However, in the absence of other relocation coefficient estimation means the study author proposes that the developed method can be used surrogate. New protocol for improved accuracy estimation of the relocation coefficient is provided in the next section.

Table 5. Sample data from source 1 (Mesonet) for December 9-23, 2013.
Source: http://mesonet.agron.iastate.edu/request/coop/fe.phtml.

station	station_name	day	snow fall (in)
IA4142	IOWA-FALLS	12/9/2013	0
IA4142	IOWA-FALLS	12/10/2013	0
IA4142	IOWA-FALLS	12/11/2013	3
IA4142	IOWA-FALLS	12/12/2013	0
IA4142	IOWA-FALLS	12/13/2013	0
IA4142	IOWA-FALLS	12/14/2013	0
IA4142	IOWA-FALLS	12/15/2013	0
IA4142	IOWA-FALLS	12/16/2013	0
IA4142	IOWA-FALLS	12/17/2013	0
IA4142	IOWA-FALLS	12/18/2013	0
IA4142	IOWA-FALLS	12/19/2013	0
IA4142	IOWA-FALLS	12/20/2013	0
IA4142	IOWA-FALLS	12/21/2013	0
IA4142	IOWA-FALLS	12/22/2013	2.5
IA4142	IOWA-FALLS	12/23/2013	0

Table 6. Sample data from source 2 (NOAA) for December 11, 2013.
Source: http://www.nohrsc.noaa.gov/interactive/html/.

Table 7. Summary examples.

Snow event	Avg. wind speed, U (m/s)	Snow transport, Q (kg/m)	S_{rwe} (in.)	Snowfall (in.)	S_{we} (in.)	*SRC*
Date	(data from website)	(equation 9)	(equation 8)	(data from website)	(equation 10)	(equation 11)
12/11/2013	18605.4	146.5	0.00384	3	0.3	0.013
12/22/2013	18610.3	351.8	0.00923	2.5	0.25	0.037
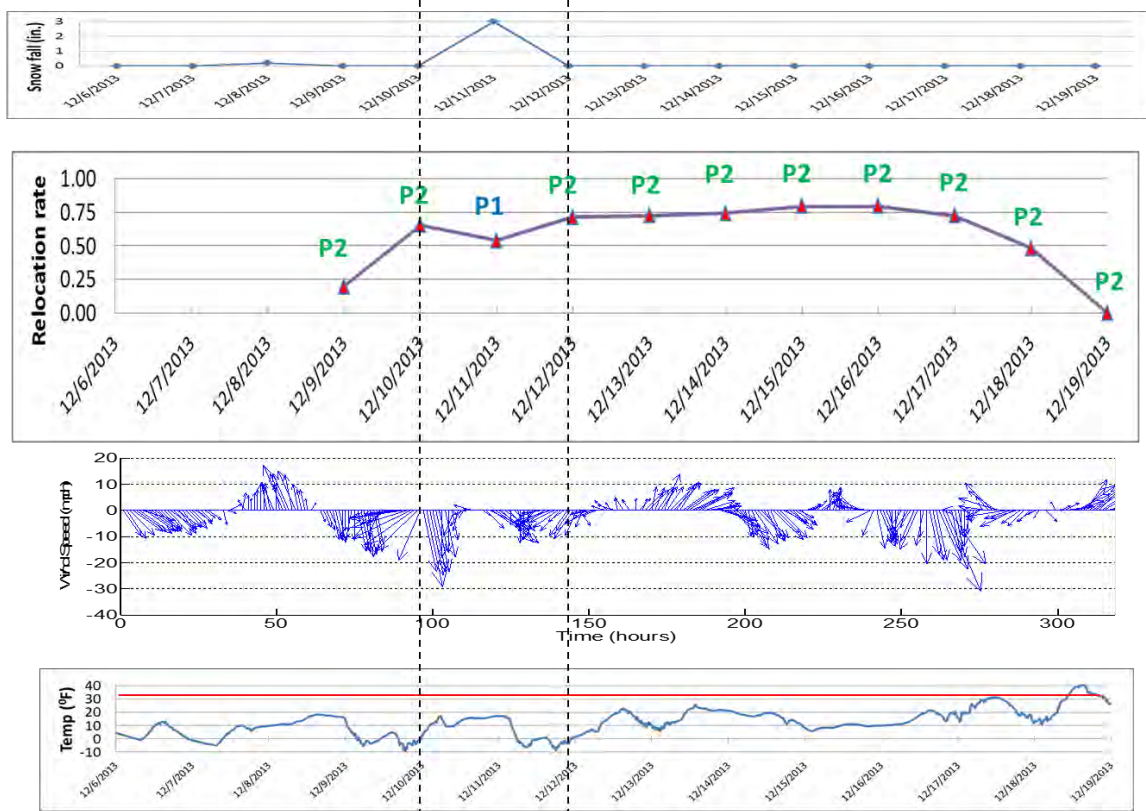
Figure 115. Sample estimation of relocation coefficient using protocols 1 and protocol 2
(December 6-19, 2013).
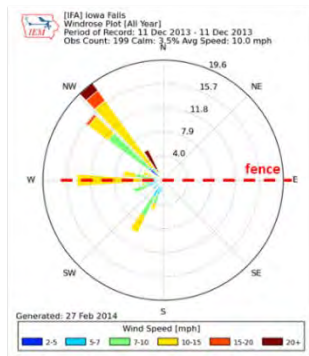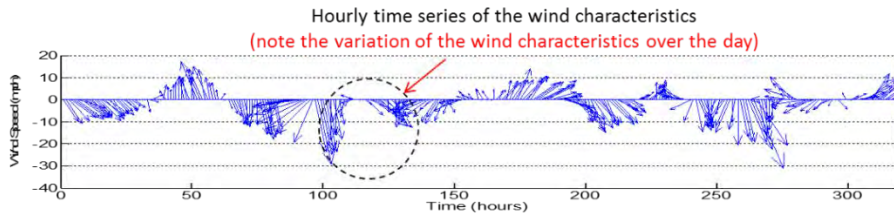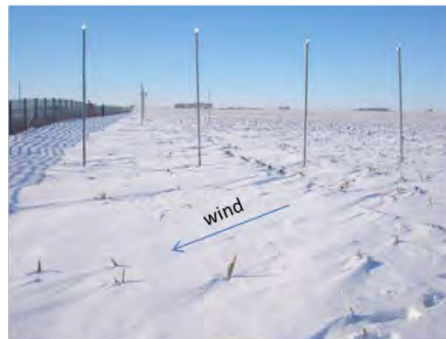
Figure 116. Variation of the wind direction during the December 11, 2013 snow storm.
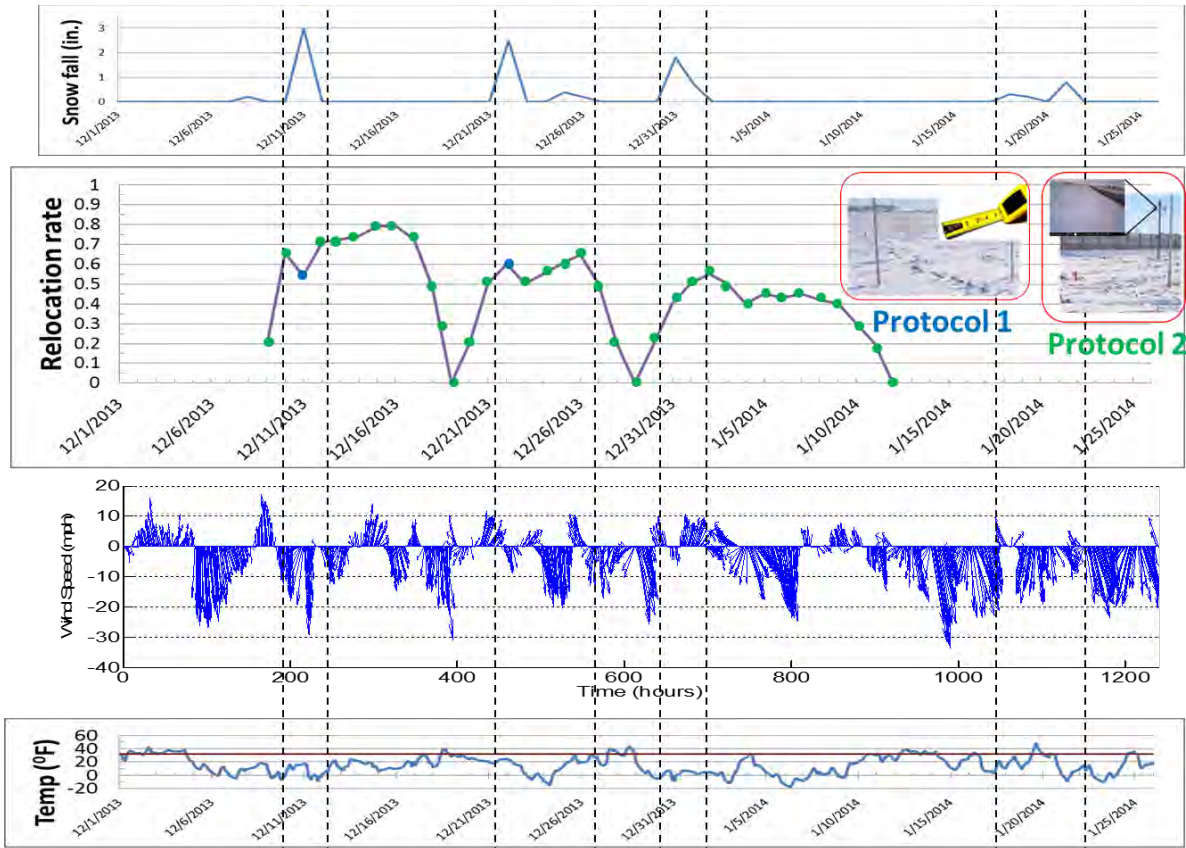
Figure 117. Relation of relocation coefficient with precipitation, wind velocity and temperature for extended period (December 1, 2013 – January 26, 2014).

5.4.4. Proposed method for estimation of the snow fall

The previous discussion lead to the conclusion that snow fall or snow depth data available from conventional meteorological stations are affected by considerable errors because of the measurement errors. In particular, these methods do not account for the effect of wind blowing the snow at the time of measurement of this quantity. Consequently, we cannot reliable use available snow data to calculate snow relocation coefficient. The study research team conducted some preliminary tests to test an alternative measurement approach for the quantification of the snow fall variable. The method is based on an image-based principle and is briefly summarized below.

The image-based method proposed as an alternative measurements method for snow fall rate estimation provides whole-field velocity measurements over large spatial coverage. The technique, labeled Large-scale Particle Image Velocimetry (LSPIV) has been extensively used for measurements in laboratory and field conditions (Muste et al., 2008). In essence, LSPIV acquires images of the snow fall at the time when it occurs using conventional video cameras (see Figure 118). The technique is portable and can be quickly deployed at the site of the measurement. It requires a background screen to provide contrast to the image and setting the camera at a distance from the screen that allows identification of individual snowflakes during their fall. The recorded

114

images are then processed using specialized software to provide vectors associated to each snowflake in the recorded images. The image processing software is also equipped with means to determine the size for each snow particle. Using the obtained vector field and the particle sizes, fluxes or rate of snow fall (as volumes or weight) can be determined through spatial-temporal averaging of the instantaneous results.

These measurement technique used in conjunction with the other protocols for monitoring the growth of snow deposits at snow fences will add depth and breadth to a comprehensive method to estimate the snow flux budget with consideration of all the transport process components. For this purpose, the snowfall and the volume of snow that is relocated will be directly measured using the technique developed through section 5.4.3.1. The amount of snow deposited upwind and downwind the fence will estimated as volumes using photogrammetry and direct topographic surveys. The snow fall budget will be completed using a flux calculation protocols that will results in estimates of the residual snow drifting over the road.

a) Video-recording of snowfall

b) Velocity vectors produced with LSPIV

c) Image based sizing

Measurement outcomes:
1. Velocity vectors (instantaneous and averaged)
2. Sizing and concentration of snow
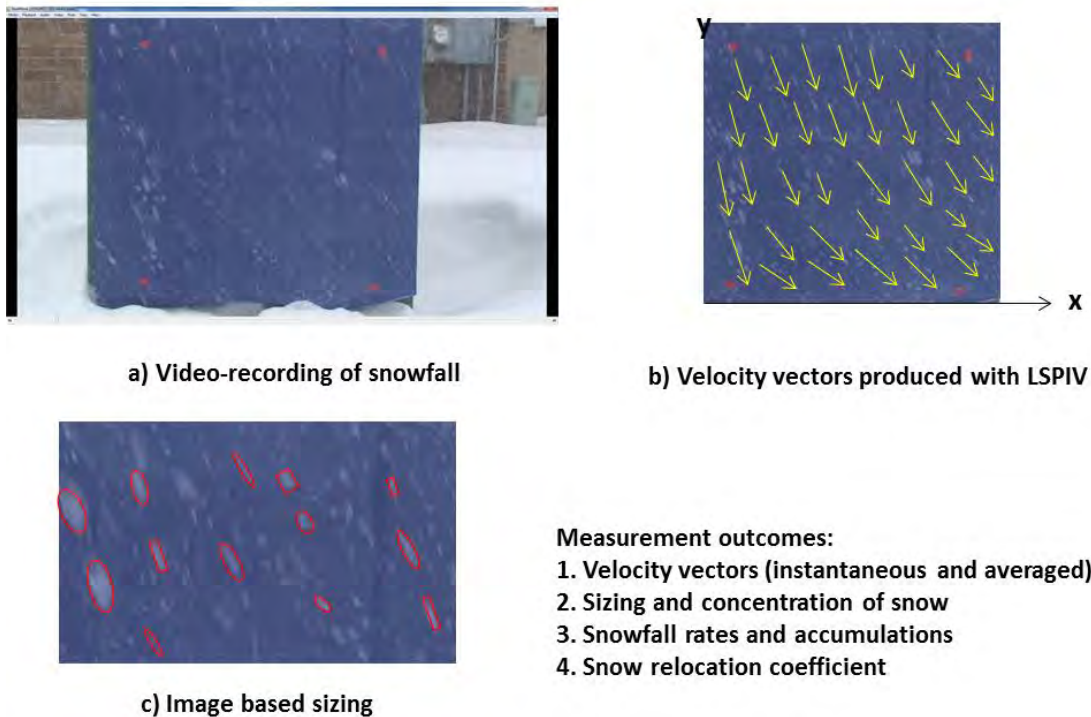3. Snowfall rates and accumulations
4. Snow relocation coefficient

Figure 118. Image velocimetry applied to snowfall: a) video-recordings are taken in-situ over an area large enough to provide reliable velocity fields; b) LSPIV procedures are used in conjunction with the recordings to obtain velocity fields; c) sizing of the snow particles is obtained with customized protocols; d) outcomes of the measurements.

6. CONCLUSIONS AND RECOMENDATIONS

A methodology based on field monitoring of snow fences, field measurements of snow deposit profiles and numerical simulations was developed to help improve the design of snow fences. Of critical importance for successfully applying the proposed methodology is that a sufficiently long field test side is available, where several fence designs can be tested under close to identical conditions, and that accurate methods are used to determine the snow deposition profiles after major snow events at the site.

Most of the focus of the present study was on lightweight snow fences which are inexpensive to deploy and a very common type of snow fences, especially in the U.S. Midwest. The standard design for this type of fences recommends fence porosity close to 50% and that the bottom gap is about 10% of the fence height.

The present study investigated the effectiveness of similar fences with a lower porosity because of the possibility that such fences retain more snow and/or the length of the region of significant snow deposit on the downwind side of the fence is reduced. If that is indeed the case, then lower porosity fences can be used for effective protection against snow drifting in regions with narrower rights of way. As previous studies have shown that the air flow fields past snow fences do not contain a recirculation region for fences with a porosity larger than 30%, we focused on proposing an optimum design for fences with P=30%. Obviously, the optimum design for fences of lower porosity should involve using a large bottom gap relative to the fence height. This is because as the fence porosity decreases, the conditions for snow deposition immediately downstream of the fence increase. This leads to a rapid filling with snow of the bottom gap and eventually to a loss in the capacity of the snow fence to protect the road against snow drifting.

The field monitoring program conducted over the first year confirmed that the optimum design of plastic snow fences with a porosity of 50% has a fence bottom gap which is about 10% of the fence height. It also allowed understanding how the shape of the snow deposit changes as the ratio G/H increases. Numerical simulations were used to understand the main characteristics of the mean flow past the fence and how these characteristics vary with the fence height, fence porosity and bottom gap. It was found that the fence with P=50% and G/H=0.08 induced the formation of an elongated and fairly thick region of small velocity magnitude close to the ground, which favors snow deposition. For the other two designs with P=50%, the streamwise extent and shape of this region were different. Similar simulations were undertaken for snow fences with P=30%. Two of the designs that were found to be good candidates for optimum design based on the distribution of the mean velocity magnitude were tested during the next winter along with the optimum design for fences with P=50%. To make easier to estimate the efficiency of the different designs, all three designs tested in the field during the second winter had the same height but different bottom gaps.

While the volume of the snow deposit retained by the three designs was found to be comparable, the length of the snow deposit was reduced by about 30% for the two fence designs with P=30% compared to the optimum fence design with P=50%. Moreover, the snow level at the location of the fence never exceeded the height of the bottom gap. This means that the fences with P=30% will continue to work well even under more severe snow events than the peak snow event recorded during the second winter. By contrast, the bottom gap was all filled with snow for the optimum

design for fences with P=50%. The optimum ratio between the bottom gap and total fence height for fences with P=30% was found to be 0.2-0.25. As expected, this value is significantly larger than the one recommended to maximize efficiency of fences with P=50%. Moreover, monitoring done over a subsequent winter season, confirmed that the design with P=30% and G/H=0.25 continue to be effective even for more severe snow events containing conventional snow as well as for events in which the snow storm was preceded by icy rain. The P=50% design totally failed for the latter conditions.

Besides formulating design recommendations for plastic snow fences with P=30%, a main finding of the present study is that properly designed fences with P=30% can be as efficient as fences with P=50% of same height, but they can be placed closer to the road. This means such lower-porosity fences are a better option to protect roadways against snow drifting in regions with narrow right of ways. Though not tested in the field, the present study showed that solutions containing blow-off snow fences can be a way to address the problem of severe snow drifting in regions with narrow right of ways. In the case where the traffic lanes in opposite directions are separated by a ditch, the present study found that blow-off fences should be installed on the downwind side of the traffic lanes in opposite direction. So two blow-off fences should be installed and to maximize their efficiency the design of the downstream blow off fence should be modified (lower bottom gap, increased number of blades). The study also found that using standard snow fences whose position is not vertical does not result in an increase in the performance of these fences.

The field monitoring performed at a site containing various types of vegetation showed that the use of living snow fences appears to be a very effective for a wide range of vegetation maturity. Quantification of the performance of this type of snow fences requires more research. Another outcome of the study was the development of a combination of data resources for estimation of the meteorological conditions at the sites where field monitoring of snow fences was undertaken.

In the present implementation of our methodology to monitor performance of snow fences, the measurements of the snow deposit were conducted using a GPS-based real-time kinematic survey. However, other imaging techniques based on LiDAR data collection (Tsubaki and Fujita, 2010), Large-Scale Particle Image Velocimetry concepts (Fujita and Kunita, 2011; Hauet et al., 2008 and 2009; Muste et al., 2009 and 2011; Ettema, 2011) or 3-D close range photogrammetry (e.g., Yakar et al., 2010) can be used in the future. In fact, all these methods were tested and implemented as part of the present study. Some of these techniques can provide the continuous evolution of the snow deposit in time, which can subsequently be used for a more detailed evaluation of the snow fence performance. The approach developed in this study to test and improve the design of snow fences can be applied to other types of structural snow fences (e.g., latch fences containing vertical elements) and can be extended for living snow fences. The present method is particularly well suited to optimize the design of living fences consisting of rows of corn for which the relative position of the corn stems, their diameter and arrangement is fairly regular, which allows an accurate estimation of the porosity.

The design of snow fences using the current procedures (e.g., using WYDOT Snow Drift Profiler) requires parameter that are related to snow volume estimates (e.g., snow relocation coefficient). Moreover, the assessment of the efficiency of the built snow fences is relevant if the snow volumes deposited in the wake of snow fence can be accurately monitored during successive storms.

Despite its critical role in design and monitoring of snow fences, the mapping of the snow volumes using conventional tools (e.g., total station or GPS surveys) is a difficult and tedious process mostly due to the adversity of the measurement environment. The emergence of the non-intrusive techniques shows big progress for facilitating this type of in-situ measurements (see Muste et al., 2009 and 2011; Basnet and Ettema, 2011). A strong candidate from this family of techniques is CRP if some precautionary measures are considered.

In the second part of this study, we discussed the benefits and limitations of CRP implementation for tracking snow volumes accumulated downwind road fences. To the knowledge of these authors this method was not previously tested in field conditions. Two protocols for conducting the measurements were established in this study. The first one requires assistance from alternative surveying measurements. The second one is accomplished using only remote measurements (see Table 1). The comparison of simultaneous measurements with the two protocols confirmed the possibility of using a measurement procedure that does not require deployment of personnel in the field. The results obtained in the study lead to the conclusion that CRP technique has unique capabilities to map snow elevations over large areas using only a pair of camera that is automatically operated. The method can be used continuously allowing tracking dynamic snow volume remotely that it is difficult, or even impossible, to be obtained with alternative mapping means. Among the CRP limitations are the lack of surface texture and color gradients on the surface of the fresh snow fall accumulations. These limitations can, up to a certain degree, be overcome using an increased number of ground control points, especially when CRP is used for dynamic snow deposit tracking. The CRP implementation protocols optimized as described in this study led to differences of not more than 16% compared to conventional (and undoubtedly more accurate) intrusive measurement approaches.

The new imaging technology offers the unique ability to simultaneously collect snow landscape panoramas and details with time steps commensurate with the in-situ development of the snow transport processes. Overall, it can be concluded that CRP is a promising technique that can be considerably perfected by adding new means to overcome the current limitations. The CRP can be used as stand-alone technique for dynamically mapping snow drifting in the presence of natural or artificial obstacles that retain the snow. The technique is especially suitable in assisting the snow fence design, an area that is guided by semi-empirical analytical formulas established for specific sites. This information is not readily transferable for other fence construction sites therefore studies as the one reported in this paper would greatly contribute to test and correct the existing methodologies.

Attempts to estimate the snow relocation coefficient (SRC) needed by the Wyoming Snow Drift Profile software using standard semi-empirical formulas or generally-available meteorological data were not successful. In particular, we demonstrated that the procedure given in Tabler (2006) to estimate the SRC gave unphysical results when applied to the test sites monitored as part of the present study. A main recommendation for future work is the development of an image-based method to evaluate the transport processes in the snow budget and measure the SRC directly in the field under various conditions. Snow drifting and transport past the snow fence will be quantified with high resolution using a combination of GPS technology and an image-based (large-scale particle image velocity, LSPIV), which has been extensively used for measurements in laboratory and field conditions (Muste et al., 2008, 2009, 2011). By providing information on the velocities

and sizes of snow particles, LSPIV and 3-D photogrammetry allow components of snow transport—flux of relocated snow, snow retention upwind/downwind of the fence, and drifting—to be measured directly and the snow budget to be evaluated. The experimental approach will also allow the temporal evolution of the volume of snow retained by a fence to be measured so that the efficiency of a design solution can be confirmed over a whole winter season.

REFERENCES

Aerotechnics. http://www.aerotechnic.com.

Alhajraf, S. (2004). "Computational fluid dynamic modeling of drifting particles at porous fences." *Environmental Modeling & Software,* 19, 163-170.

Anno, Y. (1986). "Snow deflector built at the edge of a road cut." *Cold Regions Science and Technology,* 12, 121-129.

Baldi, P., Genni, N., Fabris, M., and Zanuta, A. (2008). "Kinematics of a landslide derived from archival photogrammetry and GPS data." *Geomorphology*, 102, 435-444.

Basnet, K. and Ettema, R. (2011). "A large-scale particle image velocimetry for resolving unsteady flow features at cylinders." *Proc., 34th World Congress of the Int. Association for Hydro-Environment Research and Engineering*: 33rd Hydrology and Water Resources Symp. and 10th Conf. on Hydraulics in Water Engineering, Engineers Australia, Barton ACT, Australia, 3378–3387.

Basnet, K., Constantinescu, G., Muste, M., and Ho, H. (2014). "Method to assess efficiency and improve design of snow fences." *Journal of Engineering Mechanics,* 04014136, doi: 10.1061/(ASCE)EM.1943-7889.0000871.

Castro, I.P. (1971). "Wake characteristics of two-dimensional perforated plates normal to an air-stream." *Journal of Fluid Mechanics,* 46, 599-609.

Constantinescu, S.G., A. Bhatti, and T. Tokyay (2008), "A numerical study of wind loads on large highway sign structures." *SEI 2008 Structures Congress,* Vancouver, Canada, April 2008.

Constantinescu, G., Koken, M., and Zeng, J. (2011), "The structure of turbulent flow in an open channel bend of strong curvature with deformed bed: insight provided by an eddy resolving numerical simulation." *Water Resources Research,* 47, W05515, doi:10.1029/2010WR010114

Cooper, M.A.R. and Robson, S. (1996). Theory of Close Range Photogrammetry, Close Range Photogrammetry and Machine Vision, pp. 9-51.

Dong, Z., Luo, W., Qian, G., and Wang, H. (2007). "A wind tunnel simulation of the mean velocity fields behind upright porous fences." *Agricultural and Forest Meteorology,* 146, 82-93.

Dong, Z., Luo, W., Qian, G., Lu, P., and Wang, H. (2010). "A wind tunnel simulation of the turbulence fields behind upright porous wind fences." *Journal of Arid Environments,* 74, 193-207.

Fujita, I. and Kunita, Y. (2011), "Application of aerial LSPIV to the 2002 flood of the Yodo River using a helicopter mounted high density video camera." Journal of Hydro-environment Research, 5, 323-331.

Gannett, H. (1906). "Manual of Topographic Methods, USGS Bulletinn No. 307, Series F, Geography, Government Printing office, Washington, DC.

García Nieto, P.J., del Coz Díaz, J.J., Castro-Fresno, D., and Ballester, Muñoz, F. (2010). "Numerical simulation of the performance of a snow fence with airfoil snow plates by FVM." *Journal of Computational and Applied Mathematics,* 234, 1200-1210.

Haniu, H., Sakamoto, H., and Takai, K. (2009). "Improvement of blower type snow fences by control of the shear layer." *Journal of Natural Disaster Science,* 17, 53-64.

Hauet, A., Muste, M., and Ho, H-C. (2008). "Digital mapping of waterway hydrodynamics, banks and floodplain using imagery." *CD-ROM Proceedings of ASCE World Environmental and Water Resources Congress 2008.*

Hauet, A., Muste, M., and Ho, H-C. (2009). "Digital mapping of riverine waterway hydrodynamic and geomorphic features." *Earth Surface Processes and Landforms,* 34, 242-252.

Heisler, G. M. and Dewalle, D. R. (1988). "Effects of windbreak structure on wind flow." *Agriculture, Ecosystems and Environment,* 22/23, 41-69.

http://www.mesonet.agron.iastate.edu/.

http://www.photogrammetry.com/.

Huang, L.M., Chan, H.C. and Lee, J.T. (2012), "A numerical study of flow around nonuniform porous fences." Journal of Applied Mathematics, Article 268371, doi:10.1155/2012/268371

Iowa DOT: Iowa's Cooperative Snow Fence Program (2005).
    http://www.iowadot.gov/maintenance/pdf/snowfencebooklet.pdf

Jiang, R., Jáuregui, D.V., White, and K.R. 2008. Close-range photogrammetry applications in bridge measurement: Literature review. *Measurement* 41, 823-834.

Kim, H.B. and Lee, S.J. (2002). "The structure of turbulent shear flow around a two-dimensional porous fence having a bottom gap." *Journal of Fluids and Structures,* 16 (3), 317-329.

Kirkil, G. and Constantinescu, G. (2009). "Nature of flow and turbulence structure around an in-stream vertical plate in a shallow channel and the implications for sediment erosion." *Water Resources Research*, Vol. 45, W06412, doi:10.1029/2008WR007363.

Kramer, T. and Joska, J (2008). "A quadtree mesh readaptation for the simulation of unsteady flow and transport," Proceedings of the *International Conference on Fluvial Hydraulics*, Izmir, Turkey, 2008, 783-790.

Kraus, K. (1992). *Photogrammetry, fundamentals and standard processes,* Vol. I, Fourth Revised and Enlarged Ed., Dümmler, Bonn.

Kunapo, J. (2005). "Spatial data integration for classification of 3D point clouds from digital photogrammetry." *Applied GIS,* Vol. 1, No. 3, pp. 26.1-26.15.

Lee, S.J. and Kim, H.B. (1999). "Laboratory measurements of velocity and turbulence field behind porous fences." *Journal of Wind Engineering and Industrial Aerodynamics,* 80, 311-326.

LPS Project Manager (2009). "User's guide, November 2009." ERDAS, Inc. 5051 Peachtree Corners Circle, Suite 100, Norcross, GA 30092, USA.

Luhman, T., Robson, S., Kyle, S., and Harley, I. (2011). "Close range photogrammetry: principles, techniques and applications." ISBN-13: 978-1849950572.

Marzolff, I. and Poesen, J. (2009). "The potential of 3D gully monitoring with GIS using high-resolution aerial photography and a digital photogrammetry system." *Geomorphology*, 111, 48-60.

Matthews, N.A. (2008). "Aerial and close-range photogrammetric technology: providing resource documentation, interpretation, and preservation." *Technical Note 428*. U.S. Department of the Interior, Bureau of Land Management, National Operations Center, Denver, Colorado. 42 pp.

Muste, M., Hauet, A., Ho, H-C., and Nakato, T. (2009). "Quantitative mapping of waterways characteristics at bridge sites." *IIHR Technical Report No. 470,* IIHR-Hydroscience and Engineering, The University of Iowa.

Muste, M., Ho, H-C., and Kim, D. (2011). "Considerations on direct stream flow measurements using video imagery: Outlook and research needs." *Journal of Hydro-environment Research,* 5, 289-300.

Moultrie Game Management System. www.moultriegamemanagement.com.

Nixon, W.A., Davison, M., and Kochumman, G. (2003). "Living snow fences, Iowa Highway Research Board Project TR 460 Final Report." *IIHR Technical Report 460,* IIHR-Hydroscience and Engineering, College of Engineering, The University of Iowa.

Perera, M.D. (1981). "Shelter behind two-dimensional solid and porous fences." *Journal of Wind Engineering and Industrial Aerodynamics,* 8, 93-104.

Photomodeler. http://www.photomodeler.com/products/how-it-works.html.

Raine, J.K. and Stevenson, D.C. (1977). "Wind protection by model fences in a simulated atmospheric boundary layer." *Journal of Industrial Aerodynamics,* 2, 159-180.

Saif, A.M., Mohamed, A.M.I., and Alam Eldein, A.M. (2010). "Variable porosity wind fences to control aeolian sand transport." CD-ROM *Proceedings of Tenth International Congress of Fluid Dynamics*.

Sañudo-Fontaned, L.A., Castro-Fresno, D., del Coz-Díaz, J.J., and Rodriguez-Hernandez, J. (2011). "Classification and comparison of snow fences for the protection of transport infrastructures." *Journal of Cold Regions Engineering*, 25, 162-181.

Schenk, T. (2005). "Introduction to photogrammetry." *GS 400.02, Autumn Quarter 2005*. Department of Civil and Environmental Engineering and Geodetic Science. The Ohio State University, 2070 Neil Ave., Columbus, OH 43210, USA.

Seginer, I. (1972). "Windbreak drag calculated from the horizontal velocity field." *Boundary-Layer Meteorology*, 3, 87-97.

Sinha, S., Liu, X. and Garcia, M. (2012). "Three-dimensional hydrodynamic modeling of the Chicago River," *Environmental Fluid Mechanics*, 12(5), 471-494.

Soole, P. and Poropat, G. (2000). "Highwall mapping using terrestrial photogrammetry." *Bowen Basin Symposium 2000 Proceedings, Rockhampton, 22-24 October, (2000)*, Ed. J.W. Beeston, pp. 343-346.

Sturzenegger, M. and Stead, D. (2009). "Close-range terrestrial digital photogrammetry and terrestrial laser scanning for discontinuity characterization on rock cuts." *Engineering Geology*, 106,163-182.

Tabler, R.D. (1991). "Snow fence guide." *Strategic Highway Research Program,* Washington, D.C.

Tabler, R.D. (2003). "Controlling drifting and blowing snow with snow fences and road design." *Final Report, NCHRP Project 20-7 (147),* Transportation Research Board of the National Academies, Washington, D.C.

Tecplot 360 (2011). "User's manual, 2011." Tecplot, Inc. PO Box 52708, Bellevue, WA 98015, USA.

Topcon GTS 235 Total Station. http://geog.sfsu.edu/geog/field-equipment/topcon-gts-235-total-station.

Tsubaki, R. and Fujita, I. (2010). "Unstructured grid generation using LiDAR data for urban flood inundation modelling," *Hydrological processes*, 24(11), 1404-1420.

Wolf, P.R. and Dewitt, B.A. (2000). *Elements of photogrammetry with GIS applications,* The Mc Graw-Hill Companies, 3rd Edition, USA.

Yakar, M. (2009). "Using close range photogrammetry to measure the position of inaccessible geological features." *Experimental Techniques,* doi: 10.1111/j.1747-1567.2009.00583.

Yakar, M. and Yilmaz, H.M.   (2008). "Using in volume computing of digital close range photogrammetry." *The International Archives of the Photogrammetry, Remote Sensing and Spatial Information Sciences. Vol. XXXVII. Part B3b. Beijing 2008.*

Yakar, M., Yilmaz, H.M., and Mutluoglu, O. (2010). "Close range photogrammetry and robotic total station in volume calculation." *International Journal of the Physical Sciences,* 5(2), 86-96.